3-25-2016

The GlueX Start Counter & Beam Asymmetry Σ in Single π^{0} Photoproduction

Eric J. Pooser
Florida International University, epoos001@fiu.edu

DOI: 10.25148/etd.FIDC000274

FLORIDA INTERNATIONAL UNIVERSITY

Miami, Florida

THE GLUEX START COUNTER & BEAM ASYMMETRY Σ IN SINGLE π^0 PHOTOPRODUCTION

A dissertation submitted in partial fulfillment of the

requirements for the degree of

DOCTOR OF PHILOSOPHY

in

PHYSICS

by

Eric Pooser

2016

To: Dean Michael R. Heithaus
College of Arts, Sciences and Education

This dissertation, written by Eric Pooser, and entitled The GlueX Start Counter & Beam Asymmetry Σ in Single π^0 Photoproduction, having been approved in respect to style and intellectual content, is referred to you for judgment.

We have read this dissertation and recommend that it be approved.

Lei Guo

Misak Sargsian

Cem Karayalcin

Werner Boeglin, Major Professor

Date of Defense: March 25, 2016

The dissertation of Eric Pooser is approved.

Dean Michael R. Heithaus
College of Arts, Sciences and Education

Andrés G. Gil
Vice President for Research and Economic Development
and Dean of the University Graduate School

Florida International University, 2016

DEDICATION

First and foremost, I would like to dedicate this dissertation to both of my parents Scott and Mona. Without their unconditional love and support through the years, I would have never had the opportunity to complete, or let alone conduct, my dissertation work. They both have stood steadfastly by my side through countless trials and tribulations and without their unwavering guidance my dissertation would have never been possible.

Secondly, I would like to dedicate my dissertation to the love of my life Jennifer. Her unwavering love and support over the last five years fueled me towards the successful completion of my dissertation. Without her absolute love and devotion to aiding me in all aspects of life, I never would of had the ability to finish the marathon that is completing ones dissertation work.

ACKNOWLEDGMENTS

I would first like to acknowledge Professor Werner Boeglin for his unparalleled work as my dissertation advisor. Werner was the primary contributor to my dissertation work. He provided countless hours of guidance and invaluable instruction that has surmounted to the successful completion of my dissertation. Moreover, I would like to acknowledge him for the numerous number of fruitful discussions that led to my deeper understanding of my dissertation work and various other topics in physics. I honestly can not thank him enough for taking the time, and putting forth the effort to ensure that I could become a well rounded physicist.

I would also like to acknowledge the following Jefferson Lab staff scientists for their aid in my dissertation work: Mark Ito, Simon Taylor, Paul Mattione, Beni Zihlmann, and Justin Stevens. These gentlemen provided copious amounts of guidance and invaluable instruction which ultimately led to the successful calibration of the Start Counter detector in Hall D and the analysis of various physics observables utilizing the GlueX spectrometer.

Furthermore, I would like to acknowledge the following people for being jovial office mates and their aid in a multitude of topics such as collaboration on course work, qualifier preparation, understanding physics, learning of various computer languages, and general advice/coping mechanisms of how to deal with being a graduate student in physics: Jason Bono, Adam Freese, Sarah Dhalla, Rafael Badui, Puneet Khetarpal, Hari Khanal, and Dipak Rimal. In addition, I would like to acknowledge a few fellow Hall D graduate students for their pragmatic discussions and suggestions when learning the Hall D/GlueX framework: Mike Staib, Alex Barnes, and Will McGinley.

ABSTRACT OF THE DISSERTATION

THE GLUEX START COUNTER & BEAM ASYMMETRY Σ IN SINGLE π^0 PHOTOPRODUCTION

by

Eric Pooser

Florida International University, 2016

Miami, Florida

Professor Werner Boeglin, Major Professor

The GlueX experiment aims to study meson photoproduction while utilizing the coherent bremsstrahlung technique to produce a 9 GeV linearly polarized photon beam incident on a liquid H_2 target. A Start Counter detector was fabricated to properly identify the accelerator electron beam buckets and to provide accurate timing information. The Start Counter detector was designed to operate at photon intensities of up to $10^8\gamma$/s in the coherent peak and provides a timing resolution ~ 300 ps so as to provide successful identification of the electron beam buckets to within 99% accuracy. Furthermore, the Start Counter detector provides excellent solid angle coverage, $\sim 90\%$ of 4π hermeticity, and a high degree of segmentation for background rejection. It consists of a cylindrical array of 30 scintillators with pointed ends that bend towards the beam at the downstream end. Magnetic field insensitive silicon photomultiplier detectors were selected as the readout system.

An initial measurement of the beam asymmetry Σ in the exclusive reaction $\vec{\gamma}p \to \pi^0 p$, where $\pi^0 \to \gamma\gamma$ has been carried out utilizing the GlueX spectrometer during the Spring 2015 commissioning run. The tagged photon energies ranged from $2.5 \leq E_\gamma \leq 3.0$ GeV in the coherent peak. These measurements were then compared to the world data set and show remarkable agreement with only two hours of physics production running.

TABLE OF CONTENTS

CHAPTER PAGE

LIST OF TABLES

LIST OF FIGURES

CHAPTER 1

GlueX Overview

1.1 The GlueX Experiment in Hall-D

The GlueX experiment is designed to explore the spectrum of light mesons and search for exotic hybrid mesons and baryons that are predicted by quantum chromodynamics (QCD). Through the production of exotic mesons, which gives evidence for the formation of QCD flux tubes, the GlueX collaboration will be able to further investigate a fundamental challenge in physics: that is, a quantitative understanding of confinement of quarks and gluons in QCD [1]. Exotic hybrid mesons directly manifest the degrees of freedom associated with quark confinement [2], thus providing a suitable laboratory in which to conduct studies regarding the excitation of flux tube strings binding conventional $q\bar{q}$ mesons ($q = u$, s, or d).

Using a 12 GeV electron beam, a 9 GeV linearly polarized photon beam will be produced and sent to the GlueX experiment. The tagged photon beam is expected to be ideal for producing the exotic hybrid meson spectrum. The polarized photon beam produced *via* the coherent bremsstrahlung technique is incident on a super cooled liquid hydrogen target located at the center of the GlueX spectrometer. The GlueX detector (Fig. 1.1), is a solenoid-based 4π hermetic detector. It has been designed to fit the requirements for conducting Partial Wave Analysis (PWA), which extracts information about the line shape of a resonance, the production mechanism, and the associated decay modes [2]. The GlueX collaboration has an approved experiment to collect a total of 200 days of physics data utilizing 9 GeV tagged photons in the coherent peak, at an average intensity of 5×10^7 photons on target per second. This data sample will exceed the current photoproduction data by several orders of magnitude [4].

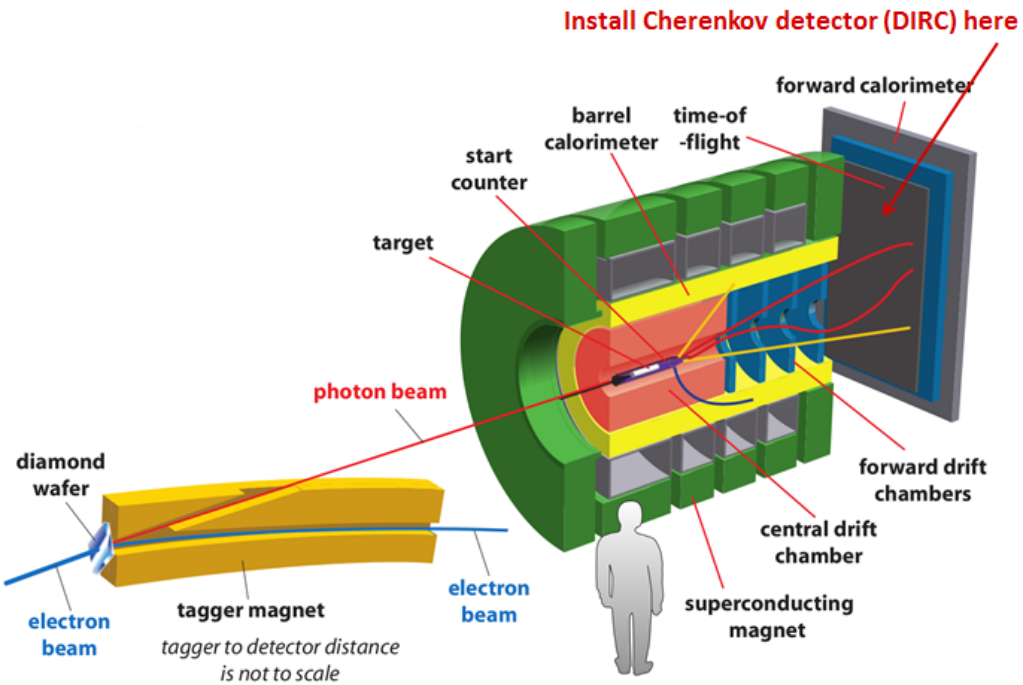

Figure 1.1: GlueX detector overview [3].

1.1.1 Theoretical Framework

Recent lattice QCD predictions indicate a bountiful spectrum of hybrid mesons that have both exotic and non-exotic J^{PC} and can be seen in Fig. 1.2. Here, J is the total angular momentum, P is Parity, and C is Charge parity [4]. Here $\vec{J} = \vec{L} + \vec{S}$, $P = (-1)^{L+1}$, and $C = (-1)^{L+S}$ where $\vec{L}$ and $\vec{S}$ are the usual orbital angular momentum and spin of the $q\bar{q}$ system respectively. Permissible values of J^{PC} arise from the usual quantum numbers of a composite fermion-antifermion system. A few combinations of L and S that are not permitted are $0^{--}, 0^{+-}, 1^{-+}, 2^{+-}, \ldots$ and are referred to as the *exotic* quantum numbers. The range of masses of established conventional meson nonets and the associated light exotic hybrid counterparts range from the π mass up to 2.5 GeV/c^2 [2], whose production are attainable within the dynamic energy ranges of GlueX.

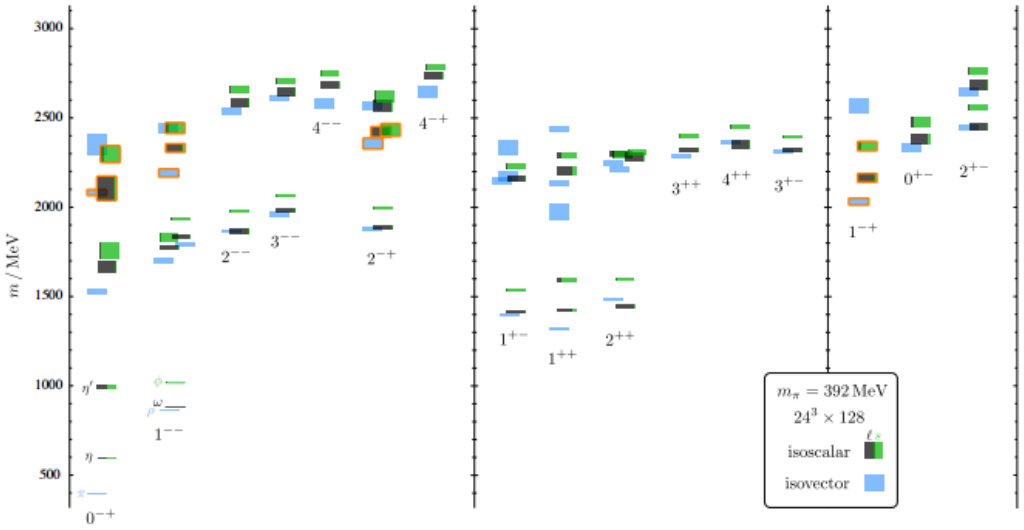

Figure 1.2: Lattice QCD calculations [5]. The left column are mesons with negative parity, while the middle column have positive parity. The column on the right are the exotic meson predictions with the lightest 1^{-+} state being the $\pi_1(1600)$. The boxes with an orange outline are the predicted lightest hybrid meson supermultiplets.

With high enough beam energy, the string-like flux tube binding the $q\bar{q}$ system is able to become excited. The vibrational quantum numbers of the string, when combined with those of $q\bar{q}$, can produce mesons with exotic J^{PC}. They are dubbed *hybrids* because the mesons manifest both their quark and gluonic content. Since gluons carry color charge it is also possible to form bound states of glue with no quarks present. Such mesons are called *glueballs* [2]. Since the expected quantum numbers of glueballs with masses below 4 GeV are not exotic, their detection is complicated by the fact they can mix with other $q\bar{q}$ states. Lattice QCD and flux tube models show strong evidence suggesting the existence of the lightest exotic mesons and glueballs to be in the mass range of $1.5 - 2.5\,\mathrm{GeV/c^2}$. The GlueX detector is designed to observe exotic quantum number and hybrid sates due to its 4π hermeticity resulting in the reconstruction of final-state particles and the subsequent application of a sophisticated partial wave analysis (PWA) [2].

While some hints of exotic mesons have been observed *e.g.*, the E852 experiment, there are either a number of inconsistencies in understanding the production mechanisms or the data suffer from limited statistics [1]. The linear polarization of the photon beam in GlueX aids in the determination of the J^{PC} quantum numbers and is essential in determining the production mechanism for various observed and predicted $q\bar{q}$ states. Within the first year of running, GlueX is expected to collect data that will exceed the current photoproduction world data set by at least one order of magnitude [2].

1.2 GlueX Beamline

The Continuous Electron Beam Accelerator Facility (CEBAF), as seen in Fig. 1.3, produces a 12 GeV electron beam ($0.05 - 2.2\mu A$) that is steered to the HallD tagger hall, upstream of the GlueX spectrometer. An overview of the GlueX beam line

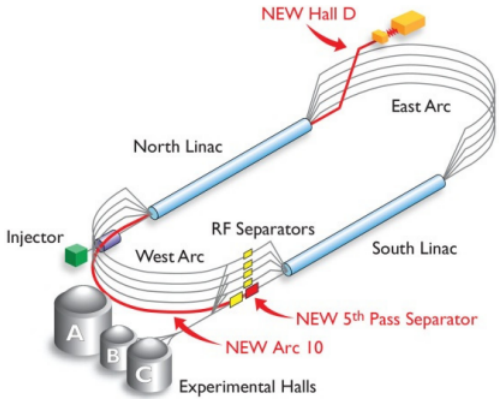

Figure 1.3: CEBAF Schematic. Labels indicate the 12 GeV upgrades.

is illustrated in Fig. 1.4. A secondary photon beam is produced *via* the coherent bremsstrahlung technique in which the incident electron beam strikes a thin 20 μm diamond wafer. The photon rate and energy spectrum is shown in Fig. 1.5. The tagged photon beam ranges in energy from $E_\gamma \in [3.0, 11.8]$ GeV. The coherent

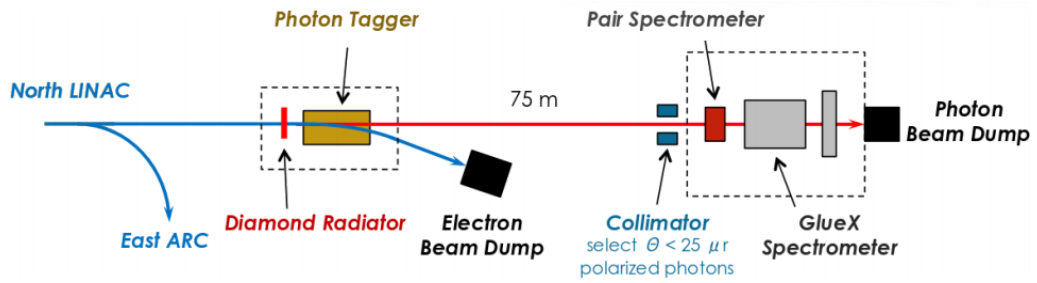

Figure 1.4: Overview of the GlueX beamline. CEBAF provides a 12 GeV electron (blue) that is converted into linearly polarized photons (red) by the diamond radiator. The photons travel 75 meters downstream and are collimated prior to entering HallD [6].

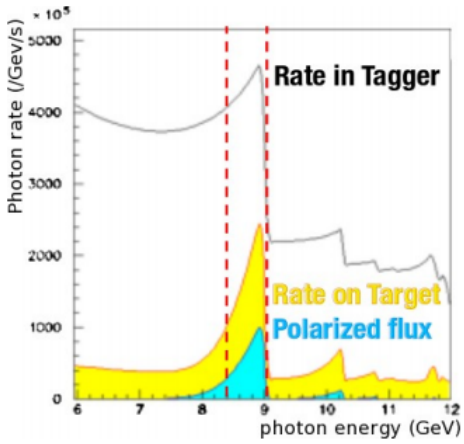

Figure 1.5: Simulated GlueX photon rates and energy spectrum [6].

peak ranges from $E_\gamma \in [8.4, 9.0]$ GeV and contains photons with an average linear polarization of $\approx 40\%$. A 2.2μA electron beam results in an on target, polarized photon rate of 100 MHz.

1.2.1 GlueX Tagger Spectrometers

The scattered electrons from the aforementioned bremsstrahlung process enter into the tagger magnet and spectrometer which is an Elbek-type spectrometer [7]. The tagger magnet bends, *via* the Lorentz Force, the electron beam away from the photon beam, towards the tagger spectrometer. The magnetic field of the tagger

magnet is constant, thus the Lorentz force acting on the scattering electrons will result in them having a particular radii of curvature that is directly proportional their respective momentum (energy). Therefore by placing the tagger spectrometer in the focal plane of the scattering electrons, it is possible to reconstruct the energy of the electrons in the focal plane. By precisely knowing the energy of the electrons *i.e.*, $E + \delta E$, conservation of energy provides a precise measurement of the photon beam energy. The aforementioned procedure is known as "tagging." The tagger microscope measures finely the coherent peak, while the tagger hodoscope measures coarsely the remaining large range of photon energies.

The tagger microscope (TAGM), seen in Fig. 1.6 consists of 102 columns of 5 BCF-20 scintillating fibers which are 20 ± 2m long and 2×2 mm^2 wide. The

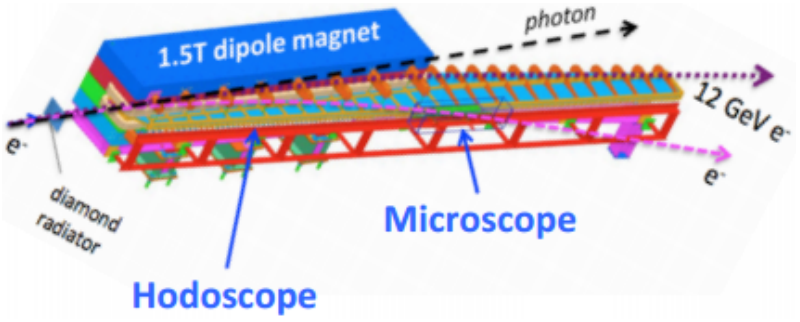

Figure 1.6: GlueX tagger spectrometers. The combined $e^-\gamma$ beam enter the tagger magnet and the deflected e^- beam is measured by the tagger hodoscope and microscope. The electrons that are not measured are collected in the electron beam dump [3].

scintillators are coupled to 1 meter long BCF-98 light guides which are also 2×2 mm^2 wide and are read out *via* 110 Hamamatsu S10931-050P silicon photomultipliers (SiPMs) also known as multi-pixel photon counters (MPPCs) (50 μm pixel size). The microscope measures the tagged photon beam in the coherent peak with 5 MeV resolution in an energy range of $8.1 - 9.1$ GeV [8]. The microscope was constructed atop a platform such that it may be moved in order to achieve the best alignment

possible with the focal plane of the scattered electrons pertaining to the coherent peak.

The tagger hodoscope (TAGH) consists of 218 counters made of EJ-228 scintillator material coupled to a cylindrical UVT PMMA light guide readout by Hamamatsu R9800 PMTs. The hodoscope counter continuously samples the photon energy range $E_\gamma \in [9.1, 11.78]$ GeV and 30 - 50 % sampling rate for $E_\gamma \in [3.048, 8.1]$ GeV [8]. The reduction in sampling rate is an effective pre-scaling which reduces the amount of data that is recorded by the ADCs and TDCs per triggered event. This is done so that overload in the buffers is minimized as a result of the high event rate in the lower electron energy range.

During the Spring 2015 commissioning run, the beam energy was significantly reduced due to technical issues with the accelerator. For this reason the pair spectrometer's (PS) magnetic field was reduced slightly to accommodate the lower beam energy. Therefore an ad-hoc energy spectrum correction was performed between the PS and the tagger spectrometers so that the tagging efficiency could be calculated. The tagging efficiency is a measure of how often an electron of a particular energy produces a hit in the tagger spectrometer while the corresponding photon of identical energy produces a hit in the pair spectrometer for each triggered event. The results of the tagging efficiencies are shown in Fig. 1.7. The reduction in tagging efficiency in the TAGH, below the TAGM energy range, is attributed to the 50% sampling rate relative to the energy region above the TAGM which has a 100% sampling rate resulting in tagging efficiencies above 90%. The nominal design of the TAGM was to have 77% tagging efficiency and the Spring 2015 data measured a 70-75% tagging efficiency in the focal plane [9]. Upon comparing the photon beam energy spectrum between an amorphous and diamond radiator run (as seen in Fig. 1.8) it is clear that with a oriented diamond radiator it is possible to obtain a high

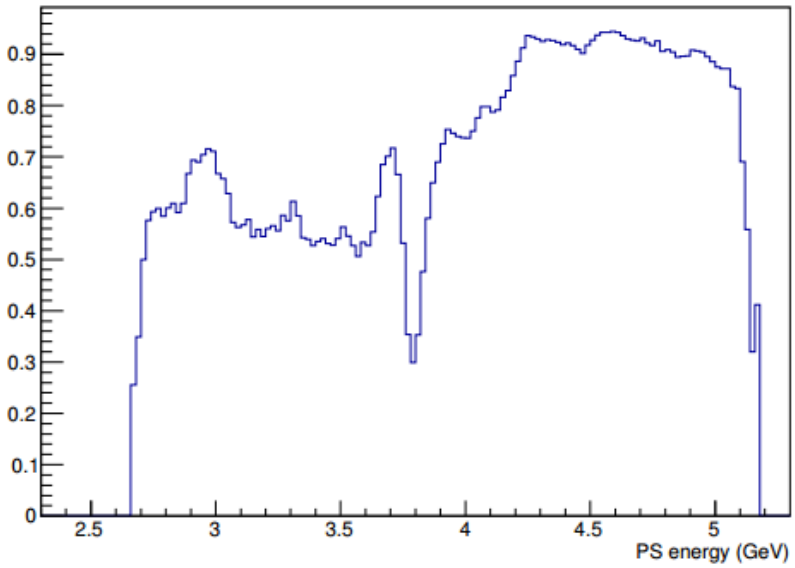

Figure 1.7: Tagging efficiency in the Spring 2015 commissioning run. The dip in tagging efficiency at 3.8 GeV results from a physical gap between the TAGM and TAGH [9].

degree of polarization. A fit to the coherent peaks yielded a maximum linear photon polarization of 65% [3].

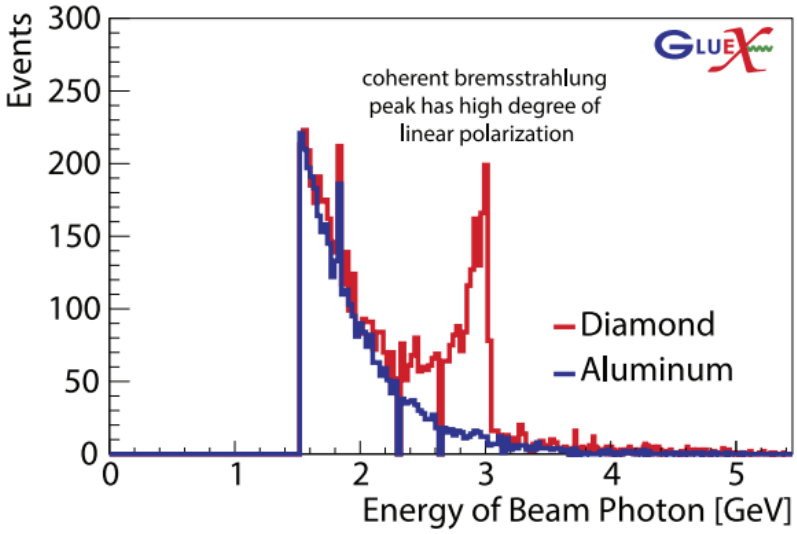

Figure 1.8: Polarized photon beam energy spectrum. The blue histogram is the amorphous radiator photon energy spectrum in which the bremsstrahlung spectrum is clearly visible. The red histogram is the oriented diamond photon energy spectrum in which the coherent edge is clearly visible.

1.2.2 Photon Beam Flux & Polarization Monitoring

The photon beam is collimated by a 3.4-mm-diameter collimator. Downstream of the collimator and upstream of the GlueX spectrometer is the pair spectrometer (PS) that is composed of thin foil converters which create e^+/e^- pairs *via* pair production, a magnet to separate their trajectories, and a hodoscope to track the charged particle trajectories. The configuration of the PS is seen in Fig. [10]. Since

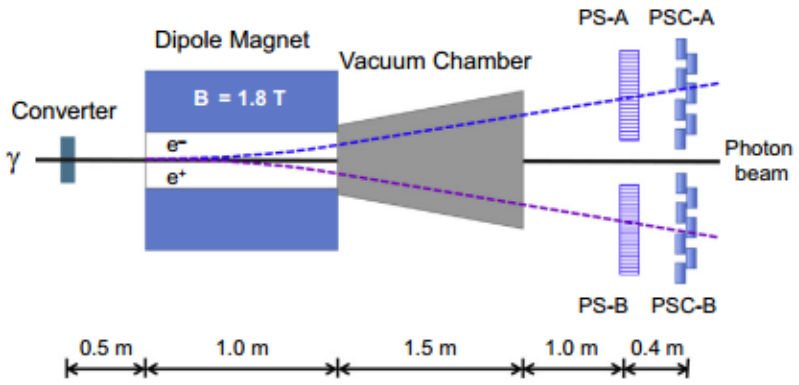

Figure 1.9: Pair spectrometer configuration. PS and PSC correspond to the hodoscope and coarse scintillator counters respectively [10].

pair production is a well known Quantum Electro-Dynamic (QED) process, the pair spectrometer allows for monitoring of the photon beam's flux, polarization, and energy [7].

The nominal design of the PS counters is to detect beam photons in the range $E_\gamma \in [6, 12.5]$ GeV with a resolution of ≈ 30 MeV. The converter thickness has yet to be determined however, they will most likely range from $10^{-4} - 10^{-2}$ radiation lengths [8].

During the Spring 2015 commissioning run, the pair spectrometer was found to have a detection efficiency larger than 95% with random coincidental background contribution to be less than 1.5% [9]. Figure 1.10, illustrates the energy resolution and photon energy spectrum of the PS during the Spring 2015 commissioning run [9].

Furthermore the time resolution of all PS counters was found to be < 150 ps relative

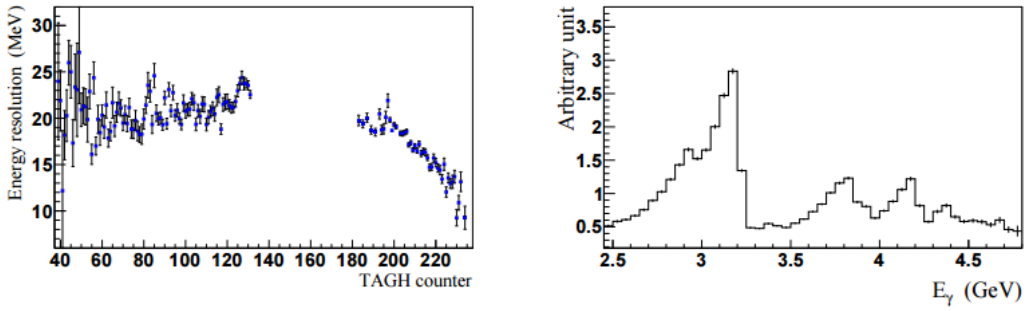

Figure 1.10: Pair spectrometer performance.The data is from the Spring 2015 commissioning run. Left: energy resolutions of the PS hodoscope. Right: photon energy spectrum with a diamond radiator run.

to the design resolution of 250 ps.

In order to measure the degree of linear polarization contained in the collimated photon beam a triplet polarimeter (TPOL) was constructed down stream of the collimator and upstream of the PS as illustrated in Fig. 1.11. Triplet photoproduc-

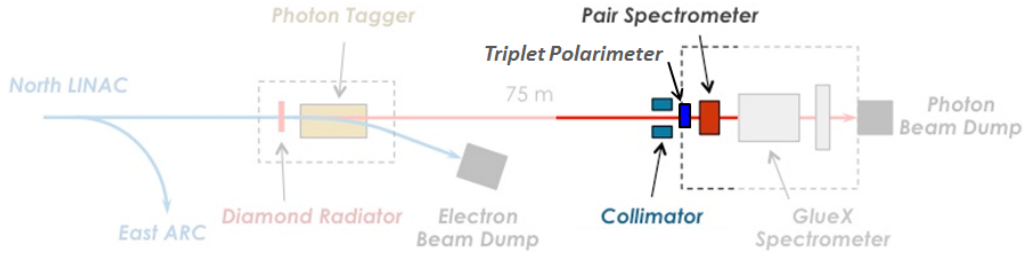

Figure 1.11: Collimator cave configuration [3].

tion, $\vec{\gamma}e^- \rightarrow e^-e^+e^-$, occurs when a beam photon interacts with an atomic electron's electric field, provided by a thin beryllium foil, and results in the production of e^-e^+ pair, detected in the PS, and a recoil e^-. The e^-e^+ pair is forward going, and the transverse momentum is carried away by the slow moving recoil e^- at potentially large polar angles [11]. The resulting angular distribution of the recoil e^- provides information regarding the degree of beam polarization.

The TPOL was constructed as a double sided silicon strip detector with a thickness of 1.034 mm. The detector consists of 32 azimuthal sectors on the ohmic side (seen in Fig. 1.12) and 24 concentric rings on the junction side, providing 768 distinct angular regions that measures the azimuthal distribution of the recoil electron with a high degree of precision [11].

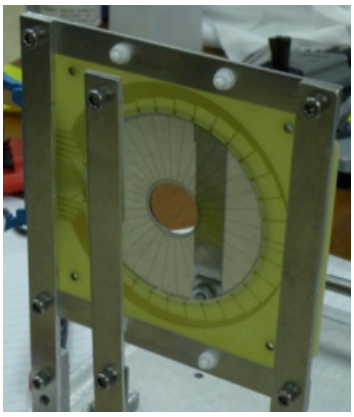

Figure 1.12: Sector side of triplet polarimeter [12]. It has an outer active diameter of 70 mm and an inner active diameter of 22 mm [11].

During the Spring 2015, one run was taken with an amorphous radiator (3180, $\approx$ 4 hrs and another with an oriented diamond radiator (3185, $\approx$ 2 hrs). The resulting data were then analyzed to measure the degree of polarization in the beam with both the amorphous and diamond radiator and is shown in Fig. 1.13. The polarization

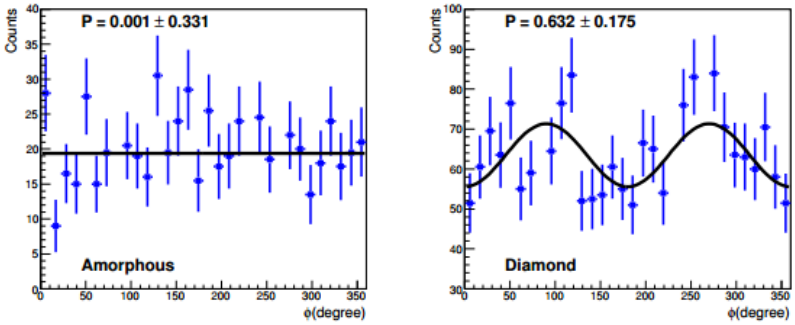

Figure 1.13: TPOL Measure of beam polarization. Left: amorphous run illustrating zero beam polarization as expected. Right: oriented diamond run producing a beam polarization of 0.632 ± 0.175.

(P) was extracted from the data by fitting the azimuthal distribution of the recoiling e^- to the functional form $A[1 + Bcos(2\phi)]$ with $B = P\Sigma$ where Σ is the assumed beam asymmetry. The results indicate that with an oriented diamond the beam had a polarization of $63.2 \pm 17.5\%$, which was consistent with other various physics analyses and a direct fit to the coherent peak to extract the polarization. The large statistical errors seen in Fig. 1.13 are the result of severely low statistics obtained in the run which only lasted a few hours [9].

1.3 GlueX Spectrometer

A schematic top view of the GlueX detector is show in Fig. 1.14. The beamline and

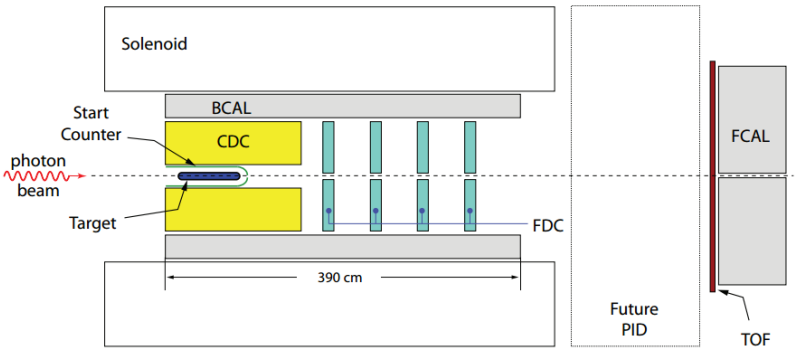

Figure 1.14: GlueX spectrometer schematic (top view) [13].

associated detector components were discussed in detail in section 1.2. Surrounding the GlueX target is the start counter (ST), the central drift chamber (CDC), and the barrel calorimeter (BCAL). Downstream of the target and CDC is the forward drift chamber (FDC). All of these detector systems are enveloped by a superconducting solenoid magnet. Downstream of the solenoid is the time of flight (TOF) and forward calorimeter (FCAL) detectors. The incident linearly polarized photon beam interacts with a liquid hydrogen target, which is 30 cm in length, and has an upstream inner diameter of 2.42 cm, tapering down to a 1.56 cm inner diameter [8].

The resulting charged particles and photons produced in the γp collisions are then detected by the GlueX detector. Measuring the charged particle trajectories in the solenoidal magnetic field allows one to extract their charge and their momentum. The GlueX solenoid consists of four coils that each run at a nominal current of 1350 A, producing a magnetic field of 2.08 T at nominal design. It is 4.795 m long, has an inner diameter of 2.946 m, and an outer diameter of 3.759 m [8].

1.3.1 Drift Chambers

Surrounding both the ST and the LH_2 target is the CDC. The CDC is a large straw tube cylindrical drift chamber that consists of 3522, 1.5 m long straw tubes each with an inner diameter of 15.55 mm. A side view of the CDC is seen in Fig. 1.15. Each

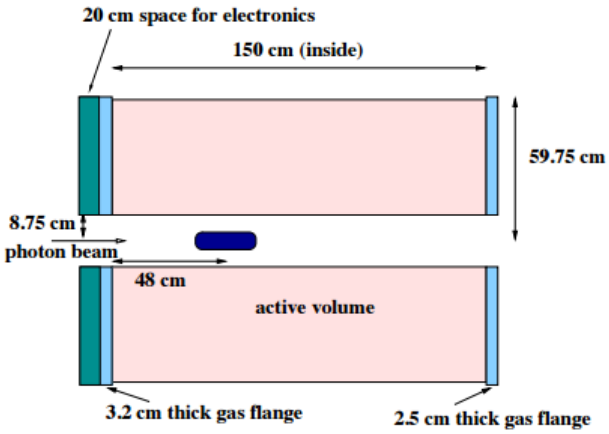

Figure 1.15: CDC schematic (side view). The CDC's active region covers charged tracks with polar angles $\theta \in [6°, 168°]$ while being optimized for polar angles $\theta \in [29°, 132°]$. The blue cylinder is the target [8]. The ST is not shown however it would occupy the space between the CDC and the target.

straw tube contains an anode wire of 20 μm diameter gold-plated tungsten. The inner wall of the tube forms the cathode which ensures uniformity of the electric field around the wire. The CDC has 28 layers of straw tubes arranged in both axial and stereo ($\pm 6°$) configurations (seen in Fig. 1.16) located within a cylindrical volume of

inner diameter of 20 cm and outer diameter 1.12 m and is filled with a 50% Argon, 50% CO_2 gas mixture. The CDC provides both r and ϕ position measurements for

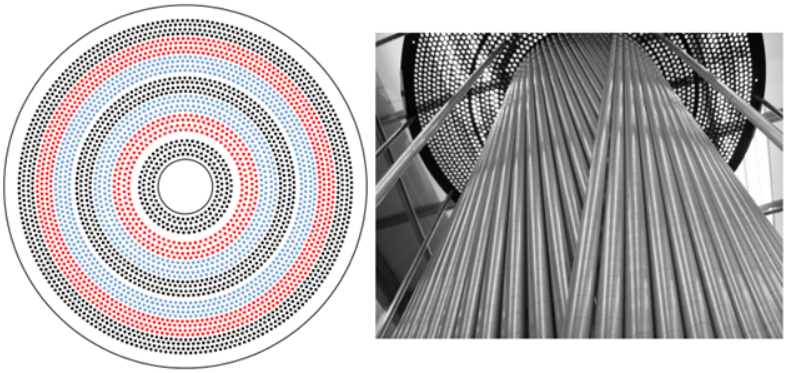

Figure 1.16: CDC design. Left: schematic of the CDC straw tube configuration at the upstream end plate. The axial straws are in black, the $+6°$ stereo layers are red, while the $-6°$ stereo layers are blue. Right: straw tubes in stereo layers 8 and 9 [8].

charged tracks with an expected position resolution of 150 μm along with timing and dE/dx measurements from the F125ADC's FPGA [8]. A picture of the fully assembled CDC is seen in Fig. 1.17.

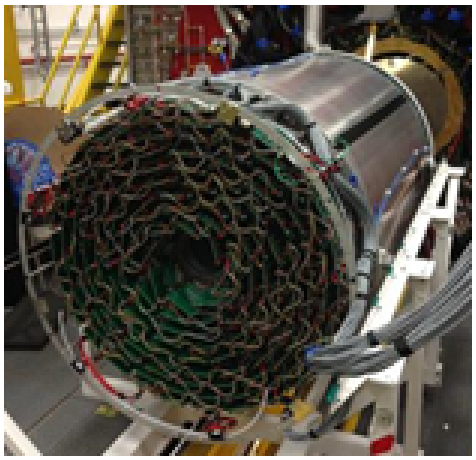

Figure 1.17: Fully assembled CDC in Hall D.

Forward-going charged particles are tracked by the FDC, which is downstream of the CDC and ST and is seen in Fig. 1.18. The FDC system consists of 24 planar drift chambers (cells) with cathode strip and wire readouts that are grouped into

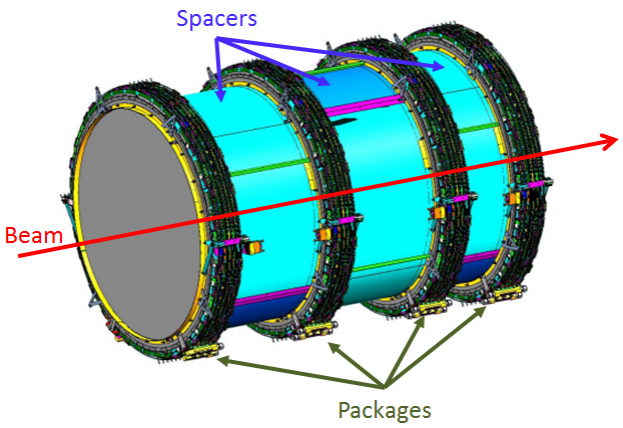

Figure 1.18: FDC schematic. The spacers separate the 4 FDC packages each consisting of 6 planar drift chambers (cells).

four identical packages of six cells [14]. Each cell contains 1 layer of 216 U cathode strips which are 5 mm in front (upstream) of 1 layer of 96 sense wires and 97 field wires. 5 mm behind (downstream) the wires is 1 layer of 216 V cathode strips. The U and V cathode strips are oriented $+75°$ and $-75°$ relative to the wires (seen in Fig. 1.19). Six cathode-wire-cathode assemblies, also known as cells, comprise one package with each cell being rotated 60° relative to the one preceding it. The 2328 field wires are 80 μm thick, gold plated copper-beryllium wires, while the 2304 sense wires, 5 mm apart from the field wires, are 20 μm thick, gold plated tungsten wires. Each of the six cells comprising one package is filled with a 40% argon 60% CO_2 gas mixture [8].

The arrangement described above allows the FDC to provide tracking, and dE/dx information, of forward-going charged particles with polar angles $\theta \in [1°, 20°]$ with a resolution on the order of 250 μm. The cathode cells provide a three-dimensional space point from each active cell layer whose schematic is seen in Fig. 1.19. In addition the timing information from the wires is readout by F1TDCs while the cathode strips timing is readout by the F125ADC FPGA which enables the reconstruction of both the coordinate of the hit along the wire and a coordinate

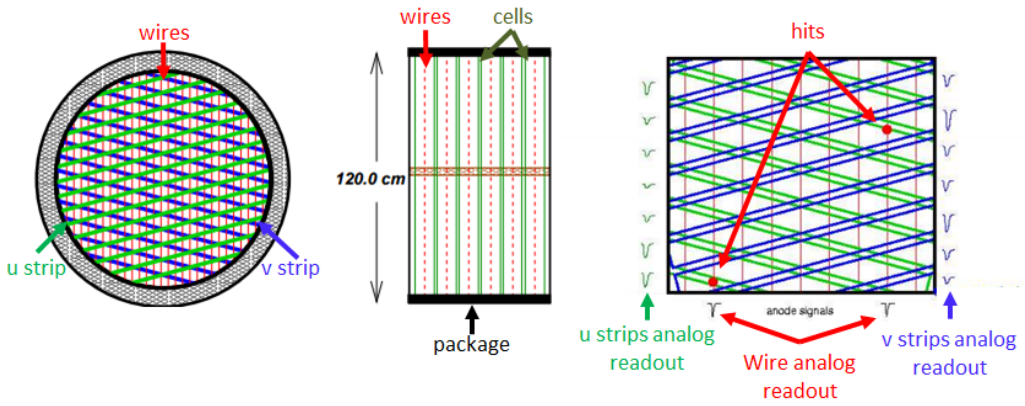

Figure 1.19: FDC cathode chamber schematics. Left: front view of the cathode cell. Facing downstream the wires are vertical while the U strips are in front of the wires and the V strips are behind the wires. Middle: side view of a package. Right: illustrates an event with two nearby hits and how they are resolved from the cathode and wire readouts [14].

transverse to the wire *i.e.*, drift time. Thus, the reconstruction of space points is achievable and facilitates the association of adjacent hits with each other, thereby enhancing pattern recognition [8]. The fully assembled FDC is shown in Fig. 1.20.

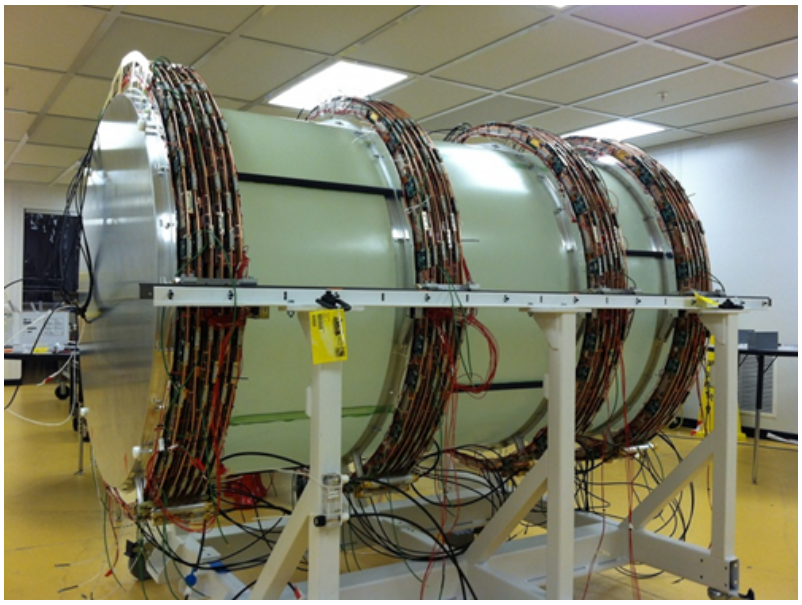

Figure 1.20: Fully assembled FDC.

During the Spring 2015 commissioning run the CDC and FDC efficiencies were calculated along with wire resolutions and are summarized in Fig. 1.21. It is clear

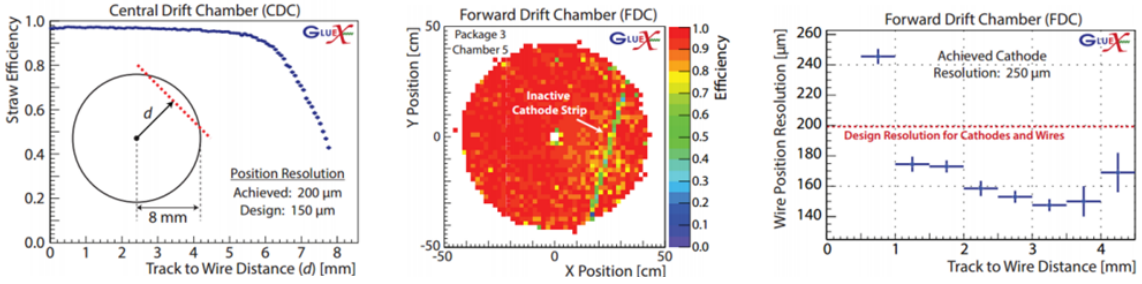

Figure 1.21: Drift chamber performance in Spring 2015 commissioning run. Left: CDC straw efficiencies as a function of the track to wire distance. The efficiency decreases close to the straw walls due to the shorter track length in the active volume of the cell [9]. The achieved position resolution is close to the design resolution. Middle: FDC tracking efficiencies in package 3, chamber 5. Right: wire resolution as a function of the track to wire distance. The achieved position resolution is close to the design resolution.

that the drift chambers are close to design resolution and efficiencies are acceptable. Moreover, quality track reconstruction was observed in the Spring 2015 commissioning run and is seen in Fig. 1.22.

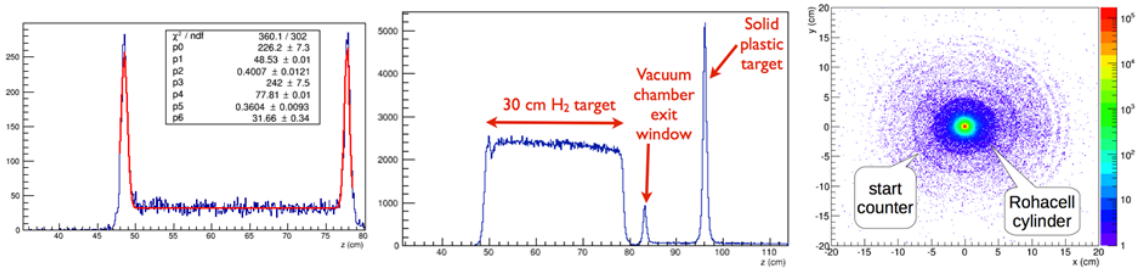

Figure 1.22: Track reconstruction in the Spring 2015 commissioning run. Left: z-coordinate of track vertices in an empty target run. A tracking spatial resolution of $\approx$ 4 mm was achieved. Middle: full target run where the target is clearly reconstructed along with other prominent features. Right: xy-coordinate of track vertices where the ST and target geometries are visible.

1.3.2 Calorimeters

By detecting photons, the primary goal of the calorimeters are to reconstruct π^0's and η's that are produced in the decays of heavier states [4]. Residing immediately inside the solenoid is the electromagnetic barrel calorimeter (BCAL) modelled closely after the EmCal utilized in the KLOE experiment at DAΦNE [8]. The BCAL envelopes all of the solenoid based detectors *i.e.*; the CDC, FDC, ST, as well as the LH_2 target. The BCAL, seen in Fig. 1.23, consists of 48 modules (each spanning 7.5° in ϕ) that are 3.90 m in length. It is cylindrical in design with an outer diameter

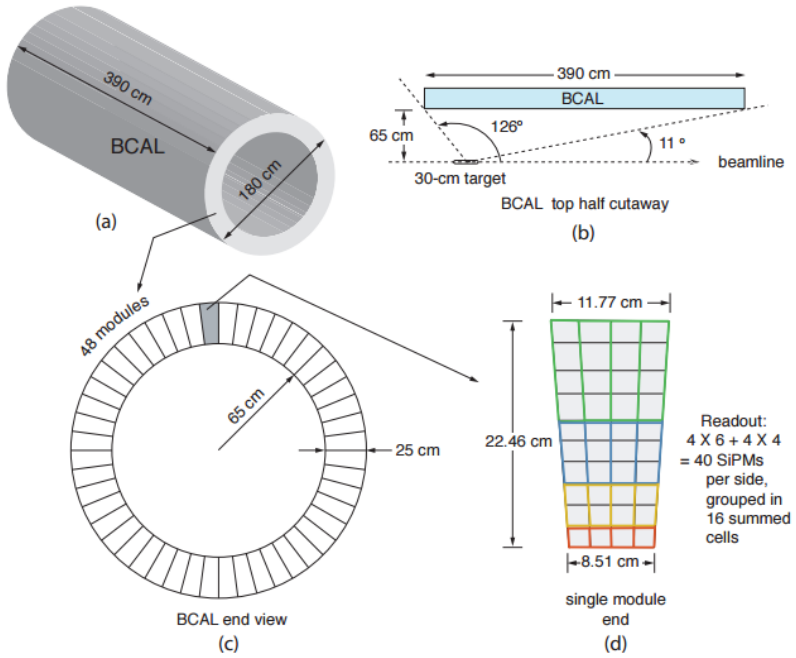

Figure 1.23: BCAL schematic. (a) isometric view of BCAL geometry, (b) side view of BCAL with polar angle acceptances, (c) end view of BCAL geometry, (d) readout module and light guide geometry [8].

of 1.8 m and inner diameter of 1.3 m. The geometry of the BCAL, relative to the target allows for a large acceptance of polar angles *e.g.*, $\phi \in [11°, 126°]$.

Each of the 48 modules in the BCAL is comprised of a lead and scintillating fiber (SciFi) matrix in which the fibers are embedded directly into lead sheets as

illustrated in Fig. 1.24. There are 683000, 1 mm^2 Kuraray SCSF-78MJ multi-clad

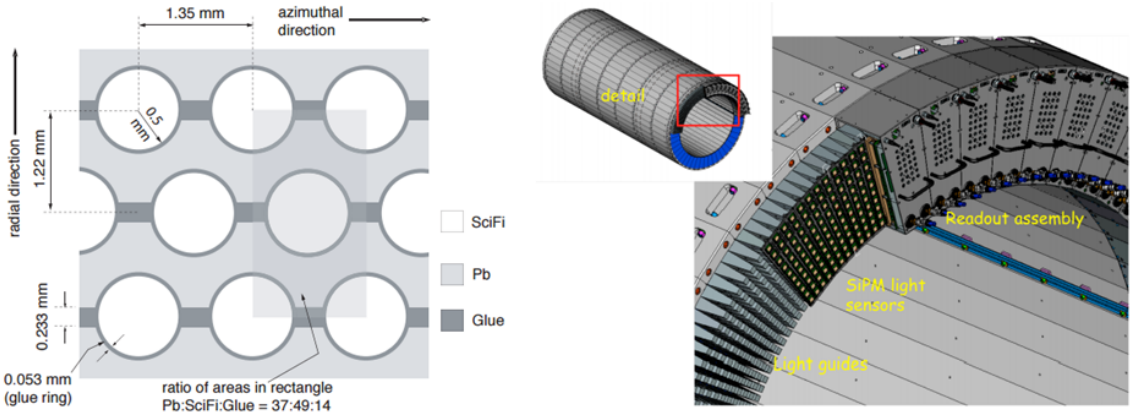

Figure 1.24: BCAL readout schematic. Left: lead and scintillating fiber matrix. Right: CAD drawing of the BCAL module readout system.

scintillating fibers in total which are embedded into 5 mm sheets of lead. Both ends of the modules are coupled to ultraviolet transmitting (UVT) acrylic light guides which are 8 mm in length and are wrapped in Tedlar to prevent cross-talk between adjacent light guides. For each of the 10 rows of light guides (seen in Fig. 1.24 (d)) the trapezoidal geometry of the light guides are designed so as to accommodate the unique module geometry as seen in Fig. 1.23. The base of each light guide is coupled to a Hamamatsu 144 mm^2 S12045 MPPC with an active area of 1.27×1.27 cm^2 *via* 500 μm air gap [8]. The partially assembled BCAL is shown in Fig. 1.26.

During the Spring 2015 commissioning run the BCAL was able to reconstruct electromagnetic showers so as to successfully identify the two photon decay of π^0 mesons through the decay $\pi^0 \to \gamma\gamma$ as seen in Fig. 1.25.

The FCAL has planar geometry orthogonal to the beam axis and is placed downstream (behind) of the forward TOF system and is shown in Fig. 1.26. The FCAL is composed of 2800, $4 \times 4 \times 45$ cm^3 lead glass F8-00 modules, stacked in a circular array, with each module coupled to a 12 stage FEU 84-3 PMT with custom IU Cockcroft-Walton bases. Fringe fields from the solenoid can distort energy mea-

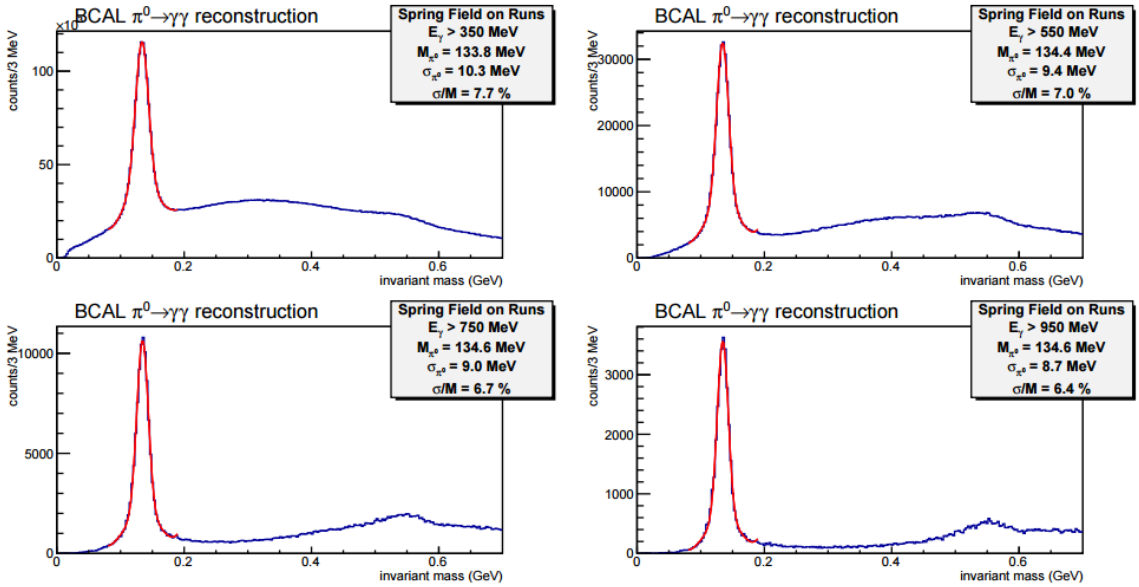

Figure 1.25: BCAL π^0 reconstruction. It is clear that the mass resolution of the π^0 improves with increasing shower energy as expected. [9].

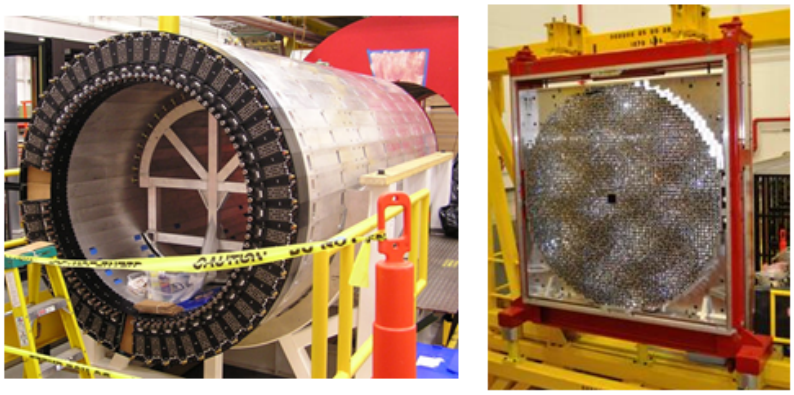

Figure 1.26: Assembled BCAL & FCAL. Left: partially assembled BCAL in Hall D. Fully assembled FCAL without dark room enclosure.

surements reported by the PMT's so 0.36 mm AD-MU-80 μ-metal was installed to provide magnetic shielding for the PMT's. Not shown in Fig. 1.26 is the dark box enclosure which measures 5 (deep) $\times$ 9 (wide) $\times$ 11 (high) ft^3 and keeps the FCAL light tight [8].

In the Spring 2015 commissioning run a severe lack of statistics made a reliable π^0 calibration of the FCAL impossible. However, with the limited statistics available

the π^0 mass resolutions as a function of photon energy is illustrated in Fig. 1.27. As a comparison, Fig. 1.28 shows the π^0 reconstructed mass resolutions obtained

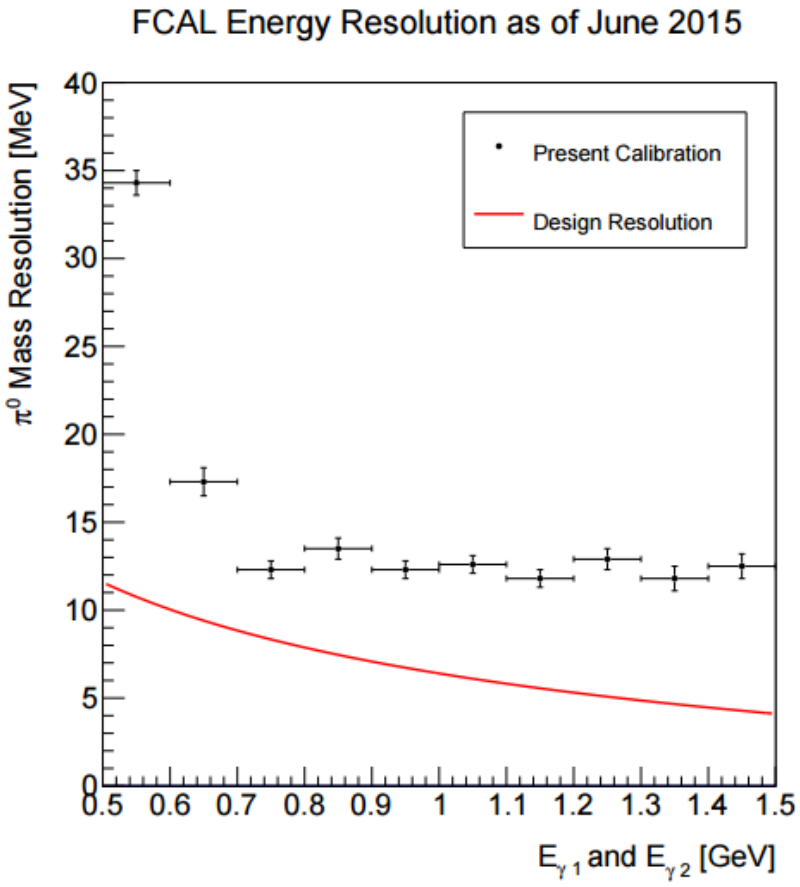

Figure 1.27: FCAL π^0 mass resolutions. Shown are the energies of the photons matched to the FCAL as a function of the minimum energy of the two decay photons. The solid red line is the design resolution while the points with errors are the current resolutions [9].

with the minimum data obtained from the Spring 2015 commissioning run.

1.3.3 Start Counter

The Start Counter (ST) detector, seen in Fig. 1.29, provides excellent solid angle coverage of $\sim 90\%$ of 4π, and a high degree of segmentation for background rejection. The purpose of the GlueX Start Counter is, in coincidence with the tagger, to

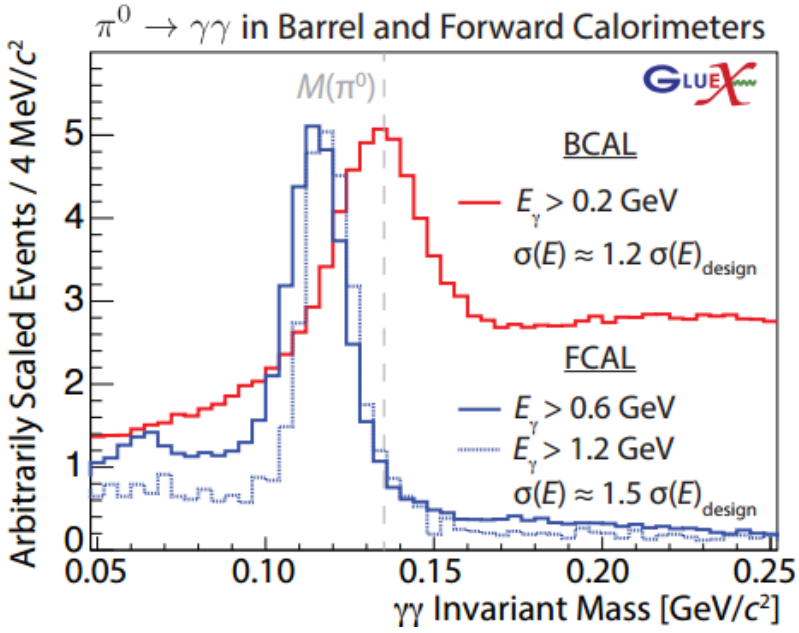

Figure 1.28: BCAL & FCAL π^0 reconstructed mass resolutions. It is clear that due to the lack of statistics the FCAL is far from design resolution. However, the BCAL is close to design resolution for small photon energies.

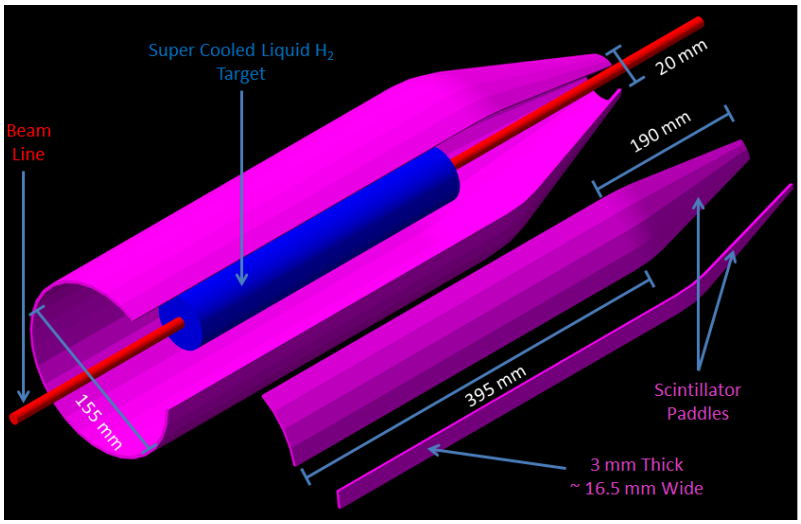

Figure 1.29: Start Counter geometry.

identify the electron beam bucket associated with the detected particles resulting from linearly polarized photons incident on a liquid H_2 target. It is designed to operate at tagged photon intensities of up to $10^8\,\gamma/\text{s}$.

The EJ-200 scintillator material from Eljen Technology, which provides a decay time on the order of 2 ns and a long attenuation length, was used in order to properly identify the beam buckets that are about 2 ns apart. The detector consists of an array of 30 scintillators with *pointed* ends that bend towards the beam at the downstream end. The support structure was kept at an absolute minimum in the active region of the detector and is made up of low density Rohacell. Silicon Photomultiplier (SiPM) detectors were selected as the readout system. These detectors are not affected by the high magnetic field produced by the superconducting solenoid magnet. Moreover, the SiPMs were placed as close as possible (< 250 μm) to the upstream end of each scintillator element, thereby minimizing the loss of scintillation light.

Each individual paddle of the Start Counter is machined from a long, thin, plastic (polyvinyl toluene) EJ-200 scintillator bar that was manufactured to be 600 mm in length, 3 mm thick, and 20 ± 2 mm wide, manufactured by Eljen Technology. Eljen Technology bent each scintillator around a highly polished aluminum drum by applying localized infrared heating to the bend region. The bent scintillator bars were then sent to McNeal Enterprises, a plastic fabrication company, where they are machined to the following desired geometry (see Fig. 1.30).

The paddles consist of three sections, described from the upstream to the downstream end of the target. First is the straight section, that runs parallel to the target cell, is 394.65 mm in length. Second is the bend region which is an 18.5° arc of radius 120 cm and is downstream of the straight section. Third is the tapered nose region, which is downstream of the target chamber, that bends towards the beam line to end at a height of 2 cm above the beam line.

After the straight bar was bent to the desired geometry, the two flat surfaces that are oriented orthogonal to the wide, top and bottom, surfaces were cut at a 6°

angle. During this process the width of the top and bottom surfaces are machined to be 16.92 mm and 16.29 mm wide, respectively. Each of the 30 paddles are rotated 12° with respect to the paddle that preceded it so that they form a cylindrical shape with a conical end. The geometry of the ST increases solid angle coverage while minimizing multiple scattering.

The 30 scintillator paddles are placed atop a Rohacell support structure that envelopes the target vacuum chamber seen in Fig. 1.31. Rohacell is a rigid, low density foam ($\rho = 0.075$ g/cm^3). The Rohacell, which is 11 mm thick, is rigidly attached to the upstream support chassis and extends down the length of paddles however, not to include the end of the conical section. Glued to the inner diameter of the Rohacell support structure are 3 layers of carbon fiber ($\rho = 1.523$ g/cm^3) which are 650 μm thick. A cross section of the ST can be seen in Fig. 1.31 where the carbon fiber is visible. The carbon fiber serves as to provide additional support during the assembly process as well as long term rigidity.

The SiPM detectors are held in a fixed position while being attached to the lip of the upstream chassis *via* two screws. The scintillators are placed as close as possible to the active region of the SiPMs (see Fig. 1.32).

The ST scintillators are coupled *via* an air gap ($< 250\mu$m) into groups of four SiPMs set in a circular arrangement. The individual SiPMs are single-cell SiPMs (Hamamatsu MPPC, S10931-50P) with a 3×3 mm^2 active area. Four individual SiPMs, grouped together in a linear array, are arranged such that they are parallel to the end of the upstream end of a scintillator as seen in Fig. 1.33.

Four SiPMs, reading out one individual paddle, are current summed prior to pre-amplification. The output of each preamp is then split, buffered for the Analog to Digital Converter (ADC) output, and amplified for the Time to Digital Converter (TDC) output by a factor five relative to the ADC. The ADC outputs are readout

via flash ADCs (JLab 250 MHz Flash, fADC250), while the TDC outputs are input into leading edge discriminators (JLab LE discriminator), followed by a 32 channel flash TDC (TDC JLab F1-TDC). Furthermore, each group of four SiPMs utilizes a thermocouple for temperature monitoring. There are 120 SiPMs in total, for a total of 30 pre-amplifier channels, as seen Fig. 1.34.

There are three components that comprise the SiPM detector and readout system. The first component is the ST1 which holds three groups of 4 SiPMs. The SiPMs are housed in a ceramic case, while being rigidly attached to the ST1. In order to mimic the geometry of the 30 paddle design one group (of four SiPM's) is offset by 12° relative to the central group, while another group is offset by -12°. One ST1 unit will collect light from three paddles individually. The ST1 implements the current sum and bias distribution per group of 4 SiPMs. It also has a thermocouple for temperature monitoring.

The second component is the ST2 which is a Printed Circuit Board (PCB) that houses the electronics of the readout system. It has three channels of pre-amplifiers, three buffers, and three factor five amplifiers. Furthermore, it has three bias distribution channels with individual temperature compensation *via* thermistors. The ST2 is attached to the ST1 *via* 90° hermaphroditic connector.

The third component, the ST3, provides interface to the power and bias supplies. It also routes the three ADC, and three TDC outputs as well as the thermocouple output. The ST3 connects to the ST2 emphvia a signal cable assembly. The ST3 is installed in the upstream chassis upstream of the Start Counter and next to the beam pipe seen in Fig. 1.35. Calibrations and performance of the ST will be discussed in chapter 4.

1.3.4 Time of Flight and Future Particle Identification

The time of flight (TOF) detectors are comprised of the forward TOF system as well as a portion of BCAL which was discussed in section 1.3.2. The forward TOF system consists of an array of, 2.54 cm thick and 6 cm wide, EJ-200 scintillator paddles coupled to 30 cm long fish-tail UVT polymethylmethacrylate (PMMA) light guides, readout on each end by Hamamatsu H105three4MOD PMT's. It has two planes of scintillator paddles. In one plane 84 paddles are stacked vertically, in the other 84 paddles are stacked horizontally to determine charged track multiplicity and provide excellent TOF information with respect to the accelerator RF beam buckets [7] and is shown in Fig. 1.36.

The TOF is positioned 550 cm downstream from the target center in front of the FCAL covering an area of 252×252 cm^2 with a 12×12 cm^2 central hole for the photon beam to pass through to the downstream FCAL. The TOF detector provides particle identification (PID) through the measurement of the particles velocity in the low momentum range [13]. The geometrical design of the TOF allows for the acceptance of charged tracks with polar angles $\theta \in [1^\circ, 11^\circ]$ [7].

During the Spring 2015 commissioning run the TOF performed in such a way that the per paddle time resolution met design resolution. Furthermore, it was able to successfully perform PID for $e's$, $\pi's$, $K's$, and $p's$ as illustrated in Fig. 1.37.

The FDIRC (forward detection of internally reflected Cherenkov) detector will significantly enhance the identification of kaons, as well as reduce the experimental backgrounds from misidentified particles, within the GlueX spectrometer so as to significantly enhance GlueX's ability to study hybrid mesons decaying into kaon final states. The FDIRC will be constructed utilizing 48 of the decommissioned synthetic fused silica bars, contained in four boxes, from the BaBar DIRC detector and is seen in Fig. 1.38 [15]. In addition the DIRC will allow for π/K separation up

to 4 GeV. A compact focusing optics system, $\sim 15,000$ channels, is currently being developed which will be read out with the CLAS12 RICH (ring imaging Cherenkov) MaPMT (multi-anode PMT) readout and electronics.

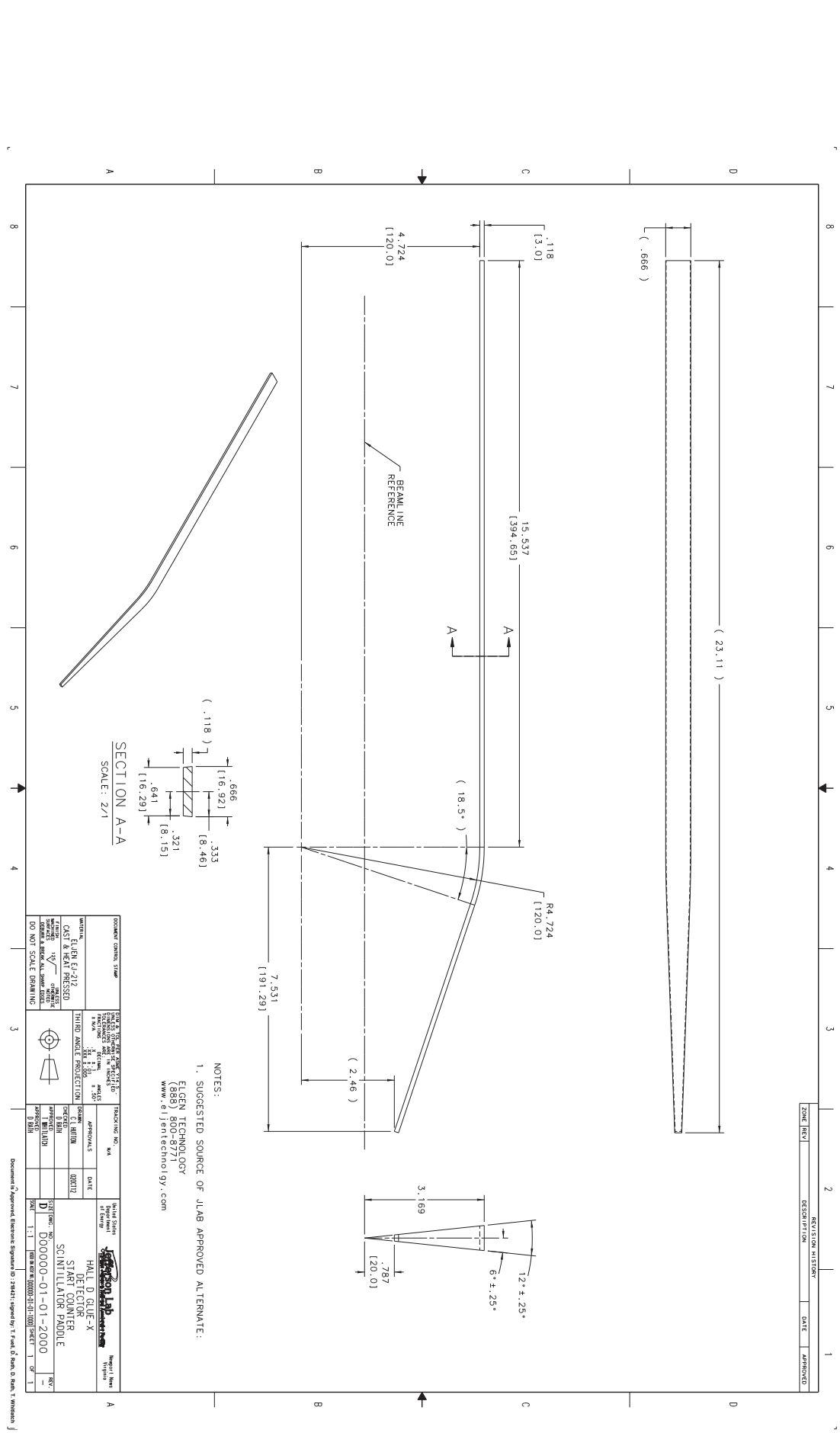

Figure 1.30: Start counter single paddle geometry.

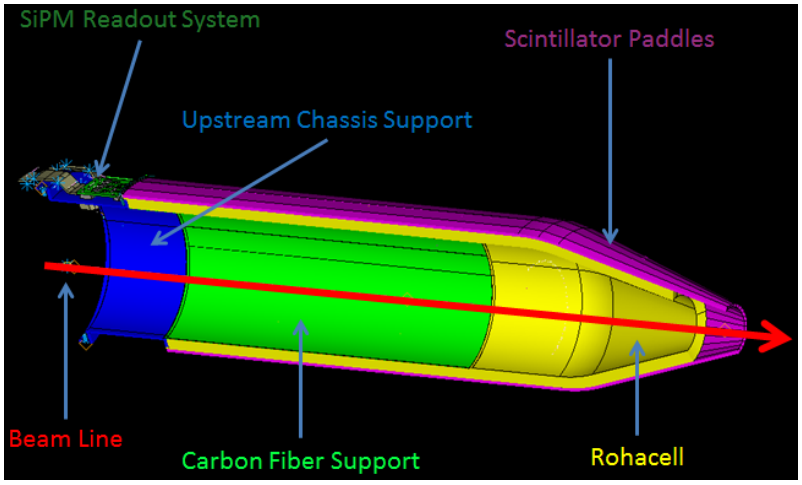

Figure 1.31: Cross section of the ST.

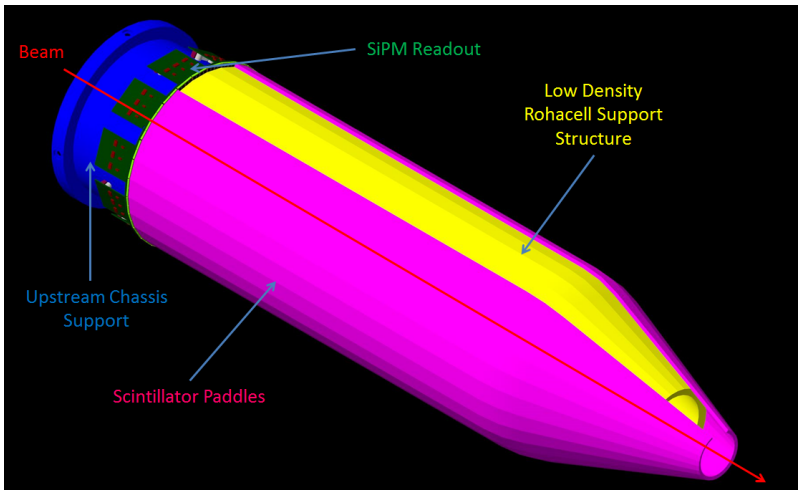

Figure 1.32: Partially assembled Start Counter.

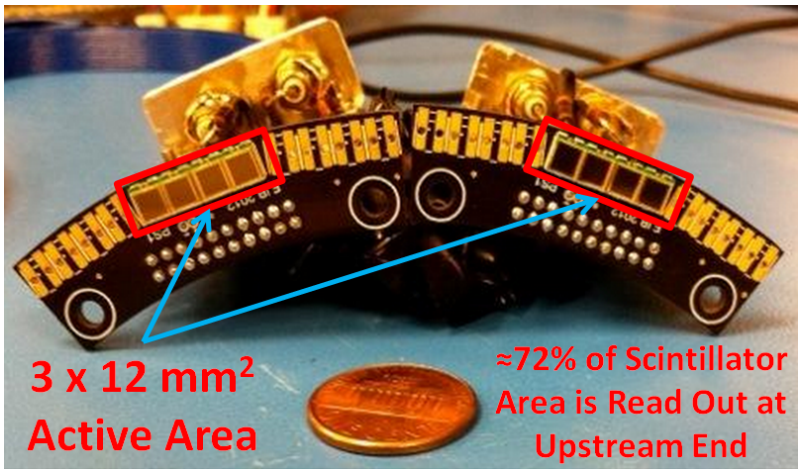

Figure 1.33: ST1 of SiPM.

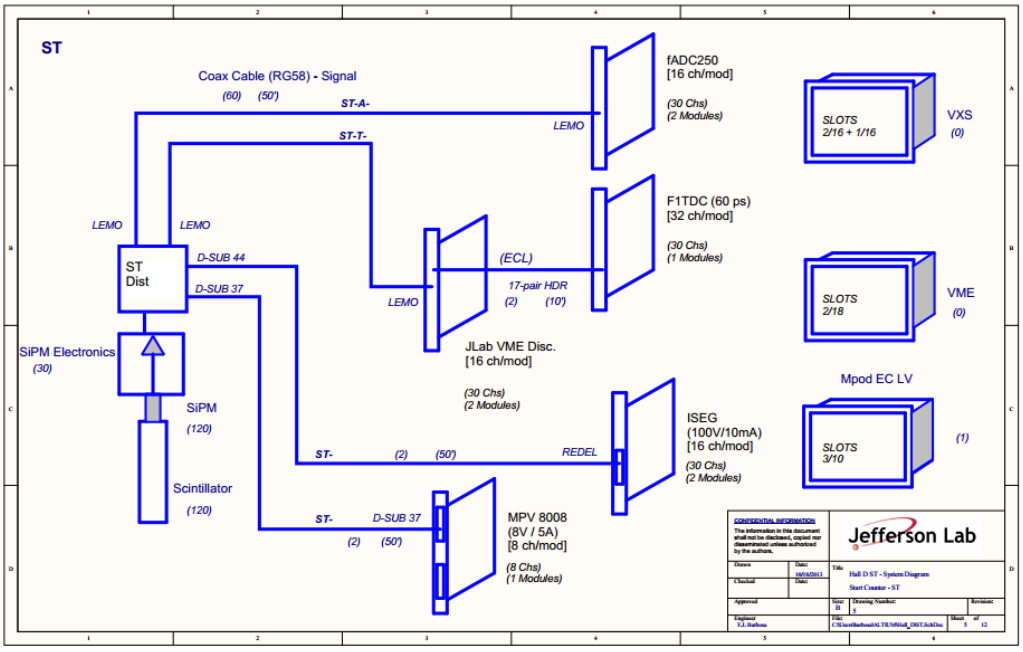

Figure 1.34: Start counter electronics.

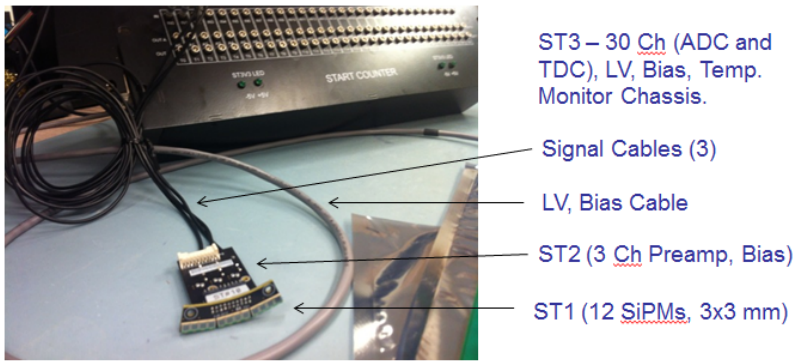

Figure 1.35: SiPM Readout System.

Figure 1.36: TOF wall. The horizontally stacked scintillators comprise the visible upstream plane, while the vertically stacked scintillators comprise the second down stream plane.

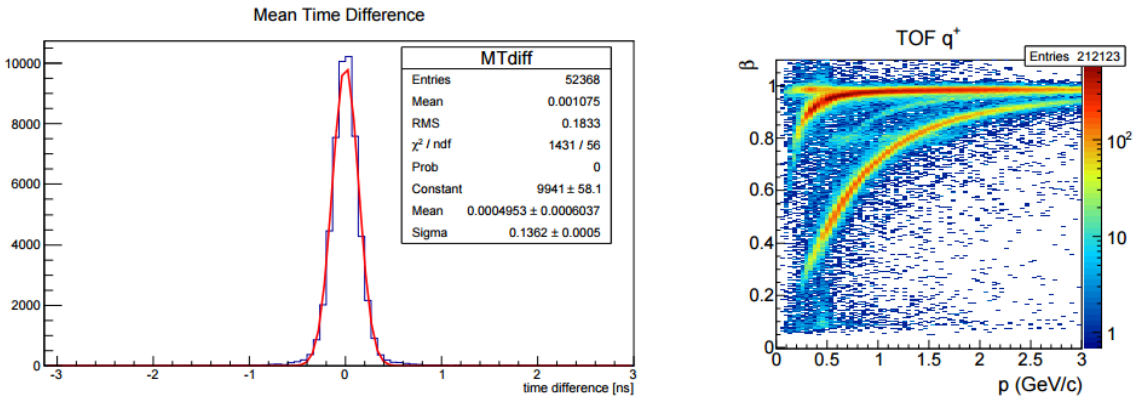

Figure 1.37: TOF performance in the Spring 2015 commissioning run. Left: the difference in hit mean times between two planes for charged tracks matched to the TOF. The resulting $\sigma \approx 1three6\ ps$ corresponds to $\sigma \approx 96\ ps$ resolution per plane. Right: $\beta\ vs.p$ for positively charged tracks. Bands corresponding to e^+, π^+, K^+, and p are clearly visible [9].

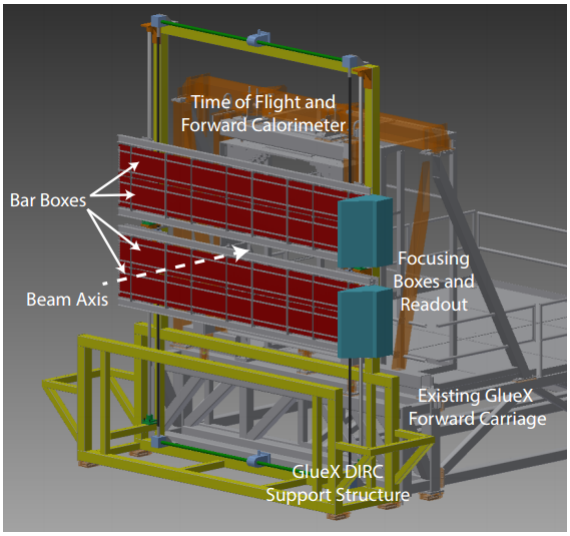

Figure 1.38: Conceptual drawing of the FDIRC [15]. The DIRC will be place upstream (in front) of the TOF and FCAL detector systems.

CHAPTER 2

Start Counter Research & Development

2.1 Prototype Scintillator Studies

Many data were collected at FIU regarding long thin scintillator bars, of different dimensions, and materials. Early studies aimed to determine the most optimal dimensions the scintillators should have in order to maximize the light output and minimize time resolution. As the nominal geometrical design required the ST scintillators to be 600 mm in length the optimal thickness and width were investigated.

2.1.1 Testing Straight Scintillator bars

A collimated ^{90}Sr source was used to produce minimum ionizing electrons at various locations along the length of the scintillator as seen in Fig. 2.1. A trigger PMT was

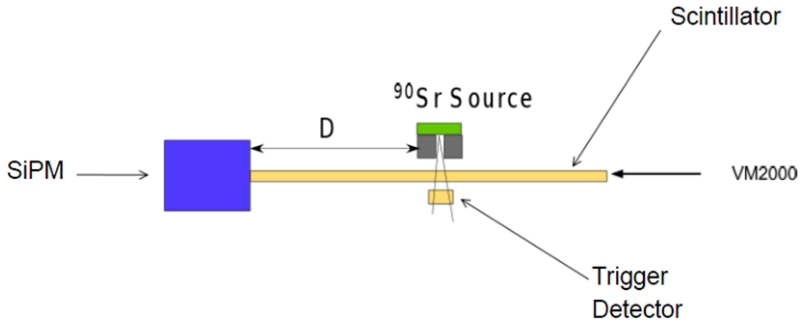

Figure 2.1: Straight paddle testing schematic.

used for timing purposes and either a fine mesh PMT or a BCAL prototype SiPM were used to read out the scintillator at one end. It is required to note that the SiPM results discussed in this section were taken at a time when the signal processing electronics had yet to be optimized and the results shown here are much worse than what was measured with the finalized SiPM readouts used in the ST. Furthermore,

it was known from the beginning of these studies that the ST scintillator paddles would be wrapped in a reflective material. Therefore, studies were also performed utilizing a strip of radiant mirror film produced by 3M adhered to the opposite end of the scintillator relative to the end which was being read out as seen in Fig. 2.1.

Quantifying the amount of light loss, or attenuation, in scintillators is usually measured in terms of the materials attenuation length. Light loss occurs in plastic scintillator material *via* escape of light through the scintillator boundaries and by absorption in the material. When the dimensions of the scintillator are such that the total path lengths travelled by the photons is comparable to the attenuation length, absorption can occur. This is the case for the Start Counter scintillators whose length is $\sim$ 600 mm. The attenuation length is defined to be the length in which the scintillation light intensity is reduced by a factor of $1/e$ (36.8%). Moreover, the functional form to describe light intensity as a function of length is given by $A(x) = A_0 e^{-x/a}$ where A_0 is the initial intensity, and a is the attenuation length. Therefore, the attenuation length of the scintillator material determines the number of photons arriving at the readout detector and therefore has significant influence on the time resolution.

Figure 2.2 illustrates attenuation measurements made for the $3 \times 15 \times 600$ mm^3 scintillator bar with and without VM2000 backing. Similar data were collected for scintillator bars with dimensions $2 \times 15 \times 600$ mm^3 and $3 \times 12 \times 600$ mm^3. These data were fit in an identical manner to Fig. 2.2 and the resulting attenuation lengths are summarized in Table 2.1.

The propagation speed of photons in the scintillator medium were also measured *via* the TDC data collected. The results of these studies are seen in Fig. 2.3. In most instances the effective velocity of light in straight scintillator bars is approximately 15 cm/ns which is clearly observed in the data.

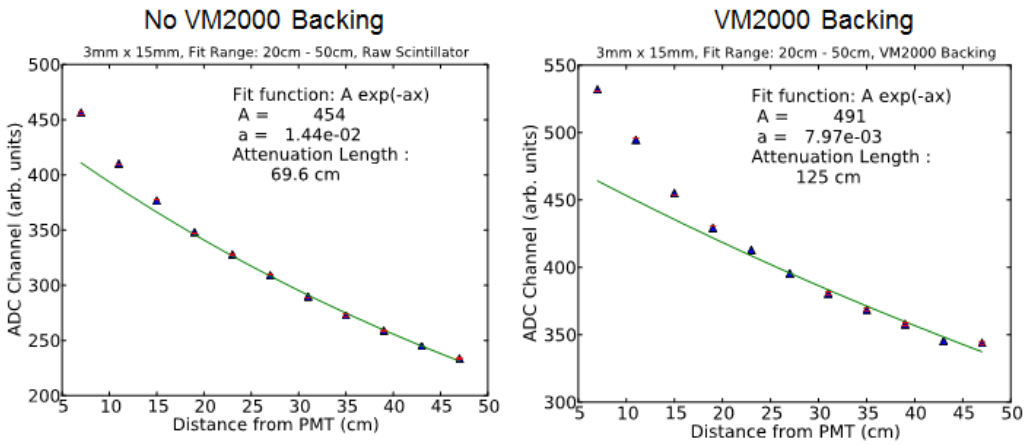

Figure 2.2: Attenuation length measurements for a straight scintillator bar. The dimensions of the bar are $3 \times 15 \times 600\ mm^3$. Left: No VM200 backing. Right: With VM200 backing. The fit range was limited to [20 cm, 50 cm].

Scintillator Dimensions (mm^3)	**Attenuation Length (cm) No VM200 Backing**	**Attenuation Length (cm) With VM200 Backing**
$2 \times 15 \times 600$	81.2	135.0
$3 \times 12 \times 600$	50.8	76.2
$3 \times 15 \times 600$	69.6	125.0

Table 2.1: Attenuation lengths of various scintillator dimensions. From these measurements it appears as though the 15 mm wide scintillators have the largest attenuation lengths.

While the attenuation length is in fact an important characteristic in scintillators, for the purpose of the ST the time resolution is in fact the most crucial parameter to have minimized. The time resolutions corresponding to various scintillator dimensions, without VM200 backing, are shown in Fig. 2.4. It is interesting to note that there exists a linear increase in time resolution as a function of source distance. It is clear from the data that the 2 mm thick scintillator performs the worst in terms of time resolution and was therefore no longer considered as a viable option for comprising the final ST design.

The time resolutions of the same scintillator bars with the VM2000 backing are shown in Fig. 2.5. It is interesting to note that there is no longer a linear increase

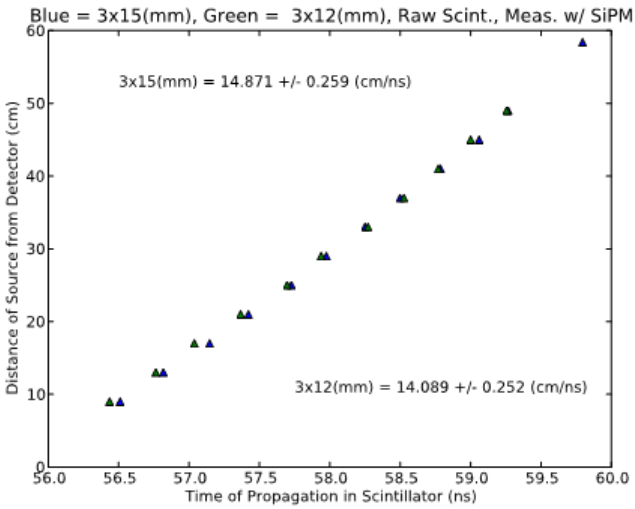

Figure 2.3: Propagation time of straight scintillator bars. The width of the scintillator bars does not effect the effective velocity of light in the scintillator medium which is to be expected.

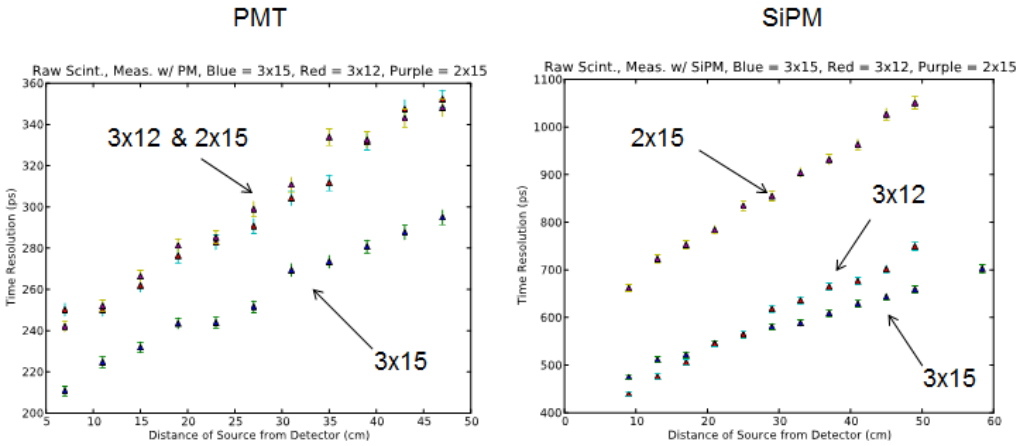

Figure 2.4: Time resolution measurements with no VM2000 backing. Left: PMT readout detector. Right: SiPM readout detector.

in time resolution as a function of source distance. Once the source gets sufficiently close to the end of the scintillator with the VM2000 backing, the light is reflected and ultimately detected. A table summarizing the time resolution measurements are given in Table 2.2. The $3 \times 15 \times 600$ mm^3 scintillator bar had the best time resolution regardless of the readout detector and whether or not there was VM2000 backing.

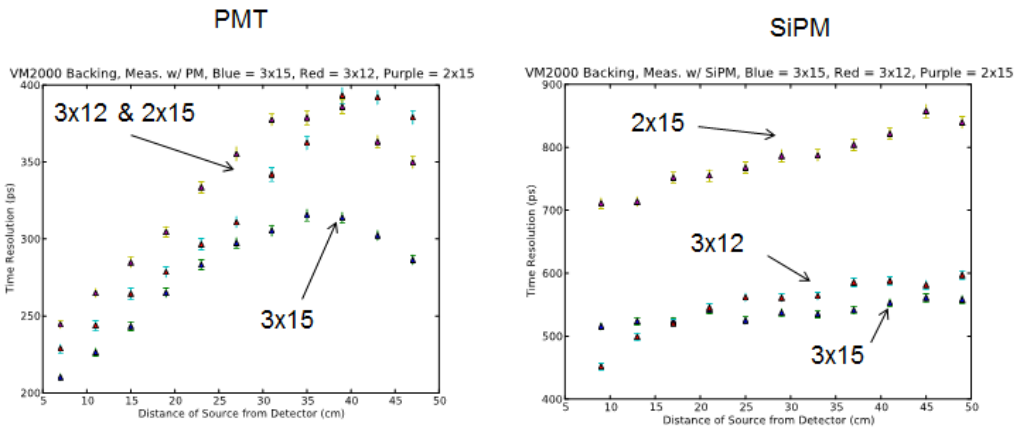

Figure 2.5: Time resolution measurements with VM2000 backing. Left: PMT readout detector. Right: SiPM readout detector.

Scintillator Dimensions (mm^3)	**SiPM Time Resolution (ps) No VM200 Backing**	**PM Time Resolution (ps) No VM200 Backing**	**SiPM Time Resolution (ps) VM200 Backing**	**PM Time Resolution (ps) No VM200 Backing**
$2 \times 15 \times 600$	$800 < \sigma < 1000$	$300 < \sigma < 350$	$720 < \sigma < 820$	$300 < \sigma < 400$
$3 \times 12 \times 600$	$500 < \sigma < 700$	$300 < \sigma < 360$	$500 < \sigma < 600$	$300 < \sigma < 400$
$3 \times 15 \times 600$	$550 < \sigma < 650$	$220 < \sigma < 300$	$520 < \sigma < 550$	$270 < \sigma < 320$

Table 2.2: Time resolutions of various scintillator dimensions.

As illustrated in Fig. 2.4, the $3 \times 15 \times 600$ mm^3 scintillator bar had the best performance in time resolution both with and without the VM2000 backing. This particular bar also had a good attenuation length as compared to the other bars. The data illustrated that the optimal dimensions of the paddles, relative the scintillators we had, were $3 \times 15 \times 600$ mm^3. However, for manufacturing purposes the straight scintillators bars were cut by Eljen into strips with the dimensions of $3 \times 20.3 \times 610$ mm^3 prior to bending and machining into the nominal design.

2.1.2 Fabricating Machined Scintillator Bars

Over the course of approximately two years, a company who could properly handle and machine the scintillators to the finalized geometry, seen in Fig. 1.29, was sought out. The first company Plastic-Craft [16], who machined scintillators for the

CTOF in Hall B, attempted to machine and polish scintillators to our standards. However, they proved unable to properly handle the scintillator material nor polish the machined edges to a standard that was suitable for the ST. Figure 2.6 shows the time resolution performance of a scintillator machined by Plastic-Craft. A sec-

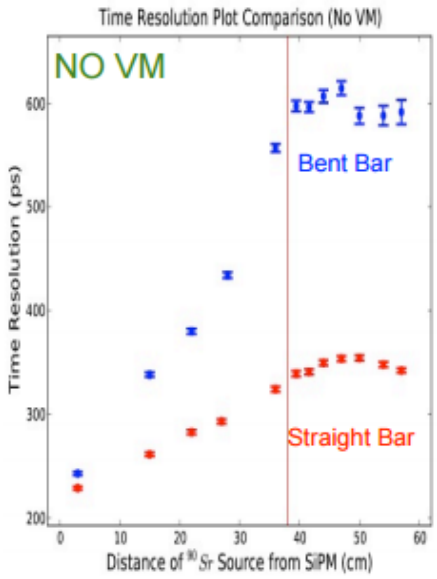

Figure 2.6: Machined scintillator by Plastic Craft. The red data points are the time resolutions of the straight bar. The blue data points are the time resolutions for the machined scintillator bar. The time resolution of the machined bar is almost a factor 2 worse than the straight bar. The red vertical line indicates where the bend region begins.

ond company, McNeal Enterprises [17] (McNeal), attempted to machine and polish prototype scintillators.

While McNeal seemed to be able to better machine the scintillator paddles to the designed geometry as compared to Plastic Craft, they had no experience with handling scintillator material. Thus, there was a steep learning curve for them. Initially, two scintillators machined to the desired geometry were ordered from McNeal. When they arrived at FIU it was discovered that one paddle was ruined during the machining process while the other scintillator possessed unsatisfactory light col-

lection properties and its performance began to quickly deteriorate. However, the performance of the scintillators machined by McNeal was significantly better than the scintillators machined by Plastic-Craft as can be observed by comparing Figs. 2.7 and 2.6.

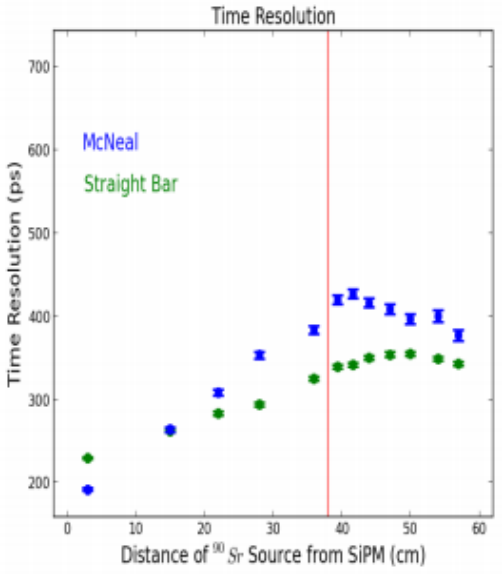

Figure 2.7: Machined scintillator by McNeal Enterprises. The green data points are the time resolutions of the straight bar. The blue data points are the time resolutions for the machined scintillator bar. There is no substantial difference ($\approx$ 40 ps) between the two bars. The red vertical line indicates where the bend region begins.

After approximately five months, the scintillator which survived the machining by McNeal began to show clear signs of crazing as seen in Fig. 2.8. The scintillator was then measured to see the effects that crazing imposes on a machined scintillator bar. The measurements are shown in Fig. 2.9.

A second batch of prototypes, consisting of 3 machined scintillators, was then manufactured by McNeal. Upon arrival at FIU it was discovered that one paddle had been broken during shipping. The remaining two paddles showed less than desirable initial time resolution measurements which was expected since both paddles had suffered large amounts of surface damage specifically in the bend region seen in

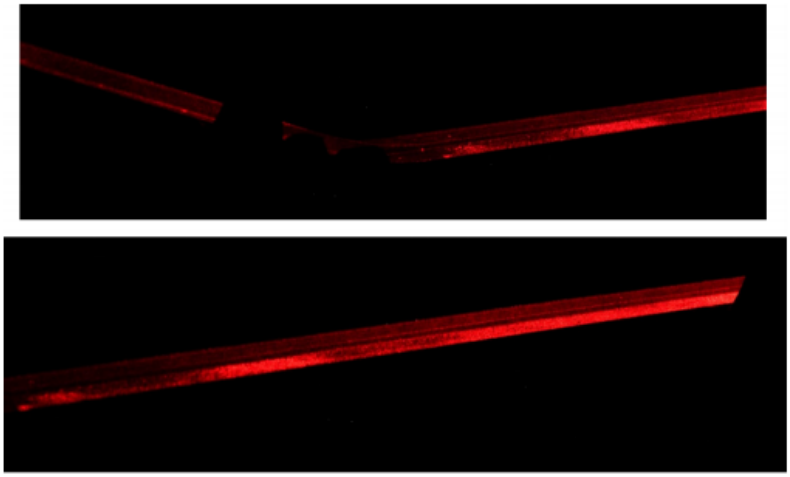

Figure 2.8: Crazing in first scintillator machined by McNeal. A diffuse laser was shone into the end of the straight section. Surface crazing is immediately obvious due to the large amount of light loss.

Fig. 2.10. Shortly after arrival the scintillators from the second batch began to deteriorate which is clearly visible in Fig. 2.9.

After lengthy discussions with the project manager at McNeal it was learned that they did not handle the scintillators correctly as a result of their ignorance in proper scintillator handling. They were ultimately provided with all the necessary materials needed to properly handle scintillator material and educated on its sensitive nature. The discussions also led to the decision for Eljen to perform the bending of the scintillators prior to being machined by McNeal.

A third and final prototype batch consisting of five machined scintillators was ordered from McNeal. Upon arrival at FIU it was learned that all five machined scintillators had survived both the machining and shipping process. Moreover, the quality of the scintillators appeared to be far superior to what was observed with the previous two batches as can be seen in Fig. 2.11.

Machined scintillator paddles from the third batch were monitored closely for possible signs of deterioration. Figure 2.12 shows the time resolution measurement

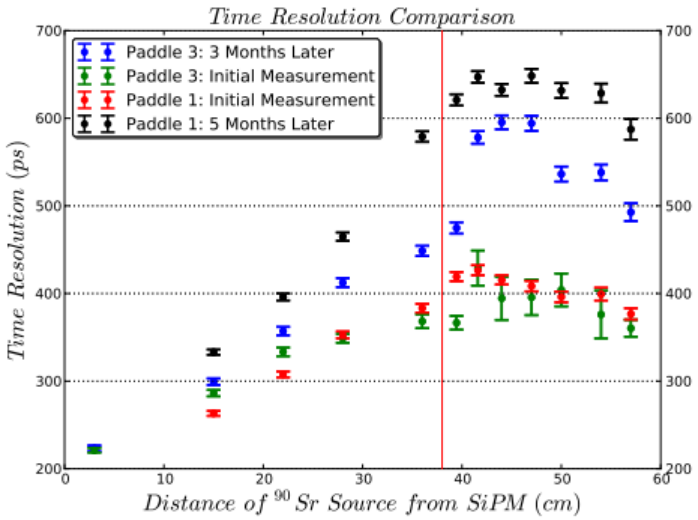

Figure 2.9: Deterioration in scintillators machined by McNeal. An average reduction of ≈ 175 *ps* in time resolution is observed over the course of five months. Paddle 1 was from the first batch of machined scintillators while paddle 3 was from the second.

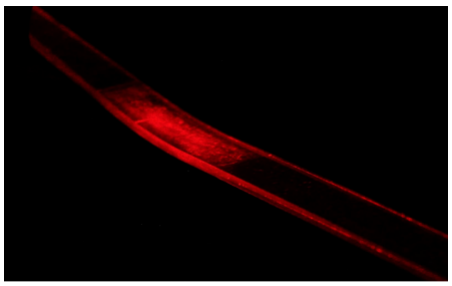

Figure 2.10: Scratches in bend region of McNeal's machined scintillators. A diffuse laser was shone into paddle 3 of the second batch at the wide end of the straight section.

data for all five prototype paddles. It was immediately obvious that the third batch of scintillators were far superior to any others received in the previous batches. Aside from paddles 1 and 3, which were erroneously handled with medical examining gloves which had lotion deposits on the surface of the gloves, no paddles seemed to show any observable signs of deterioration. The third batch of prototype scintillators proved that with Eljen performing the precision bend and McNeal performing the

Figure 2.11: Good quality machined scintillators from McNeal. This was paddle 1 from the third batch. It is useful to note that there are no locations along the surface of the scintillator where numerous scratches have occurred.

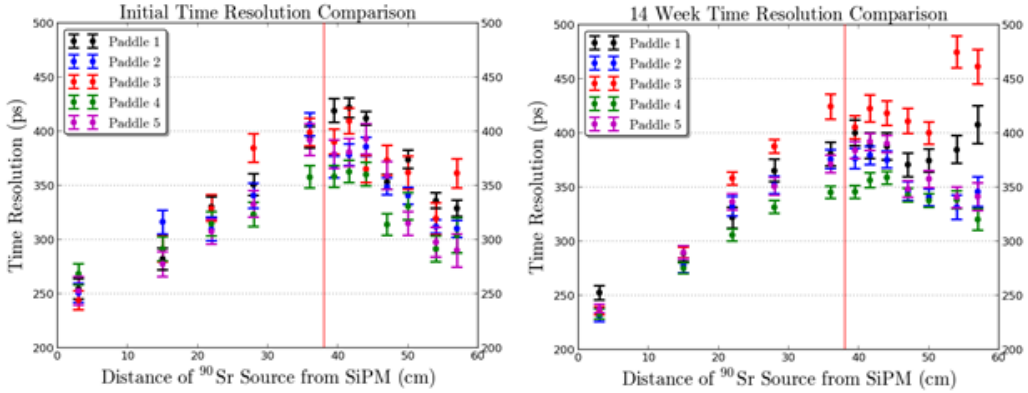

Figure 2.12: Deterioration monitoring of the third prototype batch from McNeal. Left: time resolution measurements of all five paddles taken immediately upon arrival. Right: time resolution measurements of all five paddles taken three and a half months after arrival.

machining to the desired geometry, the ST scintillator paddles could meet, if not exceed, the design time resolution of 350 ps.

2.2 Wrapping Studies

Wrapping scintillators in reflective materials has many advantages. Not only does the reflective material enhance the overall performance, it protects the surface of the scintillator from incurring any damage from handling. Another advantage is that

the reflective material reduces the amount of cross talk between adjacent scintillator paddles.

2.2.1 Wrapping Prototypes in Reflective Materials

A few different reflective materials were investigated as potential materials which would be wrapped around the individual ST scintillators paddles. While VM2000 from 3M has extremely good reflective properties it is quite thick $\approx$ 75 μm and not very malleable. Thus, it was decided that VM2000 was not a viable candidate for wrapping the individual ST paddles. Instead, studies were carried out while wrapping the machined prototypes with 2 μm thick aluminized Mylar and food grade Reynolds Wrap® aluminium foil which is 16.5 μm thick. Figure 2.13 shows a machined scintillator paddle wrapped in the two aforementioned reflective materials.

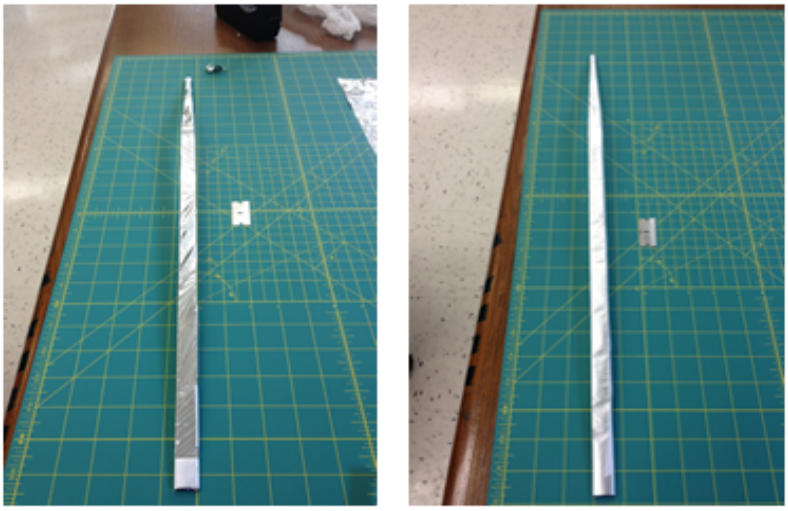

Figure 2.13: Machined scintillators wrapped in reflective materials. Left: 2 μm aluminized Mylar. Right: 16.5 μm aluminum foil.

While the prototype was wrapped, the scintillators were tested in a similar manner to what was discussed in section 2.1.1. Figure 2.14 shows the results of the

measurements. The tests concluded that there was no substantial difference in per-

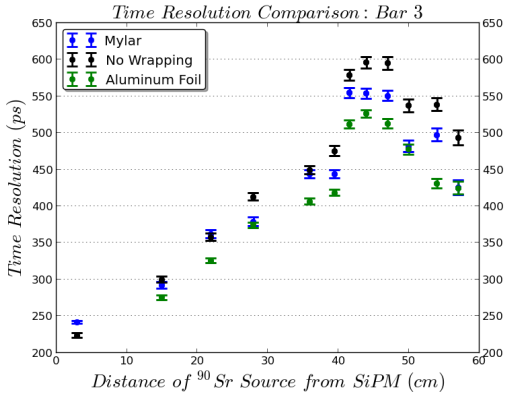

Figure 2.14: Time resolutions of wrapped machined scintillators. It is interesting to note the drastic improvement in time resolution as the source moves further away from the SiPM in the nose region.

formance enhancement among the Mylar and Al foil wrapping. However, it was learned that 2μm aluminized Mylar is quite difficult to work with when attempting to wrap machined scintillator paddles while the Al foil proved relatively simple. Therefore, it was decided to wrap the machined scintillator paddles with Al foil. A systematic procedure for wrapping machined scintillator paddles in Al foil was eventually developed and implemented.

2.2.2 Cross-Talk Measurements

If two scintillators are placed adjacent to one another it is possible that light travelling in one scintillator can escape the scintillator medium and enter into the medium of the adjacent scintillator. Assuming there are two independent detectors collecting light from each respective scintillator, then some amount of light detected by the detectors could in fact have originated from the adjacent scintillator. This phenomenon is known as cross-talk. Cross-talk is something to be minimized when dealing with arrays of adjacent scintillators such as the ST.

To perform cross talk measurements the gain of the PMT being used in the measurements was required to be known. To measure the gain of a PMT one must analyze the single photo-electron (SPE) spectrum. The SPE spectrum was produced with a light emitting diode (LED) which sends pulses of light to the photocathode of a Photonis XP2262 PMT which had a mask of Tedlar, cut to the dimensions of the scintillator paddle (3×15 mm^2). The Tedlar mask ensured that the area of the photocathode that was being illuminated by the LED source was identical to the area of the end of a machined scintillator paddle. The LED source was then varied in intensity until the SPE spectrum was clearly visible in the ADC data.

To determine the gain of a PMT the procedures outlined in [18] were followed to fit the SPE spectrum. It is assumed that the distribution of the number of photoelectrons released *via* the photoelectric effect due to the photons generated by the LED source, is governed by Poissonian statistics. The probability ($P(n;\mu)$) that n photoelectrons will be observed with a mean (μ) number of photons incident on the photocathode is given by Eq. 2.1. Furthermore, μ is defined to be the mean number of photoelectrons collected by the first dynode in the PMT.

$$P(n;\mu) = \frac{\mu^n e^{-\mu}}{n!} \tag{2.1}$$

It is useful to note that the parameter μ is dependent on the light intensity of the LED, the quantum efficiency of the PMT's photocathode, as well as the electron collection efficiency of the PMT's dynodes.

The backgroundless signal response of a PMT can be described by the convolution of a Poisson distribution and a convolution of a Gaussian distribution corresponding to the PMT output charge distribution when n photoelectrons are collected at the first dynode and is given by Eq. 2.2.

$$S_{ideal}(x) = P(n;\mu) \otimes G_n(x) = \sum_{n=0}^{\infty} \frac{\mu^n e^{-\mu}}{n!} \frac{1}{\sigma_1 \sqrt{2\pi n}} e^{-\frac{(x - nQ_1)^2}{2n\sigma_1^2}} \tag{2.2}$$

The 1 index corresponds to the Gaussian variables associated with the PMT response if a single photoelectron was collected at the first dynode. Assuming the background events contributing to the total charge collected by the PMT is given by a convolution of a Gaussian and an exponential discussed in [18], then the realistic PMT signal response distribution is given by the convolution seen in Eq. 2.3.

$$\begin{aligned} S_{real}(x) &= \int S_{ideal}(x')B(x-x')dx' \\ &= \sum_{n=0}^{\infty} \frac{\mu^n e^{-\mu}}{n!}[(1-w)G_n(x-Q_0) + wI_{G_n\otimes E}(x-Q_0)] \end{aligned} \tag{2.3}$$

Where $I_{G_n\otimes E}(x-Q_0)$ is given by Eq. 2.4.

$$I_{G_n\otimes E}(x-Q_0) = \int_{Q_0}^{x} G_n(x'-Q_0)\alpha e^{-\alpha(x-x')}dx' = \frac{\alpha}{2}e^{-\alpha(x-Q_n-\alpha\sigma_n^2)} \times \left[\text{erf}\left(\frac{|Q_0-Q_n-\sigma_n^2\alpha|}{\sigma_n\sqrt{2}}\right) + \text{sign}(x-Q_n-\alpha\sigma_n^2) \times \text{erf}\left(\frac{|x-Q_n-\sigma_n^2\alpha|}{\sigma_n\sqrt{2}}\right)\right] \tag{2.4}$$

It is useful to note that Q_0 & σ_0 define the pedestal and Q_1 & σ_1 define the single photoelectron peak. Moreover, the n^{th} photoelectron peak is given by $Q_n = Q_0 + nQ_1$ and the variance is $\sigma_n^2 = \sigma_0^2 + n\sigma_1^2$. The parameters w and α are parameters defining the exponential background.

Fitting Eq. 2.3 with parameters Q_n, σ_n, w, μ and α as fit parameters to ADC data collected in the manner previously discussed, allowed the gain of the Photonis XP2262 PMT to be determined and is given by the parameter Q_1 [18]. It is useful to note that up to fifteen photoelectron peaks were used to fit the SPE ADC data when only four fits were drawn in Fig. 2.15.

With the gain of the Photonis XP2262 PMT known it was then possible to perform cross talk measurements for two machined scintillators placed adjacent to each other with one scintillator rotated 180° relative to the other. The scintillator edges were arranged such that the edges were flush against one another so as to

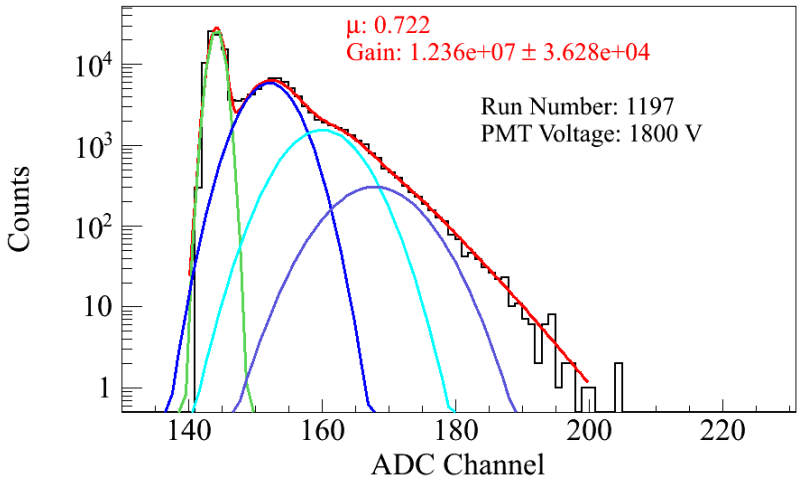

Figure 2.15: Determination of the gain for the Photonis XP2262 PMT. The red line is the fit to the SPE spectrum utilizing the convolution function given by Eq. 2.3. The green line is the fit to the pedestal. The blue line is the fit to the SPE peak, the cyan line is the two photoelectron peak and the purple line is the three photoelectron peak

simulate the arrangement of adjacent scintillators in the final ST configuration. One scintillator was read out at the upstream end by a SiPM while the adjacent scintillator was readout by the Photonis XP2262 PMT, whose gain was known, which had been masked with Tedlar as was discussed in the gain calibration. Data were then collected by alternating a collimated ^{90}Sr source coupled to the wide flat surface of the adjacent scintillators as seen in Fig. 2.16 with and without reflective material (Al foil and 2 μm aluminized Mylar) placed between the adjacent scintillators.

After the six sets of SPE ADC data were collected, the spectra were fit utilizing the function given by Eq. 2.3 with the gain factor parameter Q_1 fixed to the gain factor of the Photonis XP2262 PMT which was determined previously. The SPE ADC data and corresponding fits when no reflective material had been placed between the two adjacent machined scintillators is show in in Fig. 2.17. The SPE ADC data and corresponding fits when Al foil had been placed between the two adjacent machined scintillators is show in Fig. 2.18. It is useful to note that the Al

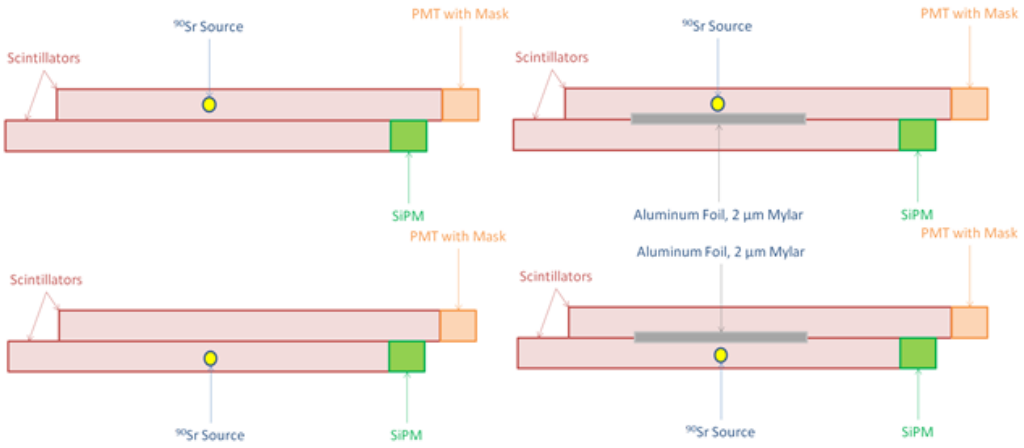

Figure 2.16: Experimental set-up for cross talk measurements. Top left: source coupled the scintillator being readout by the Photonis XP2262 PMT with no reflective material between adjacent scintillators. Bottom left: source coupled the scintillator being readout by the SiPM with no reflective material between adjacent scintillators. Top right: source coupled the scintillator being readout by the Photonis XP2262 PMT with reflective material between adjacent scintillators. Bottom right: source coupled the scintillator being readout by the SiPM with reflective material between adjacent scintillators.

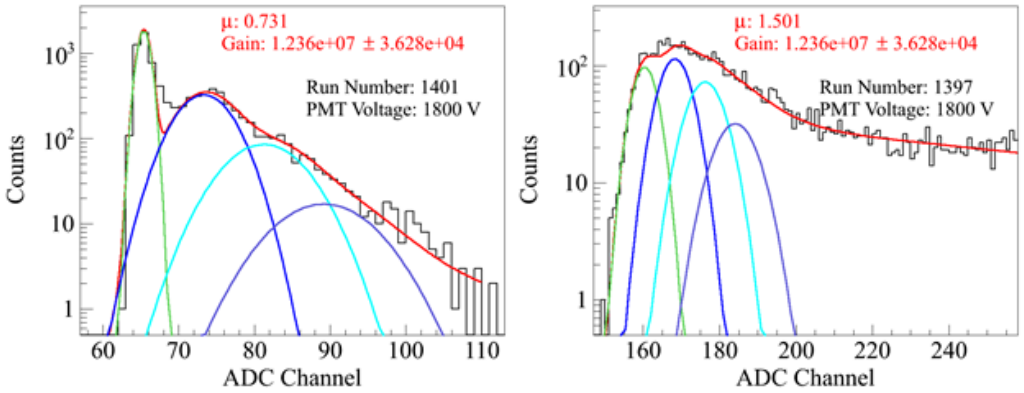

Figure 2.17: Single photoelectron spectrum with no reflective foil. ADC spectrum as read out by the Photonis XP2262 PMT with no reflective foil placed between the adjacent machined scintillators. Left: source coupled to scintillator being read out by the SiPM. Right: source coupled to scintillator being read out by the Photonis XP2262 PMT.

foil was oriented such that the reflective side was always flush against the edge of the scintillator which had the source coupled to it. For brevity only the Al foil and no reflective material are shown.

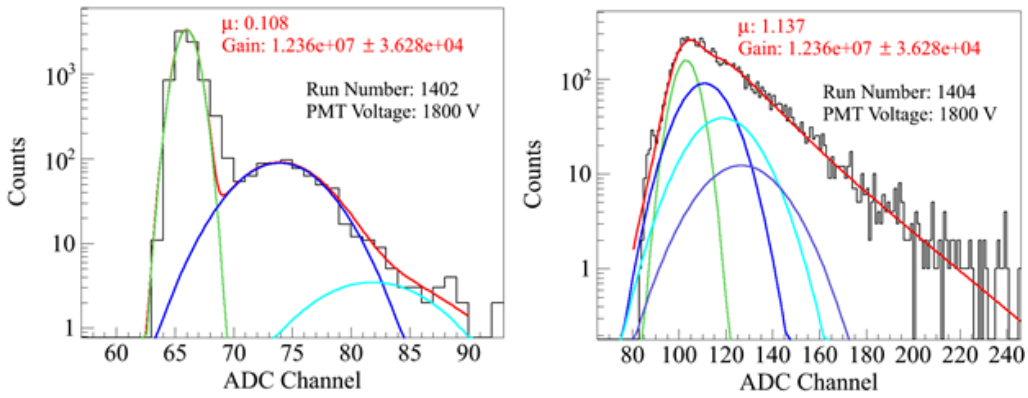

Figure 2.18: Single photoelectron spectrum with Al foil. ADC spectrum as read out by the Photonis XP2262 PMT with Al foil placed between the adjacent machined scintillators. Left: source coupled to scintillator being read out by the SiPM. Right: source coupled to scintillator being read out by the Photonis XP2262 PMT.

The parameter of importance, the mean number of photoelectrons collected by the first dynode μ, was extracted from the aforementioned fits. Effectively, μ is proportional to the intensity of the light source [18]. Therefore, the mean number of photoelectrons collected by the first dynode in the Photonis XP2262 PMT when the source was coupled to the scintillator read out by the SiPM (μ_{SiPM}), and similarly when the source was coupled to the scintillator read out by the Photonis XP2262 PMT (μ_{SiPM}), is a measure of how much cross talk exists between the two adjacent machined scintillators. The results of the cross talk measurements are summarized in Table 2.3.

Reflective Material	**SiPM**	**PMT**	$\mu_{\mathbf{SiPM}}/\mu_{\mathbf{PMT}}$
None	$\mu_{SiPM} = 0.713$	$\mu_{PMT} = 1.501$	48.7 %
Aluminum Foil	$\mu_{SiPM} = 0.108$	$\mu_{PMT} = 1.137$	9.5 %
2 μm Mylar	$\mu_{SiPM} = 0.129$	$\mu_{PMT} = 1.362$	9.5 %

Table 2.3: Results from cross talk studies.

From the data it is clear that having reflective material between two adjacent scintillator paddles reduces cross talk by nearly a factor of five. The data also show that there is no difference in the reduction of cross talk when using Al foil and 2 μm

aluminized Mylar. Due to the inherent difficulty of wrapping machined scintillators with 2 μm aluminized Mylar and no clear enhancement of scintillator performance relative to Al foil, it was decided that the machined scintillators comprising the ST would be wrapped in Al foil.

2.3 GEANT4 Simulations

Monte Carlo (MC) simulations were conducted in order to better understand the performance and characteristics of scintillators machined to the 30 paddle design of the GlueX Start Counter. Comparisons were made with the data observed in experiments conducted on the bench at FIU. The MC studies were performed with the use of the simulation tool-kit GEANT4 which simulates the passage of particles through and interacting with matter [19].

2.3.1 Simulating a Simplified Model of the ST

As discussed previously, the scintillator paddles comprising the ST have a unique geometry in which the nose section tapers down in width as the paddles approach the beam line. The tapering effect caused for a unique phenomenon in which the light output of the paddle begins to increase as the source moves further away from the readout detector. At first, this phenomenon is completely contrary to what one might expect. When the source moves further away from the end being readout the photons have a larger effective path length and thus have an increased probability in light being lost for detection.

A primitive GEANT4 simulation was conducted to investigate if the unique geometry of the nose section was responsible for the increased light collection as the source moved further away from the readout detector. For simplicity and robustness

only the two trapezoidal regions of a machined scintillator bar were considered. Namely, the wide straight section and the tapered nose section which are illustrated in the GEANT4 event display seen in Fig. 2.19.

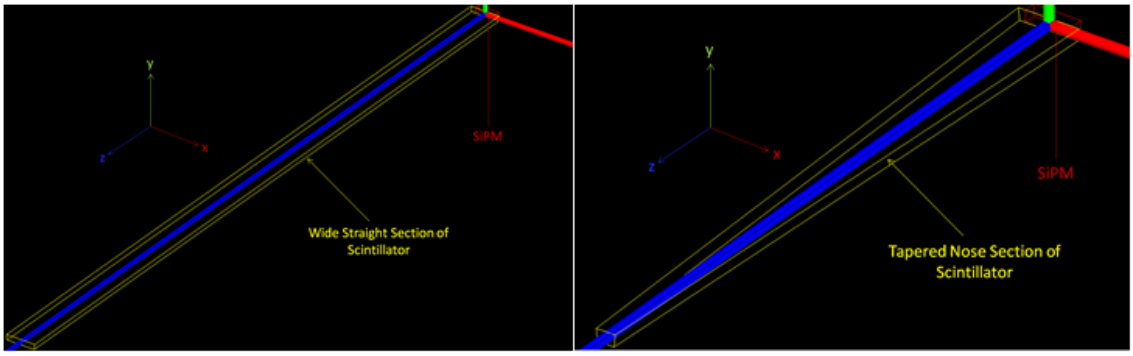

Figure 2.19: Simulated straight & nose section geometries. Shown is the GEANT4 event display. Left: wide straight section. Right: tapered nose section. The sections have been oriented such that they are in the same coordinate system as defined in HallD. The yellow lines are the scintillator boundaries, while the red lines are the boundaries of the SiPM.

The EJ200 scintillator material ($\rho = 1.023$ g/cc^3, $n = 1.58$) [20] was simulated with only one free parameter utilized to characterize the scintillator bar *i.e.*, the reflectivity of the G4LogicalSkinSurface, was set to 98% so there remained some finite probability that photons could be lost in the scintillator medium. Furthermore, the SiPM readout detector was placed at the wide end of the two sections, seen in Fig. 2.19, and was constructed as a G4SensitiveDetector made of Silicon with a 100% detection efficiency.

In order to simulate a charged particle traversing through the scintillator medium resulting in the production of photons along its path through the material, optical photons were generated inside the simulated scintillator. The scintillation yield was defined to be $10,000\gamma's/$ 1 MeV [20]. For visual purposes, Fig. 2.20 shows 100 optical photons being produced at the tip of the far end of the two sections of the simulated scintillator paddle.

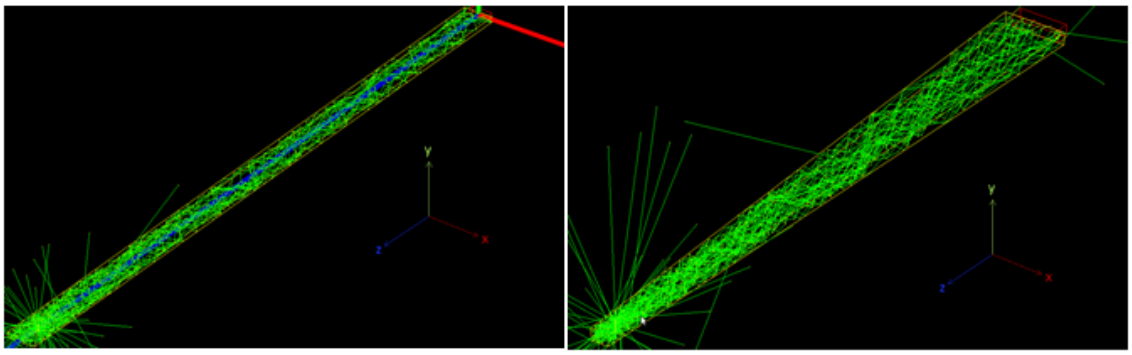

Figure 2.20: 100 Optical photons generated in the staight & nose sections. Left: wide straight section. Right: tapered nose section. The neon green lines are the paths of the optical photons. It is clear that some photons do in fact escape the scintillator medium, while others are collected in the simulated SiPM detector.

In order to sample the entirety of the two sections 10,000 optical photons were generated at 16 different locations inside the medium of the scintillator. The photon

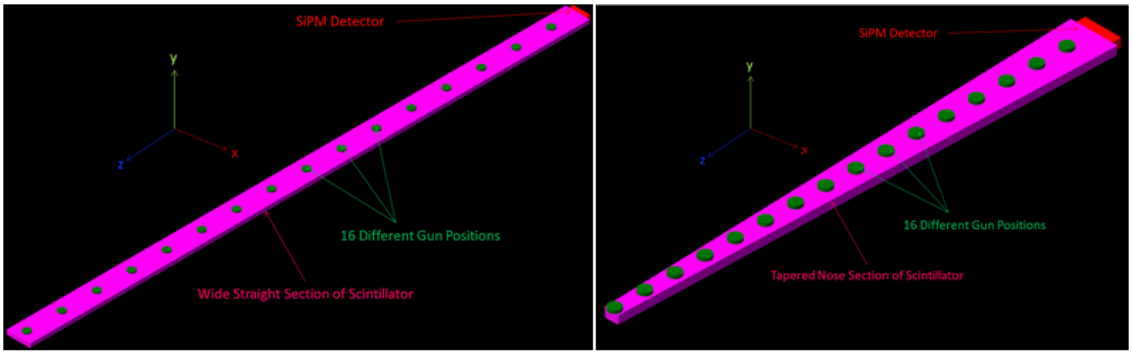

Figure 2.21: Optical photon gun locations along the straight & nose sections. Left: wide straight section. Right: tapered nose section. The magenta geometries indicate the scintillator boundaries of the two sections. The red box is the sensitive SiPM detector, and the green cylinders represent the location of the 16 optical photon gun locations. The locations of the source were chosen to be equal distances apart relative to each of the two sections.

energies ranged between $0.5 - 3.0$ eV [21] and were generated randomly in 4π along a 3 mm path $(y - axis)$ in the scintillator medium, orthogonal to the wide surface of the scintillator so as to simulate a charged particle traversing through the scintillator medium with a $\theta_{track} = 90^{\circ}$ in hall coordinates. The number of photons collected by

the SiPM at each of the 16 source locations is counted and correlated to the source location. The results can be seen in Fig. 2.22. From the data it is clear that the

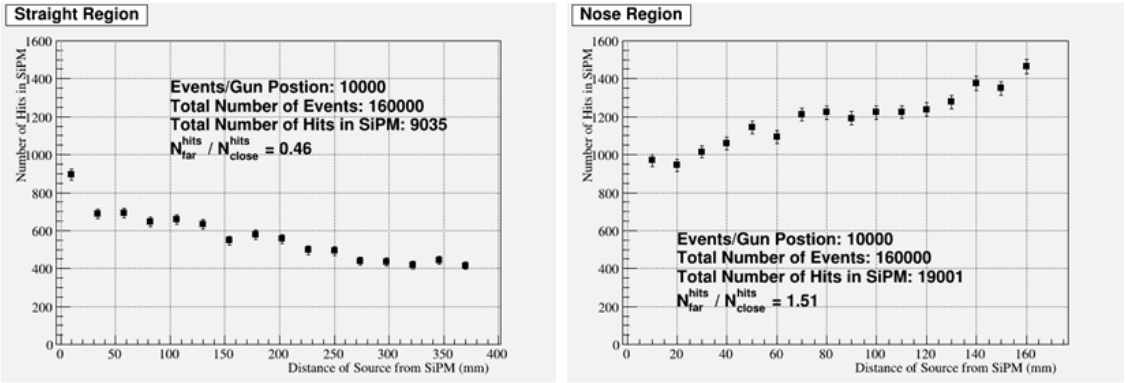

Figure 2.22: Simulation results for simplified two section scenario. The total number of photons which were collected by the SiPM detector at each of the 16 source locations is plotted against the sources distance from the sensitive detector. Left: wide straight section. Right: tapered nose section.

unique geometry of the nose sections causes an improvement in light collection as the source moves further away from the readout detector. In fact, there is a factor $\approx 1/2$ light loss observed in the straight section upon comparing the number of hits collected at the closest and furthest locations relative to the readout detector. However, there is factor $\approx 3/2$ light gain observed in the nose region. These results are primarily due to the unique scintillator geometry. This phenomenon is advantageous in the case of the ST since the majority of forward going charged particles will traverse through the nose region.

2.3.2 Simulating the Machined Scintillator Geometry

Further simulations were conducted by P. Khetarpal [22] to simulate more realistically the effects of light collection that results from the unique ST scintillator geometry and optical surface quality.

The ST scintillator geometry was imported into GEANT4 from a Vectorworks CAD drawing utilizing the CADMesh utility [23] and can be seen utilizing the GEANT4 event display in Fig. 2.23. The SiPM was constructed as a $12 \times 12 \times$

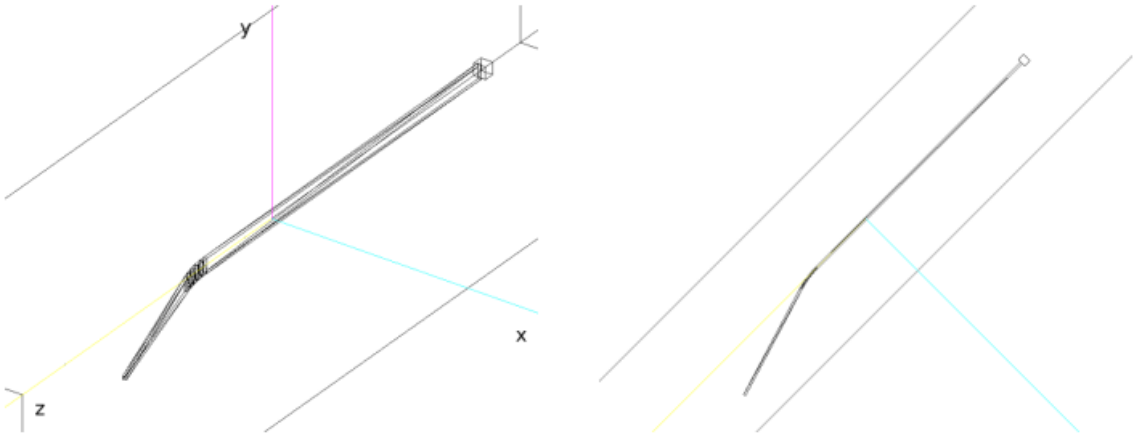

Figure 2.23: Scintillator geometry imported into GEANT4 utilizing CADMesh Utility. The scintillator is coupled to a SiPM detector. Left: isometric view. Right: top view. The tapering of the nose section is clearly visible.

10 mm^3 volume with a 100 μm air gap between it and the wide end of the straight section. Furthermore, the volume surrounding the scintillator volume was air. The EJ-200 scintillator material, SiPM silicon detector, and optical photons were defined in an identical manner discussed in section 2.3.1.

To simulate the imperfections, due to the manufacturing and machining, on the scintillator surfaces an optical surface "skin" was defined to exist on the the scintillator surfaces and between the surrounding air. The material was defined to be of they type "dielectric-dielectric" and made use of the UNIFIED physics model [24] to define an imperfect scintillator surface. Both the transmission efficiency and reflection parameters were implemented as free parameters to study their various effects on light transmission.

The UNIFIED model allows one to define the finish of the scintillator surface as *polished*, *ground*, or *unified* and is illustrated in Fig. 2.24 [24].

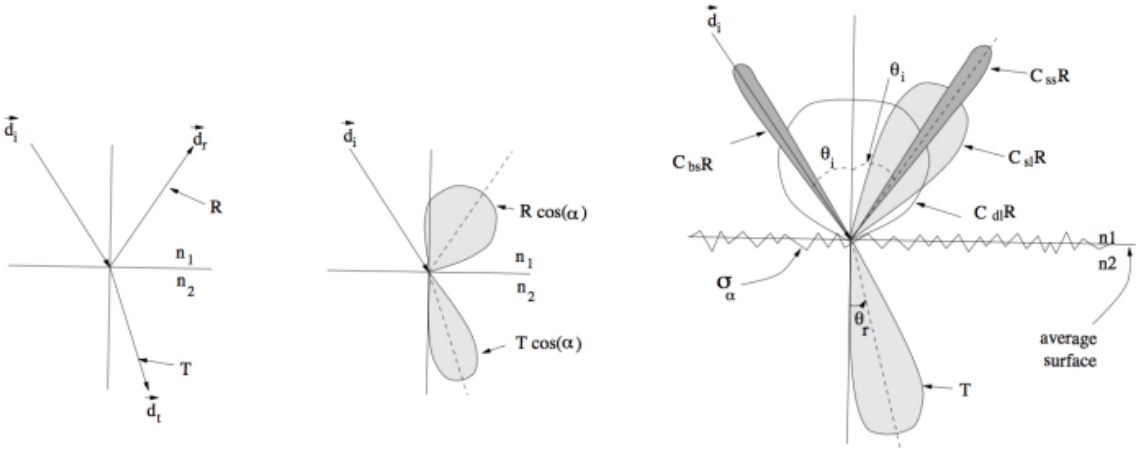

Figure 2.24: UNIFIED Model of scintillator surfaces. Left: Polar plot of the radiant intensity of the polished (left) and ground (right) models. Right: Polar plot of the radiant intensity in the UNIFIED model.

In the polished model, Fresnel reflection and refraction is assumed, where as the ground model allows for Lambertian reflection, Fresnel refraction, backscattering, as well as spike and lobe reflections. The spike (C_{ss}) reflection parameter assumes the optical photons are reflected as if the surface was a perfect mirror. The backscattering (C_{bs}) reflection parameter assumes the photon is reflected in the same direction of incidence. The Lambertian (C_{dl}) reflection parameter assumes that the photons are reflected corresponding to a Lambertian distribution. The lobe (C_{sl}) reflection parameter assumes that the photons will reflect based on the orientation of the micro-facet on the scintillator surface, where σ_α defined the standard deviation of the distribution of the micro-facets orientation [24]. One caveat of the aforementioned models is that they assume identical parameters for the entire optical surface [22].

As was done in section 2.3.1 10,000 optical photons were generated in the scintillator medium every 2.5 cm and the number of hits in the SiPM were recorded. The results of these simulations are show in Fig. 2.25. It is clear the transmission efficiency increases assuming a polished surface and so does the overall light collected

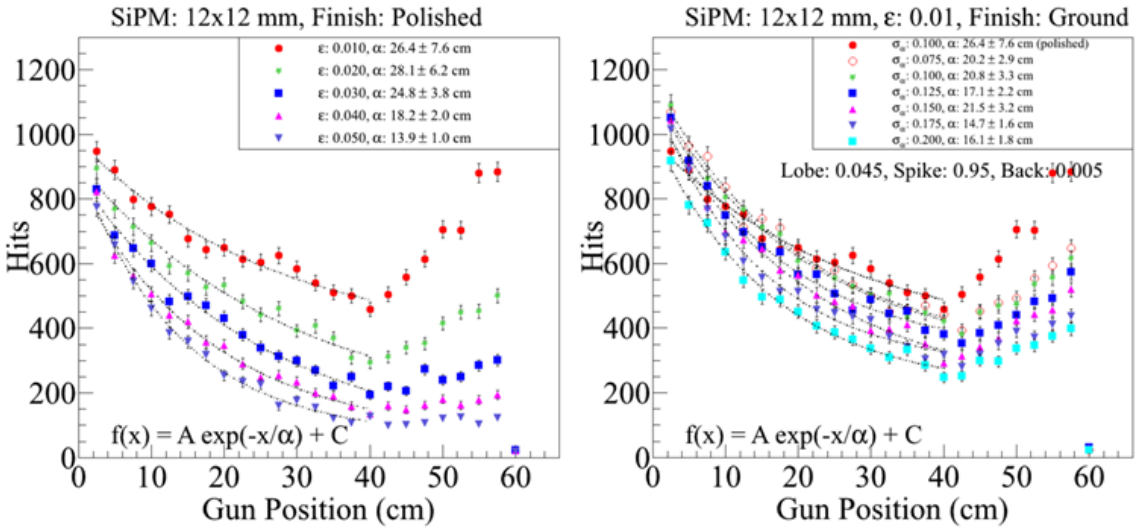

Figure 2.25: UNIFIED Model results. Left: polished model while varying the transmission efficiency. Right: ground model with varying σ_α which characterizes the standard deviation of the surfaces micro-facet orientation.

in the SiPM as seen in Fig. 2.25. Similarly, as the number of possible micro-facet orientations increases, meaning a more coarsely ground surface, the light input decreases as expected. Moreover, in the instances where the surface quality of the machined scintillators are good, the phenomenon of light increase in the nose region as the source moves further from the readout detector is clearly observed.

It is clear, in both simulation and experiment, that the unique geometry of the ST scintillator paddles causes the straight region and the nose region to have drastically different light output properties.

2.4 Misalignment Studies

To protect both the active area of the SiPMs and the scintillator surface at the upstream end of the straight section, the coupling distance between the two was required to be larger than zero. Similarly, the scintillator paddles were also shimmed radially such that the top edge of the scintillator was level with the top edge of

the active area of the SiPM thereby maximizing light collection. It was therefore necessary to study the effects of SiPM/scintillator misalignments on light collection and time resolution.

A CAD drawing of the custom test stand, seen in Fig. 2.26, illustrates all the components of the custom test stand used in the misalignment studies. The SiPM

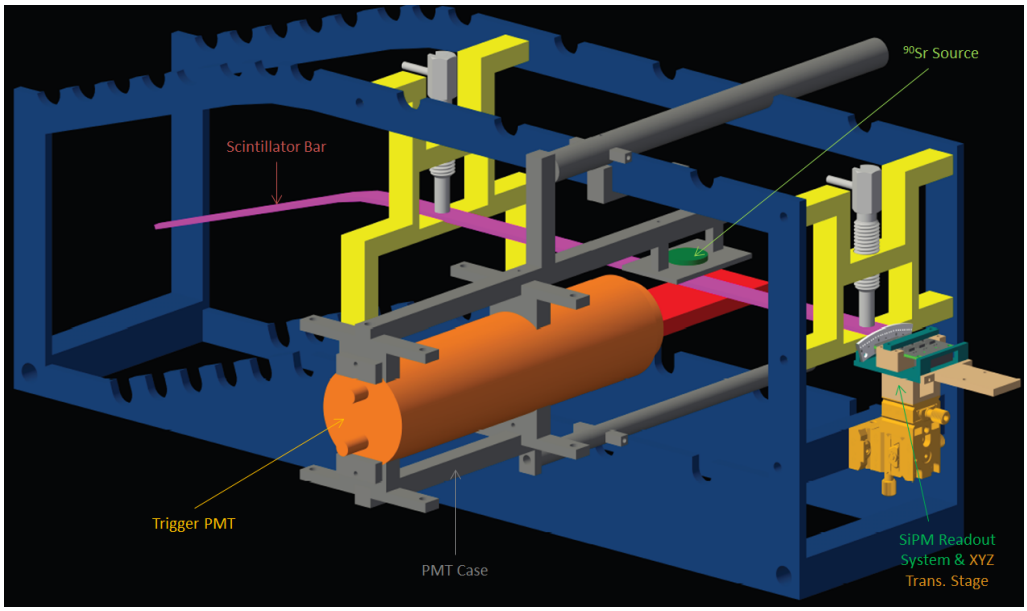

Figure 2.26: CAD Drawing of custom test stand. The test stand was used in the misalignment studies.

sits atop a Newport MT-XYZ (MT) compact dovetail XYZ linear translation stage with three fine adjustment screws with 80 threads per inch as seen in Fig. 2.27. Each translation knob for the three axes of translation provides a translation of 318 μm per rotation. It is useful to note that for each location of the SiPM, relative to the scintillator, the source and trigger PMT were located at $z = 24.467$ cm and 10,000 event triggers were collected.

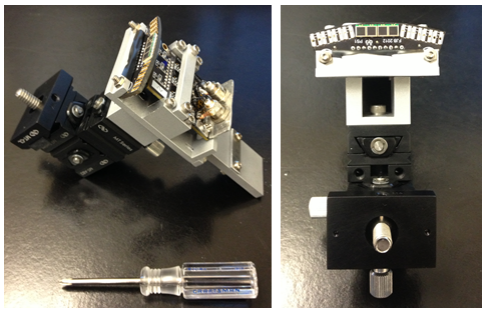

Figure 2.27: The SiPM case is the aluminum matt finished metal. The translation stage is black. Left: isometric view of SiPM case and MT-XYZ translation stage. Right: front view (looking upstream).

2.4.1 Vertical Alignment of SiPM & Scintillator

To study the effects of the various horizontal (translations along the $z - axis$) coupling distances, the relative position of the active area of the SiPM and the top edge of the scintillator paddle was required to be known. Vertical alignment is the most critical since the 3 mm thickness of the scintillator matches the 3 mm height of the active area of the SiPM. To test the 50 machined scintillators in a reproducible manner, the vertical alignment of the SiPM and scintillator must be replicated in a robust manner.

Utilizing an Edmund Optics CMOS camera, and a ruler (seen in Fig. 2.28) the vertical alignment of the top edges of the SiPM and scintillators could be measured within 0.025 mm accuracy relative to the ST2 PCB Board. The 3×3 mm^2 SiPMs, which are mounted to the ST1, are housed in a ceramic case mounted on the ST1 PCB. Therefore, there exists some area between the top of the SiPM ceramic case and the active area of the SiPM which must be taken into account. The distance is also measured both optically and manually relative to the ST2 PCB.

Figure 2.29 illustrates a labelled schematic similar to what was seen in Fig. 2.28 and depicts the variables measured and monitored so as to quantify the vertical alignment. Of all the variables in Fig. 2.29, y is of the utmost importance since it

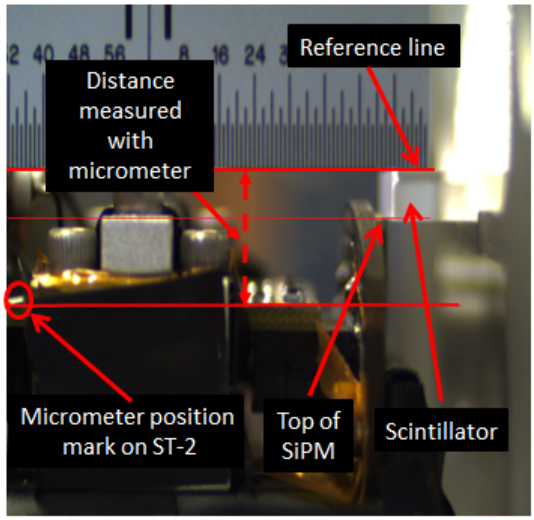

Figure 2.28: Vertical alignment optics set-up. The reference line corresponds to the top surface of the scintillator, while the micrometer position on the ST2 is clearly marked so that the absolute difference could be measured both optically and manually with a micrometer.

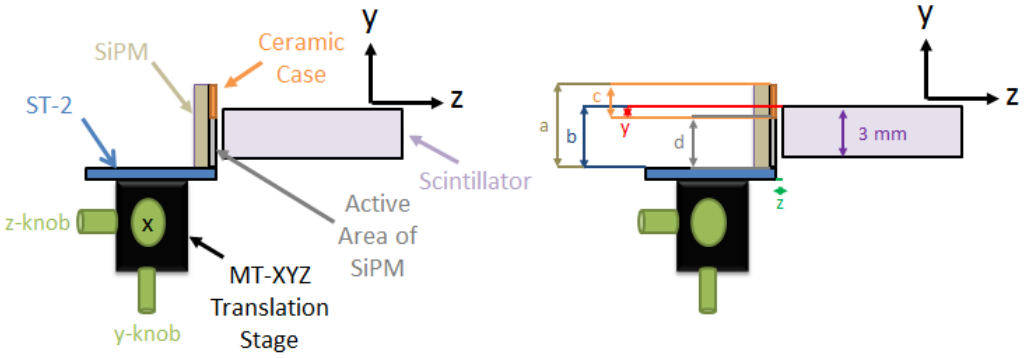

Figure 2.29: Vertical alignment optics schematic. Left: labelled cartoon of SiPM & scintillator vertical alignment. Right: variables used to quantify vertical alignment. The scintillator is intentionally misaligned in this cartoon so that the misalignment parameter y is visible.

is the distance between the top edge of the scintillator paddle and the active area of the SiPM and is the quantization of the vertical misalignment. That is to say the at $y = 0$ the SiPM and scintillator are aligned vertically. Both the distance between the top of the SiPM and ST2 PCB (a), and the distance between the top of the SiPM and the active area of the SiPM (c), are measured optically and define

the distance between the top edge of the active area of the SiPM and the ST2 PCB (d) *via* $d = a - c$, which are all constants. It is necessary to note that the coupling distance between the active area of the SiPM and scintillator (z) was done by eye and then measured optically until a desirable coupling distance was found. The values of the aforementioned variables are summarized in Table 2.4. The variable b

Variable	**Value (mm)**
a	5.22
c	0.91
d	4.32
z	0.25

Table 2.4: Vertical alignment variables. All variables were measured five times and the numbers reported are averages of those values.

defines the distance between the top edge of the scintillator and the ST2 PCB and is measured both optically and manually. This distance, coupled with the constant d, provides the measured quantity y through the difference $y = b - d$.

The coordinate system used to quantify the vertical misalignment studies is illustrated in Fig. 2.30. The scintillator remained fixed, while the SiPM was lowered, relative to the scintillator, to the minimum location governed by the range of the MT translation stage at approximately $y = -4$ mm. Coarse measurements were then taken at half turns (159 μm) intervals until the maximum height of the MT translation stage was reached which was approximately $y = +4$ mm. The results of these measurements can be seen in Fig. 2.31. Once the coarse measurements concluded, the SiPM was lowered to $y \approx -1$ mm and then the translation stage was moved in quarter turn (79.5 μm) intervals until $y \approx +1$ mm was reached. The results of both the coarse and fine measurements are seen in Fig. 2.32. It is useful to note that at every location of the SiPM the distance traversed was verified by a manual measurement made with a micrometer (1 *mil* precision).

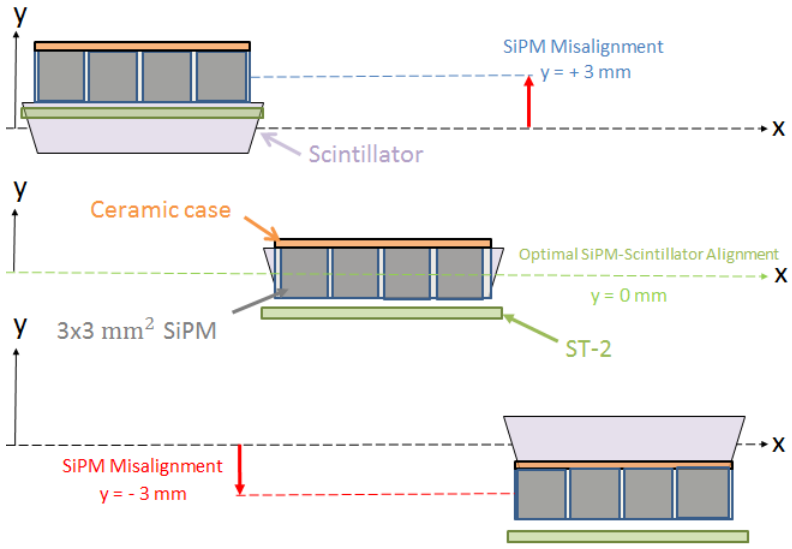

Figure 2.30: Vertical alignment schematic. The scintillator is fixed while the SiPM effectively scans across the face of the scintillator along the y-axis.

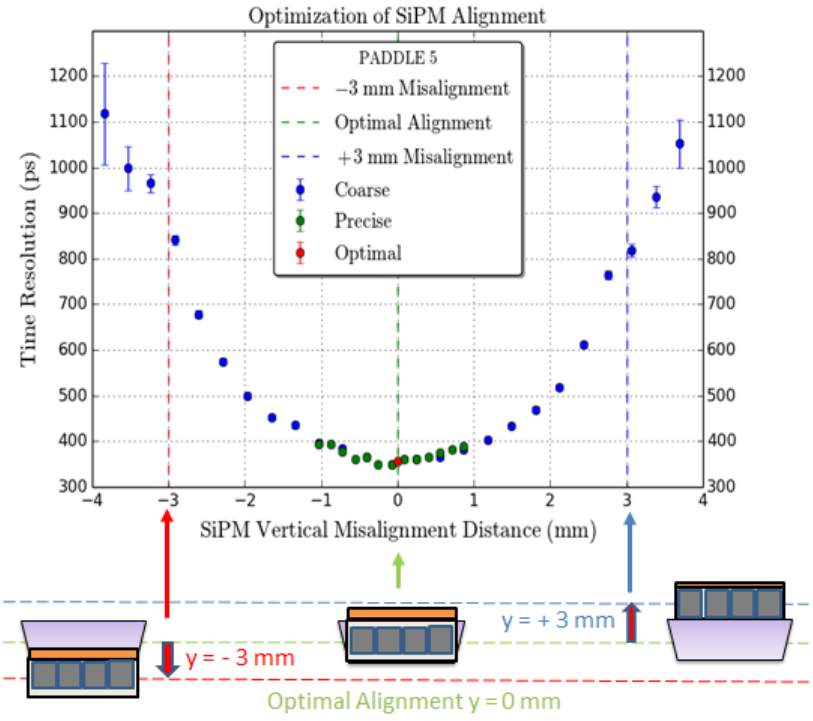

Figure 2.31: Coarse vertical misalignment results. The minimum time resolution obtained was approximately 350 ps which was expected. Once the SiPM exceeded $y = \pm 3\ mm$ there is no active area of the SiPM coupled to the face of the scintillator.

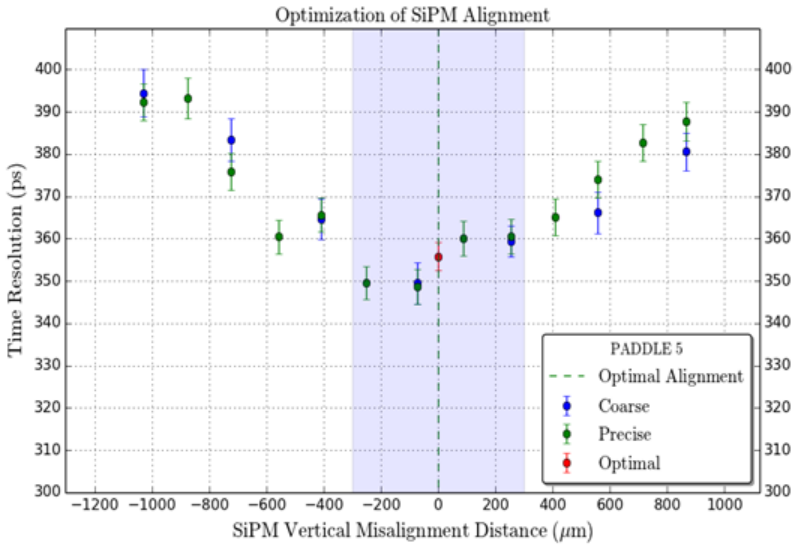

Figure 2.32: Fine vertical misalignment results. Note that the coarse and fine measurements were overlapped so the reproducibility of the measurements were depicted.

From the vertical misalignment studies it is clear that there is no significant variation of time resolution within a ± 300 μm range of the ideal alignment. These results were also simulated in a manner similar to what was discussed in section 2.3.2 and the results are seen in Fig. 2.33. The Geant4 simulations indicate that

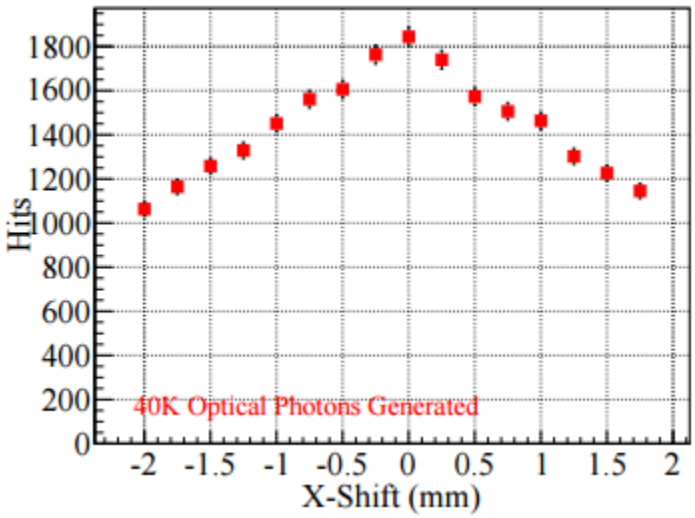

Figure 2.33: Vertical alignment simulation studies [25]. It is important to note the x-axis corresponds to the y-axis as discussed with the experimental measurements.

the acceptable range of vertical misalignment is approximately ±250 μm [25] which is consistent with what was measured on the bench at FIU.

2.4.2 Coupling Distance of SiPM & Scintillator

With the vertical alignment between the scintillator and SiPM optimized, the effects of varying the coupling distance was studied. Using an identical set-up as was described in section 2.4.1 the coupling distance, and resulting time resolutions, was measured at various locations with three distances shown in Fig. 2.34. While the

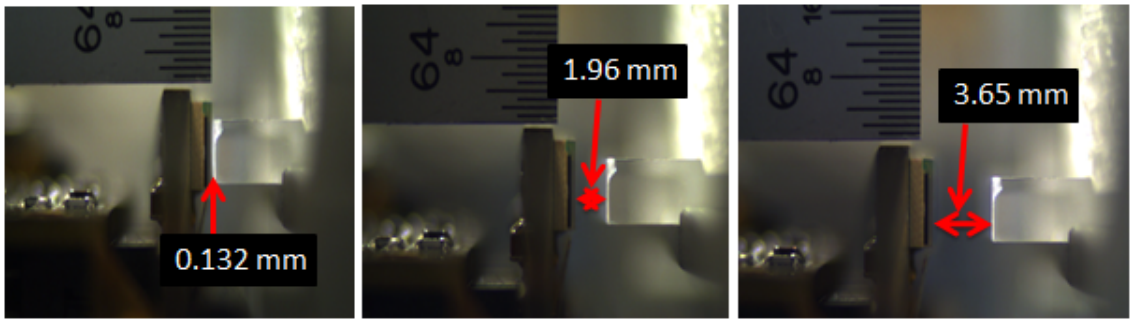

Figure 2.34: Coupling distance optics. Various coupling distances as measured with the CMOS camera. The high degree of precision is clearly visible.

coupling distance was varied, the vertical alignment was kept constant at the optimal location determined from the studies outlined in section 2.4.1 and was monitored both optically and manually.

With the optimal vertical alignment having been verified, the SiPM was moved *via* the MT translation stage along the $z - axis$ such that the active area of the SiPM was flush against the face of the machined scintillator paddle at $z = 0$ mm. In the coupling region $z < 1$ mm the SiPM was receded from the face of the SiPM in 1/4 turn (79.5 μm) intervals. For 1 mm $<$ z $<$ 2 mm, the SiPM was receded from the face of the SiPM in 1/2 turn (159 μm) intervals, and for 2 mm $<$ z $<$ 4 mm data were collected in 1 turn (318 μm) intervals and is illustrated in Fig. 2.35.

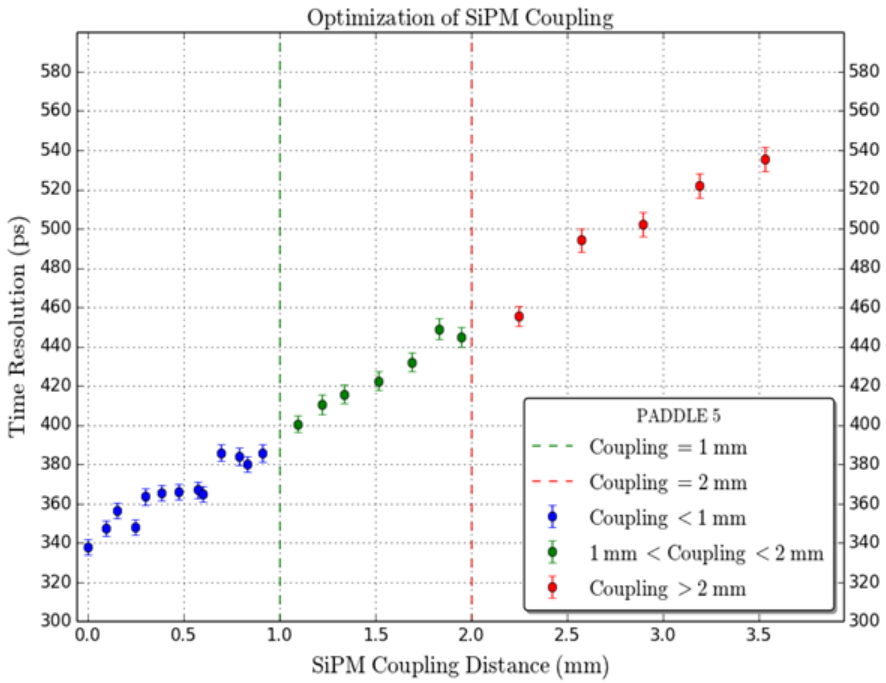

Figure 2.35: Coarse coupling distance studies. It is useful to note that at a coupling distance of 251 μm the time resolution was identical to what was measured in Fig. 2.32 while conducting the vertical alignment studies.

Figure 2.36 zooms in on the (z < 1 mm) region of the coupling distance studies shown in Fig. 2.35. It is clear from the data the optimal coupling range was 50 μm < z < 350 μm and there was no significant reduction in time resolution performance over a 0 μm < z < 600 μm range. Similarly, the simulation results also indicate that there is no significant reduction in light collection in the 0 μm < z < 600 μm range [25].

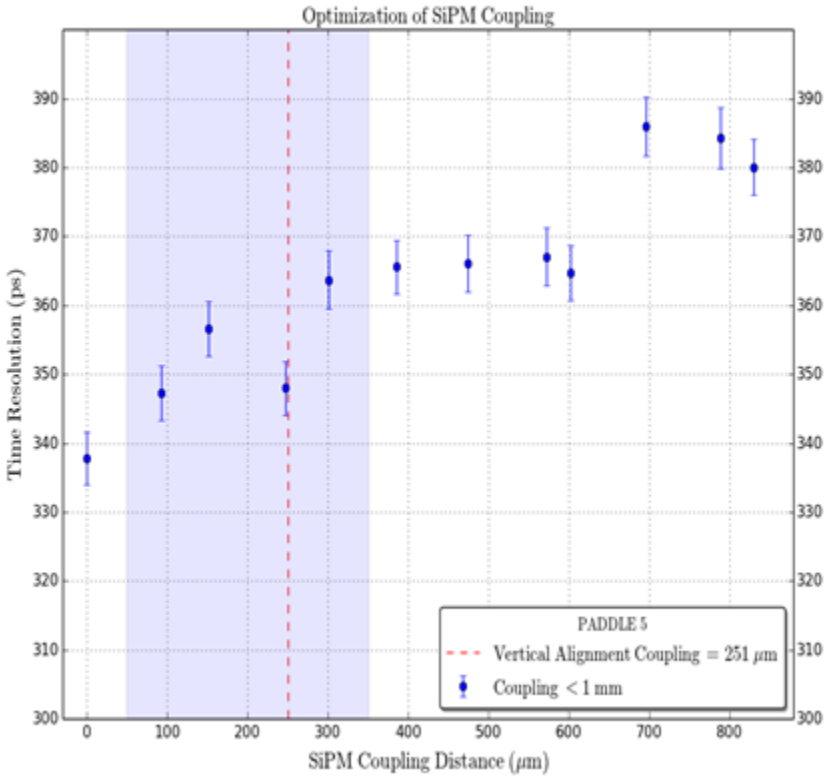

Figure 2.36: Fine coupling distance studies. The blue shaded region (50 $\mu m < z <$ 350 μm) indicates the optimal coupling range.

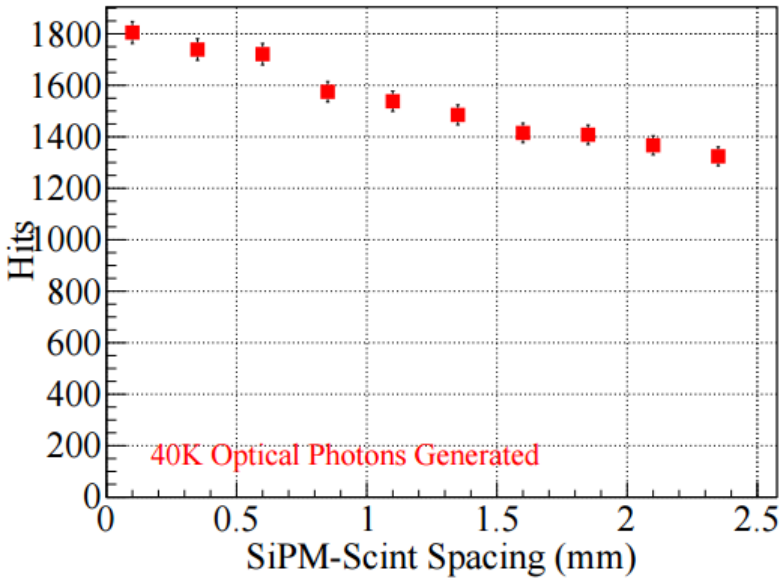

Figure 2.37: Coupling distance simulations. Simulations indicated that the optimal coupling distance is in the 50 $\mu m < z <$ 350 μm range.

CHAPTER 3

Start Counter Construction

3.1 Polishing Machined Scintillators

Prior to polishing 50 machined scintillators, received from McNeal Enterprises [17], a coarse measurement of the paddles performance was conducted to understand the magnitude of damage the paddles had incurred as a result of mishandling during edge polishing. The time resolution was measured at three precise locations along the length of the scintillators utilizing a custom fabricated test stand discussed in section 2.4.1. The upstream end of the scintillator where the light is readout out by the SiPM is defined to be $z = 0.0$ cm. One measurement is taken in the middle of the straight section at $z = 24.47$ cm, one in the middle of the bend at $z = 42.190$ cm and one at in the tip of the nose at $z = 59.02$ cm.

In doing so, we were able to quickly determine the properties of the three sections of the paddles which we then used to predict the behavior of the remaining untested scintillator areas. Thus, we were able to determine which scintillators, at their current state, were defective and were essentially unusable for the final construction of the start counter. These scintillators were then utilized so that the optimal polishing procedures could be developed.

Figure 3.1 illustrates the erratic fluctuation in time resolution performance that existed from paddle to paddle prior to polishing the scintillators. On average, even at the tip of the nose, the 50 paddles did not meet the design resolution of 350 ps.

Once the appropriate polishing procedures had been developed and implemented the surface quality was greatly improved as can be seen in Fig. 3.2. The same scintillator paddle is shown in Fig. 3.2 before and after polishing. Instead of shinning a diffuse laser into the upstream end of the straight section, the laser beam was shone

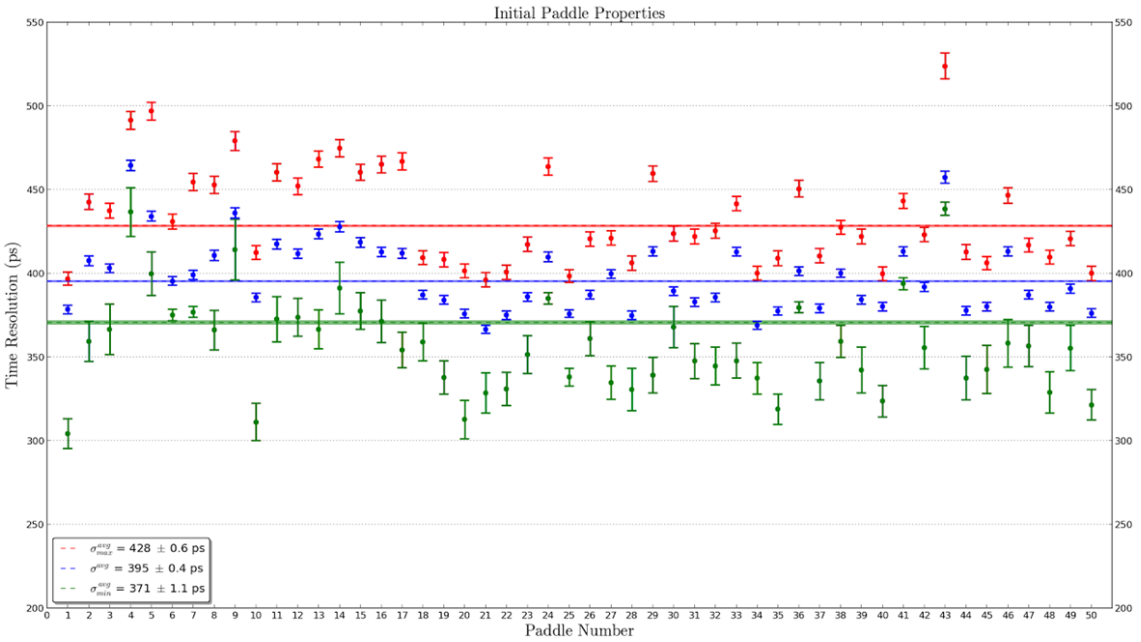

Figure 3.1: Coarse time resolution measurements prior to polishing. Paddle number is on the x-axis and time resolution in ns on the y-axis. The scintillators were tested on the custom test stand and were not wrapped in aluminum foil. The red points correspond to the time resolution in the bend region, the blue points are the average of the three measurements, while the green points occur at the tip of the nose. The red, blue, and green horizontal lines are the weighted averages of the three measurements for all 50 paddles.

into the scintillator medium from the upstream end aimed at one edge so that the total internal reflection towards the tip of the nose was visible. The unpolished scintillator had such poor surface quality that the reflections in the bend region could not be seen due to multiple scattering of light at the scintillator boundaries. However, the reflections in the polished scintillator can clearly be seen traversing down through the nose region.

After the scintillators were polished they were required to have their performance remeasured, in an identical manner outlined above and illustrated in figure, 3.1, so that an initial understanding of the effects of polishing could be understood. As expected, the time resolutions were greatly improved as seen in Fig. 3.3. On average,

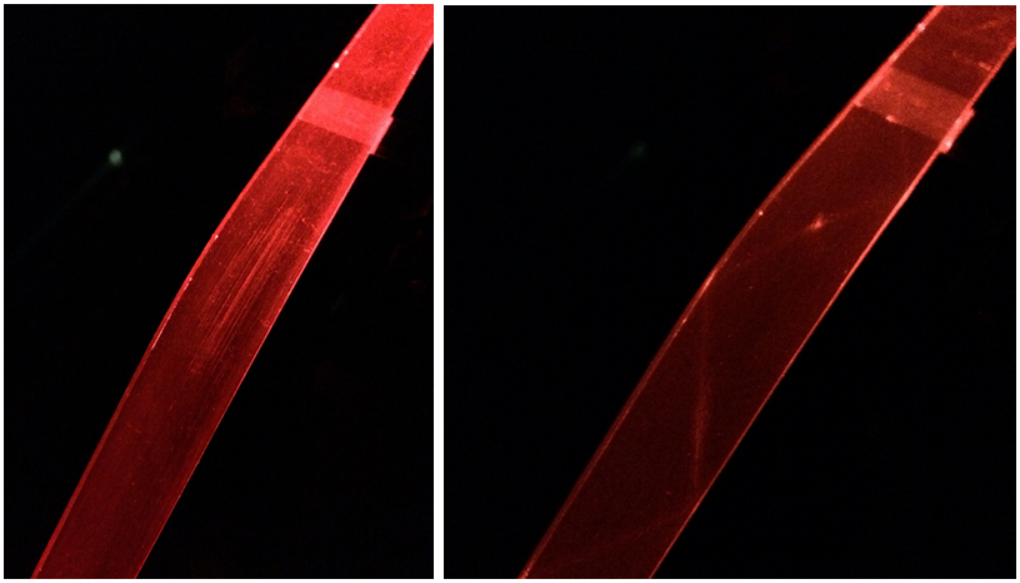

Figure 3.2: Effects of polishing scintillators. Left: non-diffuse laser incident on an edge, before polishing, at the upstream end of the straight section. Right: non-diffuse laser incident on the same edge, after polishing, at the upstream end of the straight section.

at the tip of the nose, the 50 scintillators improved in time resolution by approximately 15%. Furthermore, there was a substantial reduction in erratic fluctuations in time resolution that was exhibited across the whole lot of 50 scintillators prior to polishing.

From these measurements, careful consideration was given to the data so as to determine the best 30 scintillators that would comprise the GlueX Start Counter.

3.2 Testing of Machined Scintillators

Each of the 50 machined scintillators were tested to study light output and time resolution. They were measured in an identical manner utilizing a custom fabricated test stand shown in Fig. 2.26. The test stand allows each scintillator paddle to be measured in an identical and reproducible fashion. There exist 12 precise locations

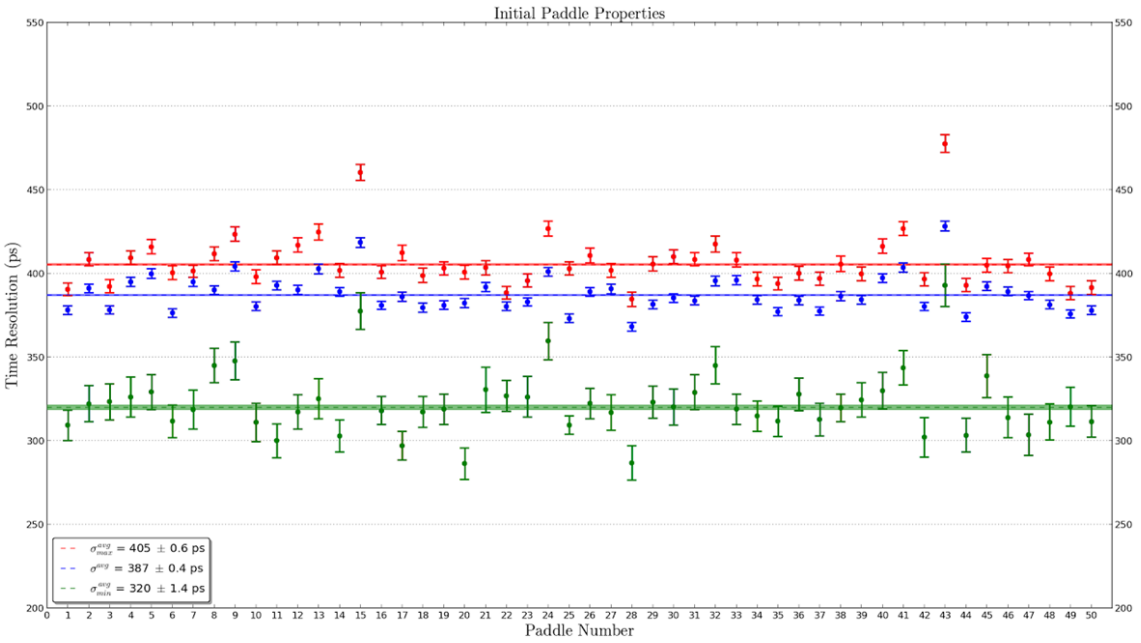

Figure 3.3: Coarse time resolution measurements after polishing. Paddle number is on the x-axis and time resolution in ns on the y-axis. The scintillators were tested on the custom test stand and were not wrapped in aluminum foil. The red points correspond to the time resolution in the bend region, the blue points are the average of the three measurements, while the green points occur at the tip of the nose. The red, blue, and green horizontal lines are the weighted averages of the three measurements for all 50 paddles.

in which a ^{90}Sr source and trigger PMT can be placed so that each of the 50 scintillators are tested at the same locations. More specifically 4 locations in the straight section, 3 in the bend, and 5 in the nose were tested.

3.2.1 NIM Electronics

When testing machined scintillator paddles, the signal processing outlined in the electronics diagram seen in Fig. 3.4 was utilized so that the desired light output and time resolution measurements could be made.

All discriminator thresholds, associated delays, and gate widths were set to the values indicated in tables 3.1 & 3.2. It is useful to note that the leading edge

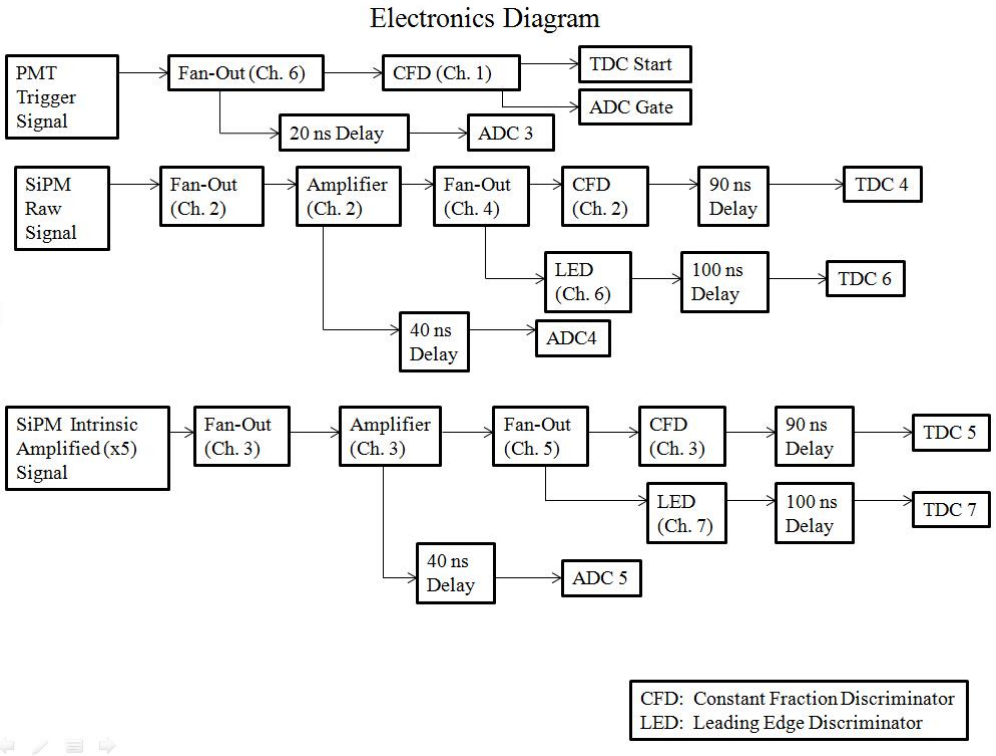

Figure 3.4: Electronics diagram for testing scintillator.

discriminators (LED) were implemented for the purpose of time-walk correction studies. All DC offsets, controlled by the linear fan out modules, were set to the

CFD Channel	Threshold (mV)	Delay (ns)	Gate Width (ns)
1	-100	5	56.0
2	-100	8	40.8
3	-145	8	40.8

Table 3.1: CFD settings

LED Channel	Threshold (mV)	Gate Width (ns)
6	-100	36.4
7	-145	40.8

Table 3.2: LED settings

values indicated in Table 3.4. Similarly, all amplification factors associated with the SiPM were set to the values indicated in Table 3.3.

SiPM Signal	Amplification Factor
Raw signal	7.05
Intrinsically amplified signal (×5)	2.54

Table 3.3: SiPM signal amplification factors.

Channel	DC Offset (mV)
2	-1.8
3	-6.2
4	-30.5
5	-12.0
6	-3.2

Table 3.4: DC Offsets. These offsets correspond to linear fan out modules.

3.2.2 Testing a Machined Scintillator Paddle

Utilizing a dedicated data acquisition computer configured with CEBAF online data acquisition CODA software, 10,000 event triggers and associated data were collected at each of the 12 locations along the scintillator path. Subsequently, ADC and TDC data for the machined scintillators were analyzed in detail as outlined in section 4.4.2.

Once the best 30 scintillator paddles were selected, they were wrapped in Al foil and then tested at all 12 locations on the test stand.

The measured time resolutions for the 30 best scintillators, which would eventually comprise the ST, were found to be satisfactory and even below design resolution in the nose region which is illustrated in Fig. 3.5.

The unique geometry of the machined scintillator paddles exhibit the phenomenon of an increase in light collection in the nose region as the light source moves towards the tip at the downstream end. It is hypothesized that the relatively poor time resolution in the straight section is due to a reflective smearing effect in which light is able to traverse from the straight section down to the tip of the nose, and then back up to the upstream end.

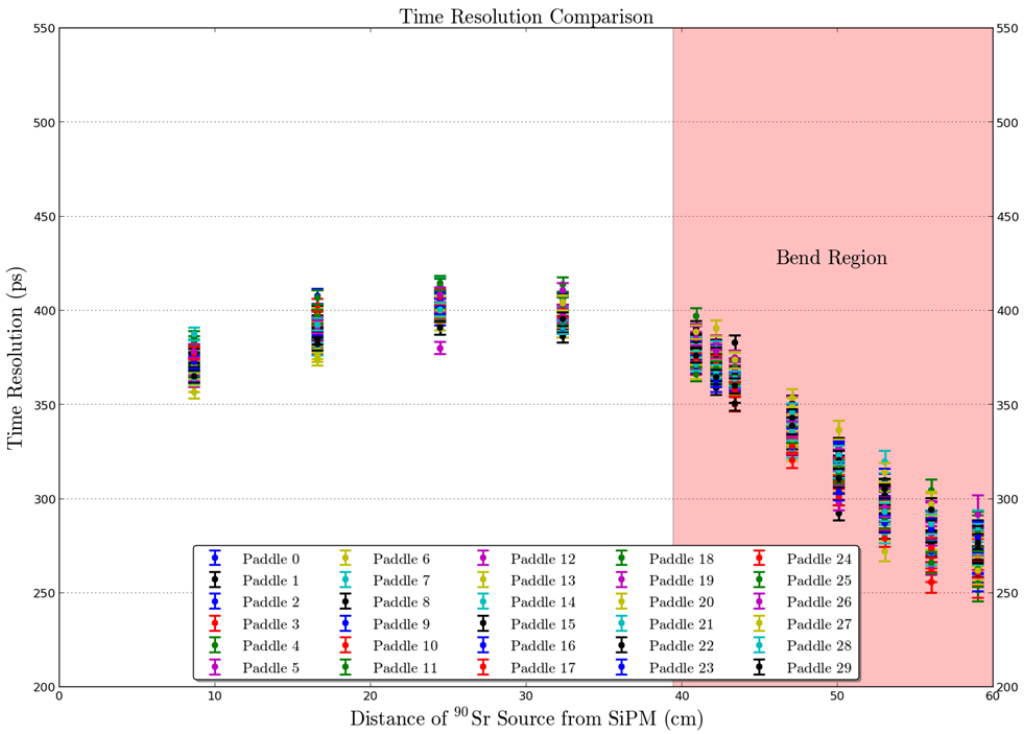

Figure 3.5: Time resolution of 30 the best scintillator paddles. The performance of the lot of scintillators is remarkably similar and only show a spread of ≈ 50 *ps* in the nose region.

The overall time resolution of the individual scintillators are shown in Fig. 3.6.

3.3 Assembly of the Start Counter

A custom fabricated support structure (assembly jig) was constructed to provide aid in the assembly of the Start Counter and is seen in Fig. 3.7.

3.3.1 Assembly Jig Components

The assembly jig consisted of a rotating cylindrical mounting bracket rigidly attached to a 2" diameter shaft housed in two cast iron mounted steel ball bearings. The rotating bracket was engineered such that it was free to rotate unless engaged

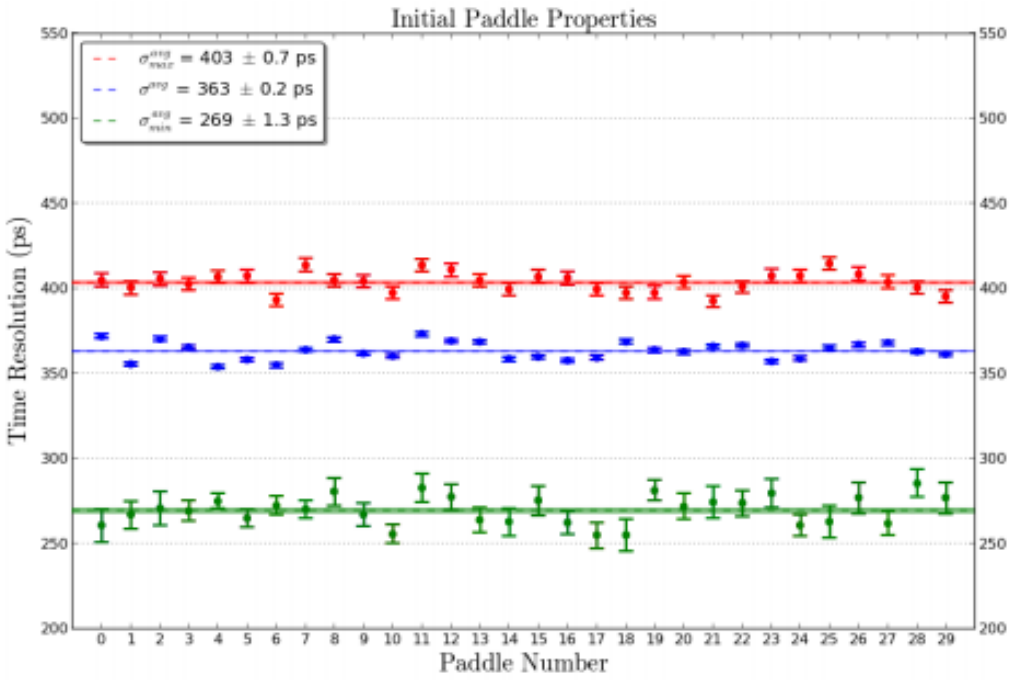

Figure 3.6: Average time resolution of 30 best scintillator paddles. The red data points correspond to the maximum time resolution obtained in all 12 data points. The blue data points are the weighted average of all 12 data points. The green data points indicate the minimum time resolution obtained in all 12 data points.

by a spring loaded locking plunger which would cause the assembly jig to move in discretized 12° intervals. Furthermore each 12° interval corresponded a paddle being oriented perfectly parallel to the table so that alignment and coupling could be performed reliably and reproducibly.

The Rohacell support was manufactured by a vendor approved by JLab while the upstream chassis was fabricated, and rigidly attached to the Rohacell support structure by Jlab technicians. They also installed the 3 layers of 650 μm thick carbon fiber to the inner surface of the Rohacell which reinforced the support structure during the assembly process. While mounted to the assembly jig, the upstream chassis (and Rohacell) was attached to the rotating bracket. A few gaps existed in the Rohacell at the glue joints, and were filled in with black RTV silicone caulking

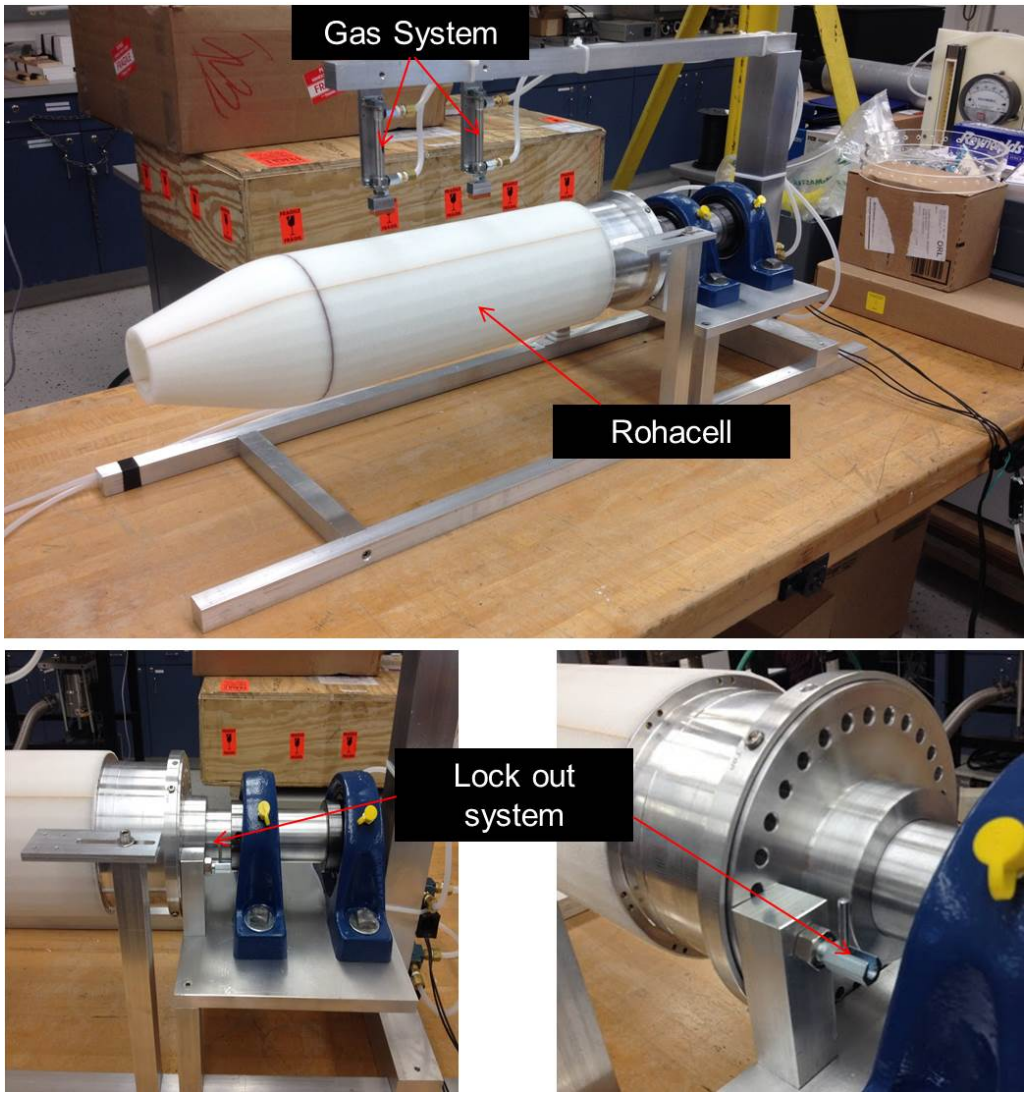

Figure 3.7: Assembly jig and lockout system. Rohacell support structure mounted on assembly jig and lockout system.

for light tightening purposes. Moreover, it was painted with black latex paint and allowed to dry overnight.

The vertical bar running parallel to the table above the Rohacell served as a mount for the pneumatic cylinders so that the scintillators could be held firmly in place during installation. Furthermore, it provided a surface in which a portable

flex arm could hold the Edmund Optics complementary metal oxide semiconductor (CMOS) camera to monitor the coupling of the scintillators and SiPMs.

A pressurized gas system was implemented to provide manual control of the two pneumatic cylinders with soft, semi-dense rubber feet attached to the ends illustrated in Fig. 3.8. The rubber feet would hold the scintillator being installed

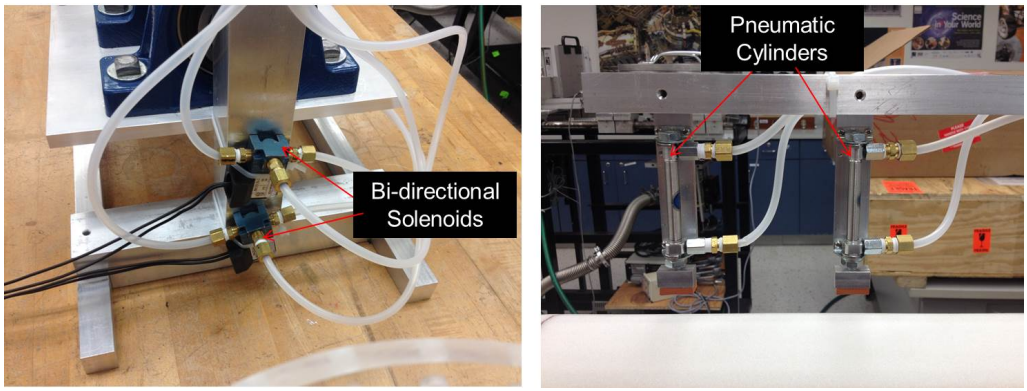

Figure 3.8: Pressurized gas system. At the end of each solenoid was a soft, semi-dense rubber foot which would hold the scintillator being installed firmly in place.

firmly in place by activating two switches which controlled each pneumatic cylinder independently *via* bi-directional solenoids connected in a 5 psi nitrogen gas system.

Two free floating acrylic rings, with 30 tapped holes 12° apart, were fabricated so as to firmly hold the 30 scintillator paddles in place during assembly. Each tapped hole housed a 10° swivel pad thumb screw which had silicone foam foot (0.25×0.25 in^2) adhered to it in order to provide a soft barrier between swivel pad and the scintillator surface. Swivel pad screws were chosen so that there existed a maximal amount of play between the scintillator and swivel pad in the event that the screw was not perfectly orthogonal to the scintillator surface.

The camera and its associated software were utilized to measure scintillator/SiPM coupling distances and shimming heights with a precision of < 10 μm in real time.

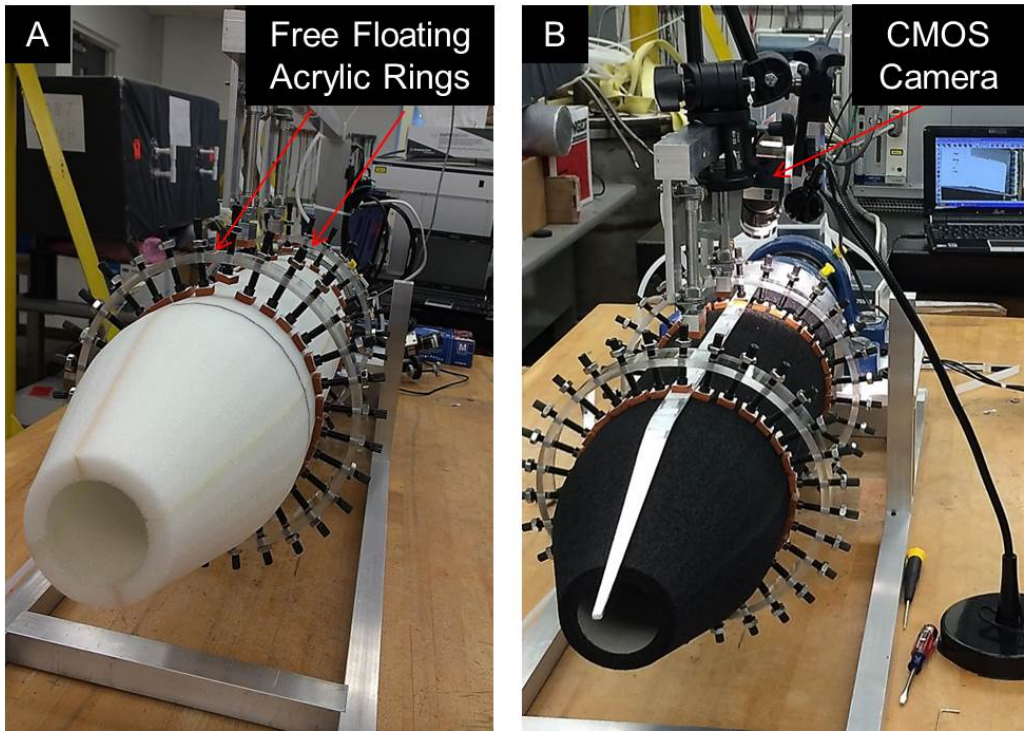

Figure 3.9: Free floating acrylic rings. Left: Rohacell prior to being painted with black latex paint. Each free floating ring is supported by 30 swivel pad screws. Right: Rohacell after being painted black. One wrapped scintillator paddled is being held firmly in place by two swivel pad screws.

The camera was calibrated such that at various magnification settings the distance to pixel ratio was known.

3.3.2 Mounting ST1 boards

The 10 ST1 boards, housing 3 sets of 4 3×3 mm^2 SiPMs were mounted to the pre-fixed tapped holes along the lip of the upstream support hub as seen in Fig. 3.10. Black 1 mm spacers were installed between the ST1 PCB and the support hub to avoid any possibility of the electrical contact between the two. After installation it was evident that the through holes in the ST1 PCB were quite a bit larger in

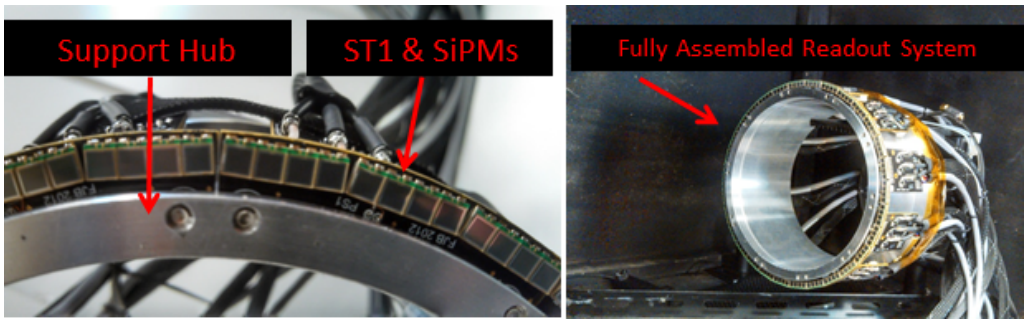

Figure 3.10: SiPMs mounted to support hub. Left: 1.5 ST1 PCBs mounted to support hub. Right: 30 ST1 PCBs (120 SiPMs) mounted to support hub

diameter relative to the screws used to connect it with the support hub. Thus, the ST1 PCB was free to move in the xy plane (hall coordinates).

A wrapped scintillator, known to not be a candidate for final installation, was then used as a reference so that the relative positions of the ST1 PCBs could be determined in a reproducible manner. The scintillator was placed at all 30 locations and coupled to each SiPM readout. This was done with all 10 ST1s fixed to the support hub. In the final configuration of the ST all 30 scintillators would be held in place by 0.8 mil thick bundling wrap. Therefore, it was required to wrap the reference scintillator to the Rohacell support structure so that it was as flush as possible to the surface as illustrated in Fig. 3.11. The position of the ST1 was adjusted such that the distance between the top edge of the scintillator and the top edge of the active area of the SiPM was offset by 30 mils (30 mil = 0.03 in = 762 μm) of radial shimming.

The offset was measured with the CMOS camera. If the alignment deviated from 30 mils, by more than 10 mils, the ST1 boards were realigned as close as possible to the nominal 30 mils by readjusting the ST1 before securing it to the support hub.

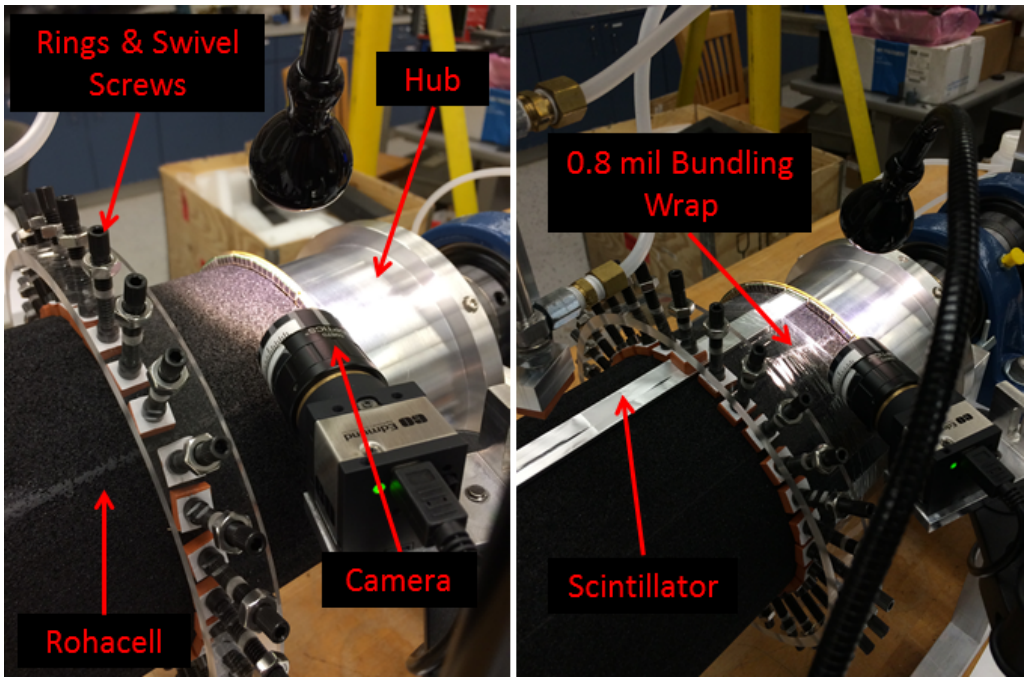

Figure 3.11: Aligning ST1 to support hub. Left: CMOS camera and lamp prepared to monitor ST1 positioning. Right: Reference scintillator wrapped to Rohacell during ST1 alignment.

3.3.3 Scintillator Paddle Installation

In order to avoid biasing the orientation of the best 30 paddles based on their performance, their locations on the ST were randomized and numbered from channel 0-29. To install a paddle the assembly jig was locked into the desired orientation *via* the spring loaded plunger. Next, the swivel screws corresponding to the channel being installed, were then raised as high as possible to provide maximum clearance between the Rohacell and the acrylic rings.

The paddle was then carefully positioned into place with upstream end of the wide straight section located a approximately a millimeter away (downstream) from the active area of the SiPM. The pneumatic cylinders were then extended so that the feet came into firm contact with the scintillator and held the paddle firmly in

place. If repositioning was required then the pneumatic cylinders were retracted, and the scintillator was adjusted to the desired orientation.

Once the scintillator was being held firmly in the optimal orientation, relative to the SiPM, the set screws were tightened and a piece of bundling wrap was wrapped firmly around the scintillator and the Rohacell structure as seen in Fig. 3.11. This was required for each scintillator paddle being installed since it was discovered that the scintillators would sometimes bow at the upstream end. This ultimately would result in false measurements while determining the distance between the top edge of the scintillator and the top edge of the active area of the SiPM. This distance was then measured with the camera to determine the amount of shimming necessary for radial alignment.

In order to determine the approximate amount of radial shimming required for each paddle, a reference paddle was used to simulate the installation of each of the 30 scintillator paddles prior to the final installation of the paddles as seen in Fig. 3.12. This was done so as to reduce the amount of handling of the good scintillator

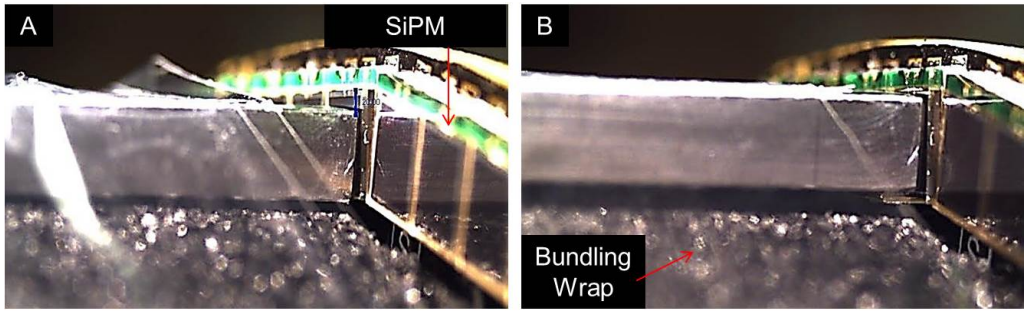

Figure 3.12: Shimming effects. Left: Before and Right: after shimming.

paddles. Three different thickness's (5, 10, 20 mil) of Kapton polyimide heavy duty film (type HN, $\rho = 1.42$ g/cm^3) were cut into 0.5×12 in^2 strips and utilized for shimming the scintillators in the radial direction. The 10 and 20 mil material were an opaque black while the 5 mil material was a semi-translucent yellow. The

shimming material was stacked in order to have the bottom and top film piece be a 10 or 20 mil piece for light tightening purposes.

Even though measurements with a reference bar were taken, the radial alignment of the scintillator with the active area of the SiPM was remeasured at the time of final installation so as to ensure the most optimal coupling. The identical process of alignment was repeated with the good bars and the final shimming required was recorded and can be seen in Table 3.5.

The Kapton strips were neatly stacked atop each other and placed along the surface of the Rohacell. They were centered along the the paddle outlines cut into the Rohacell. While ensuring the Kapton did not move, a paddle would be installed on top of the Kapton and held firm in place by the pneumatic cylinders with the upstream end of the straight section being ≈ 1 cm away from the active area of the SiPM. The final coupling took place later.

The paddle was carefully positioned that the center of the upstream paddle was aligned with the center of the SIPM. Any misalignment or offset would quickly propagate to the adjacent paddles and it would be impossible to install the remaining paddles. Once the position of the scintillator was satisfactory the swivel screws were extended to hold the scintillator in place and pneumatic cylinders were retracted and the assembly jig was rotated to the next adjacent location. This procedure was repeated until all 30 scintillator paddles were installed.

3.3.4 Coupling a Scintillator to SiPM on Assembly the Jig

Once all 30 scintillators were shimmed and installed the scintillators were coupled to the active area of their respective SiPM's. The paddle was removed from the assembly jig and the shimming material was positioned $\approx$ 1 cm away from the

ST1 Board Number	**ST1 Channel Number**	**Required Shimming (mils)**	**Amount Shimmed (mils)**	**FIU Paddle Number**
1	0	34	35	20
	1	29	30	27
	2	24	25	42
2	0	28	30	48
	1	28	30	25
	2	26	30	22
3	0	15	20	34
	1	22	25	16
	2	25	30	36
4	0	34	35	19
	1	31	30	49
	2	37	35	11
5	0	32	35	17
	1	32	35	39
	2	33	30	10
6	0	25	25	37
	1	31	30	50
	2	29	30	46
7	0	20	20	28
	1	30	30	47
	2	25	30	18
8	0	26	30	03
	1	32	30	23
	2	35	35	38
9	0	29	30	35
	1	36	35	14
	2	38	35	1
10	0	35	35	7
	1	30	30	6
	2	25	25	44

Table 3.5: Shimming material used. Amount of shimming material calculated relative to how much material was used in the final assembly. Table **??** provides a translation table to equate the FIU paddle numbers to JLab sector numbers.

active area of the SiPM. A piece of computer paper sandwiched between two pieces of Al foil (≈ 150 μm thick) was then placed parallel to the active are of the SiPM

and the paddle was then pressed firmly against the outer most piece of Al foil which is seen in Fig. 3.13.

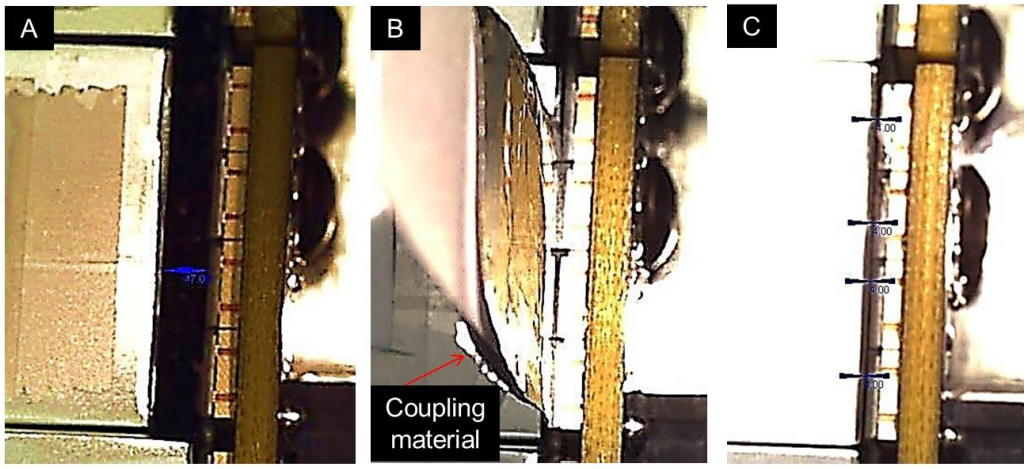

Figure 3.13: Steps of coupling paddles to SiPM. Left: Paddle prior to being coupled to SiPM. Center: Paddle pressed firmly against spacing material and SiPM. Right: Paddle properly coupled to SiPM at a distance of 162 μm.

With the upstream end of the scintillator firmly pressing against the face of the SiPM the piece of computer paper was carefully removed. Then, the Al foil pieces were removed individually so as to ensure no damage was incurred on the paddle surface or SiPM. It is useful to note that studies showed that the coupling of the SiPM/scintillator could not exceed 300 μm without a substantial amount of light loss occurring.

Once the paddle had been couple to the SiPM in a manner that was satisfactory (see Fig. 3.13), the paddle was secured *via* swivel pad screws and the the assembly jig rotated to the adjacent paddle and the process was repeated in an identical manner until all 30 paddles had been coupled to their respective paddles.

3.3.5 Securing the Start Counter Paddles to Rohacell

In order to secure paddles to the Rohacell support structure the Start Counter was wrapped along its length using self-adhesive transparent bundling wrap (0.8 mil thick, 6 in wide) at six different locations perpendicular to the central axis of rotation. Four of the locations were wrapped along the straight section at equal distance ($\approx$ 8 cm) from one another. One section was wrapped around the bend section and the nose region was wrapped in a symmetrical manner. While wrapping the straight section, the three most downstream sections were wrapped first, followed by the upstream end of the start counter. This was done to ensure that the least amount of torque would be applied to the area closest to the SiPM/paddle coupling.

For the four locations in the straight section $\approx$ 2 ft of bundling wrap was cut for each section. The bundling wrap was slid under the start counter and centered on the location to be wrapped. With equal lengths of bundling wrap on each side, the bundling wrap was placed firmly along the bottom of the start counter. One side of the wrap was firmly wrapped over the top side of the ST and held in place while the other end was wrapped over the first. At the end of the overlap area a small piece of electrical tape was placed to mark the overlap and keep a count of how many overlaps were placed at one position. This process was repeated for a total of five times at each of the four positions in the straight section. This procedure was also done for the bend region. It is useful to note that with every addition of bundling wrap, it was applied in the reverse manner to the one preceding it so as to reduce effects of torque during application and to not disturb the paddle/SiPM alignment.

In order to wrap the nose region a strip of bundling wrap centered along the bottom side, downstream edge of the nose. That is to say that the strips edge was lined up with the edge of the tip of the start counter nose. The wrap was then firmly wrapped around the nose region crossed over like a ribbon with the ends stuck onto

the wrapping along the bend region on the top side of the start counter. Another strip was quickly applied to the bend region so as to hold the tips of the ribbon in place. Then the start counter was rotated 180 degrees and the process was repeated. This was done a total of 4 times at every 90 degrees. Once all the bundling wrap had been applied the acrylic rings were no longer required to hold the paddles securely to the Rohacell support structure as illustrated in Fig. 3.14.

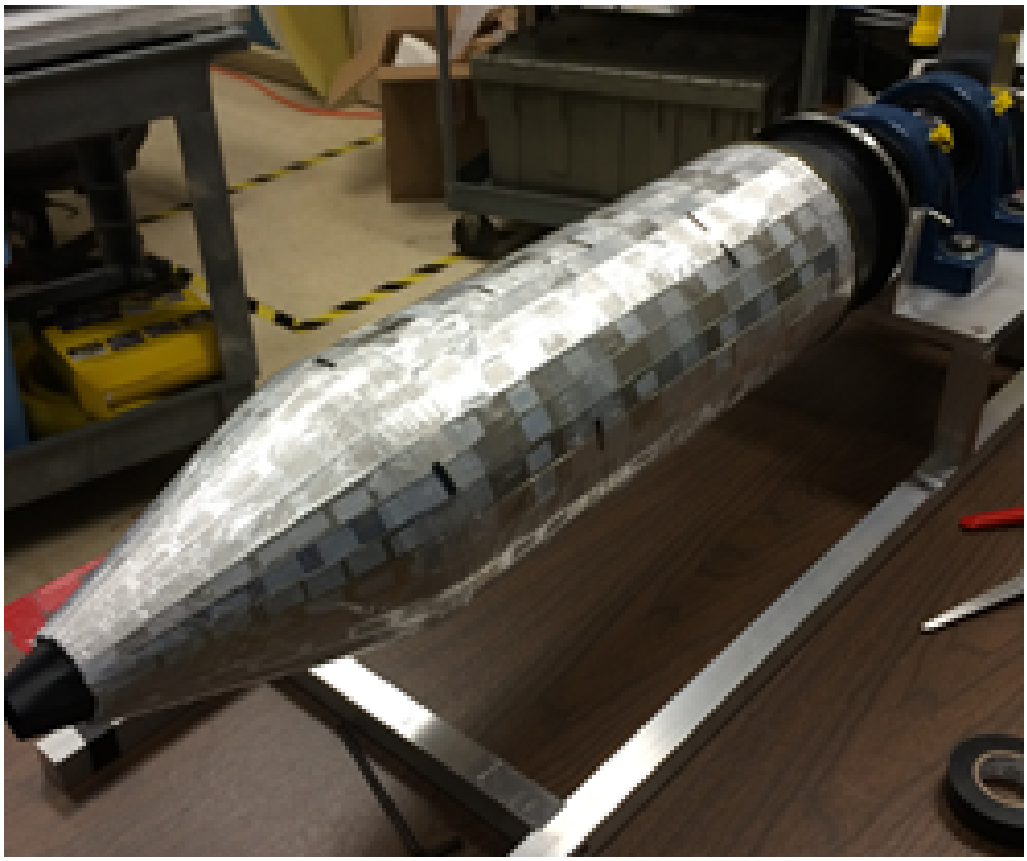

Figure 3.14: Isometric view of assembled Start Counter. The pieces are black electrical tape which mark the ends of bundling wrap are clearly visible.

3.3.6 Light Tightening of the Start Counter

After wrapping the Start Counter the free floating acrylic rings were removed. It is necessary to note that prior to installing all 30 paddles an inner cone of black

Tedlar® (polyvinyl fluoride $\rho \approx 1.5$ g/cm^3) was taped to the Rohacell for light tightening purposes as seen in Fig. 3.15.

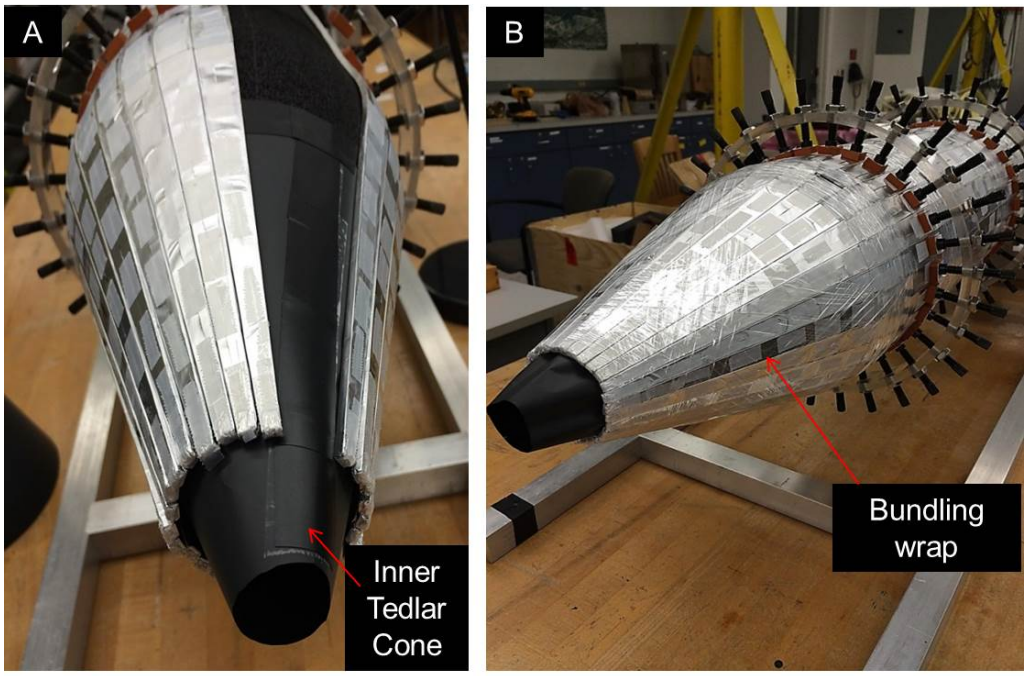

Figure 3.15: Inner Tedlar cone. Shown is before and after wrapping with bundling wrap. The cone was specifically engineered to have the same dimensions of the Rohacell support structure to avoid crumpling of the light tightening material.

The support hub was also was wrapped with Tedlar® and taped down with black electrical tape. The spacing between the ST1 PCBs along with the bottom side of the support hub, was filled with RTV black opaque silicone caulking illustrated in Fig. 3.16. Similarly, RTV silicone caulking was then applied to the inner edge of the collar which encompassed the ST1 PCBs at their our diameter as seen in Fig. 3.16.

A cone of Tedlar was wrapped around the nose region and taped down with electrical tape as seen in Fig. 3.17. The tips of the inner and outer cones in the nose region were then taped together with electrical tape and eventually trimmed

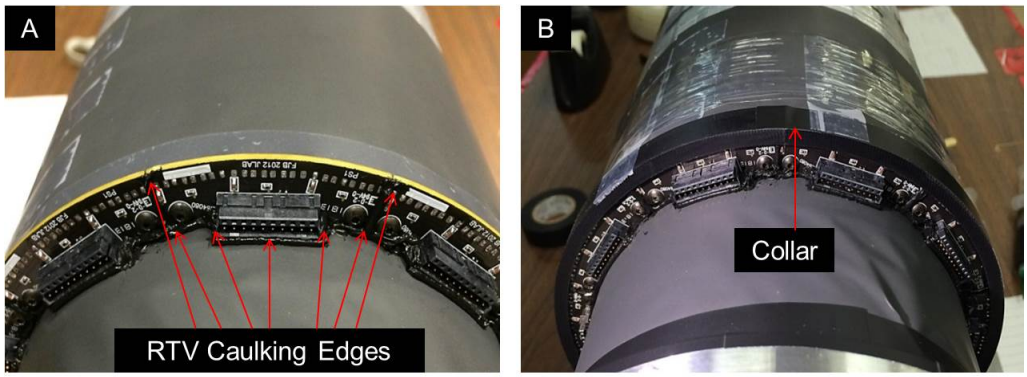

Figure 3.16: RTV caulking. Left: RTV caulking of ST1 PCBs and hub for light tightness. Right: Collar designed for light tightening purposes.

of any excess material. Furthermore, a cylindrical piece of Tedlar was taped down at the bend region and to the collar covering the ST1 boards.

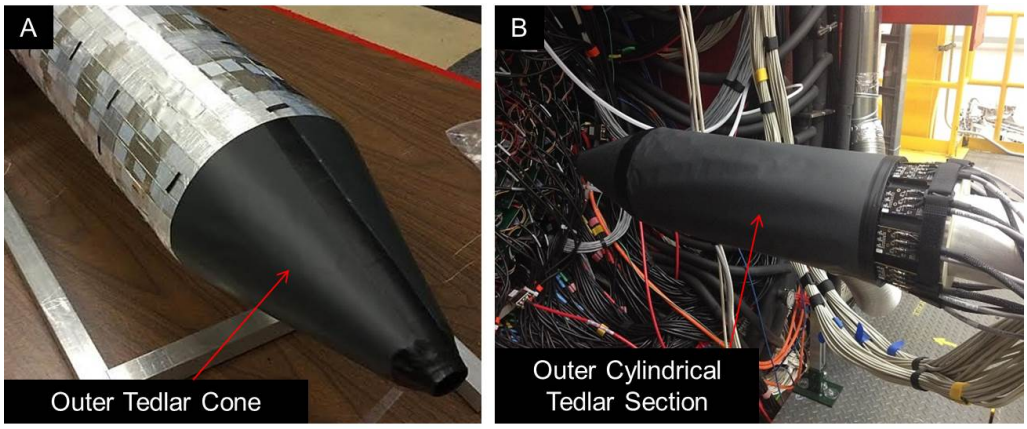

Figure 3.17: Light tight Start Counter. Left: Outer cone Tedlar® piece. Right: Fully light tight Start Counter mounted to the Fall 2015 commissioning target.

Once the ST was thought to be light tight, extensive tests were conducted so as to ensure that there were no light leaks prior to mounting to the target.

CHAPTER 4

Start Counter Calibration

4.1 GlueX 250 MHz Flash Analog to Digital Converters

Each of the 30 Start Counter (ST) analog channels are fed into the front panels of two Jefferson Lab 16 channel 250 MHz VME64x flash analog-to-digital converters (FADC250). The FADC250 readouts for the ST have been configured to the available 2 volt dynamic range setting. The FADC250s measure a predefined number of raw samples, at 4 ns intervals, of each incoming pulse corresponding to an event trigger. If at least one sample of the incoming pulse is larger than the user defined threshold, then pulse identification will be initiated [26]. There are a number of useful pulse data that can be reported by the FADC250's field programmable gate array (FPGA) for each analog pulse that crosses the programmed threshold value, depending on the operating mode in which the FADC250 was configured to run. The various data that can be reported are discussed below.

4.1.1 FADC250 Pulse Pedestal

The pulse pedestal information is reported for every pulse that falls within the trigger window. The pulse pedestal is calculated by averaging the first four raw pulse samples within the trigger window, once at least one pulse sample has crossed the threshold [26]. An example of one ST sector pulse pedestal spectrum can be seen in Fig. 4.1. This quantity provides information regarding the base line of each pulse, which is predominately determined by the user defined digital to analog converter (DAC) values in a detector specific configuration file. There is of course an overall contribution from the readout electronics to the baseline for each pulse. The

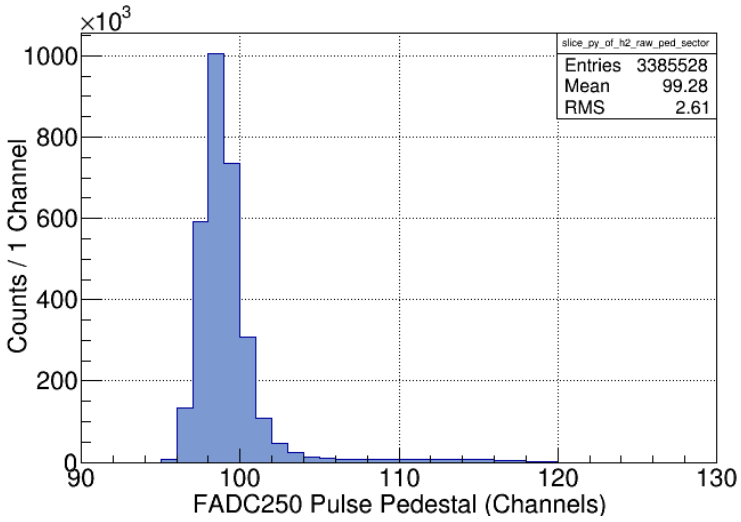

Figure 4.1: Typical Start Counter FADC250 pulse pedestal spectrum. The spectrum is from sector 15, during the Spring 2015 run 2931. In this histogram, the Gaussian distribution has a $\sigma \approx 1.1$ channels

pedestal information is crucial since the true pulse peak, and pulse integral, data need to be pedestal subtracted in order to properly interpret the absolute value being reported by the FPGA.

4.1.2 FADC250 Pulse Integral

For a given pulse that is above threshold and falls within the trigger window, the pulse integral data is reported. The pulse integral is defined to be the sum of all raw data samples within the trigger window. This data, when subtracted from the value of the pulse pedestal, is useful for energy deposition measurements, *e.g.* dE/dx. An example of a typical pedestal subtracted pulse integral spectrum can be seen in Fig. 4.2. In modes 2, 3, & 4, up to three pulses can be identified in the trigger window [26].

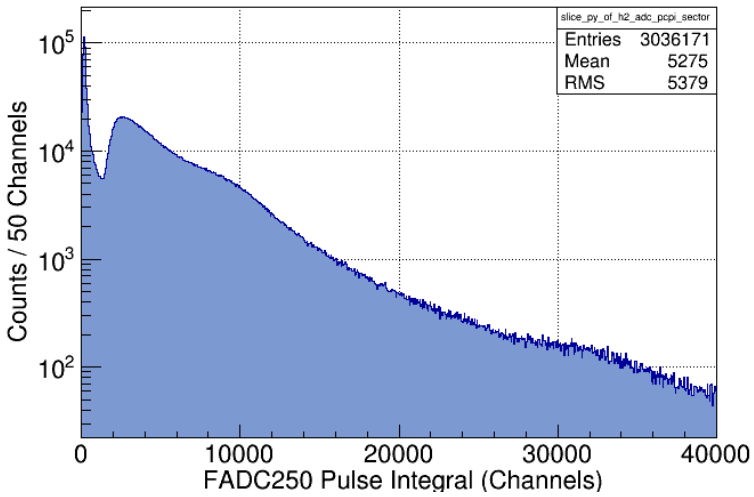

Figure 4.2: Typical Start Counter FADC250 pulse integral spectrum. The spectrum has been pedestal subtracted. This spectrum is from sector 15, during the Spring 2015 run 2931.

4.1.3 FADC250 Pulse Peak

The FPGA also provides information pertaining to the amplitude of the signal which has crossed the threshold. This quantity is also known as the "pulse peak." This particular data can only be obtained when the FADC250 is operating in modes 1, 4, 7 & 8. In order to locate the sample which is in fact the maximum sample value of the raw pulse data, the FPGA locates the first instance of a sample value which has decreased relative the sample preceding it, and reports the preceding sample value as the pulse peak. An example of a typical pulse spectrum can be seen in Fig. 4.3. This quantity is of particular importance since it provides information required to properly characterize the amplitude of each pulse. This in turn allows for a proper "time-walk" correction to be made to the data, which is discussed further in section 4.3.1.

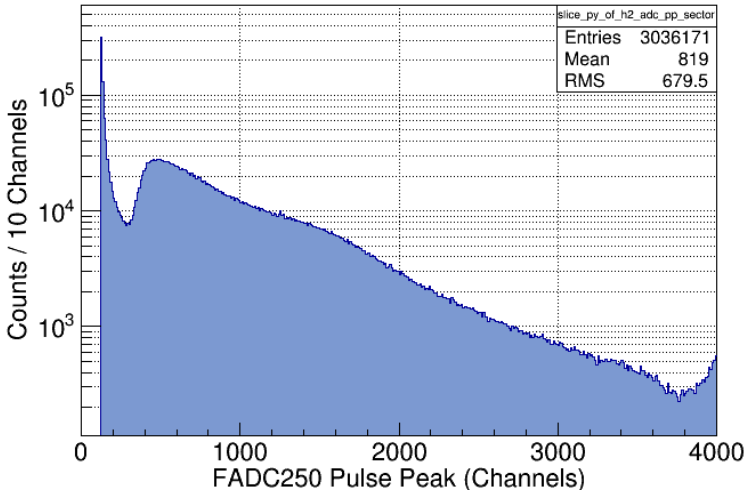

Figure 4.3: Typical Start Counter FADC250 pulse peak spectrum. The spectrum has not been pedestal subtracted. This spectrum is from sector 15, during the Spring 2015 run 2931.

4.1.4 FADC250 Pulse Time

The pulse time is a quantity of particular importance that is calculable by the FADC250's FPGA. The specific mode in which the FADC250 is set to acquire data will dictate which of the two available pulse times will be recorded. One form of pulse time that may be calculated is the "coarse" pulse time which is reported as the time corresponding to the first pulse sample which has crossed the threshold. In modes 2 & 3 the coarse pulse time is reported. The coarse time may not be used as a reference time since it contains an inherent minimum 4 ns time-walk effect. Fortunately, there exists an alternate pulse time calculable by the FADC250's FPGA. This is known as the "high resolution" pulse time. In modes 4, 7, & 8 the high resolution pulse times will be computed and reported for each pulse crossing threshold. The pulse time that is reported corresponds to the time in which the signal has reached 50% of its maximum amplitude. A representative high resolution pulse time spectrum can be seen in figures 4.4 & 4.6

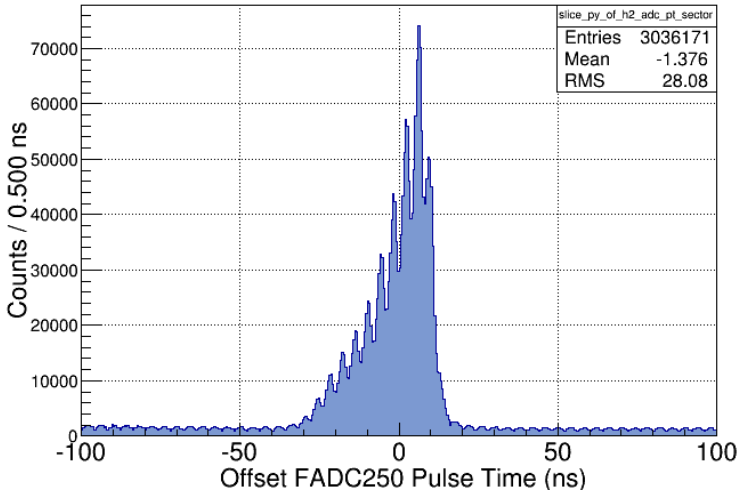

Figure 4.4: Typical Start Counter FADC250 pulse time spectrum. The spectrum has an applied offset to center the time around 0 ns. This spectrum is from sector 15, during the Spring 2015 run 2931.

The algorithm utilized by the FADC250's FPGA in order to calculate a high resolution pulse time is the following. Table 4.1 outlines the various variables needed by the FPGA to calculate a signals corresponding pulse time. A simulation of how the FADC250's FPGA handles pulse data can be seen in Fig. 4.5. The pulses pedestal, V_{ped}, is determined by averaging the signal size of the first four samples in the trigger window which is illustrated by Eq. 4.1.

$$V_{ped} = \frac{1}{4} \cdot \sum_{i=1}^{4} SN_i \tag{4.1}$$

This was discussed in more detail in section 4.1.1. The pulse peak V_{peak}, discussed in section 4.1.3, is the sample with the maximum value of the entire pulse sample data. We define V_{mid} to be the location where the signal crosses 50% of its maximum value and is calculated by Eq. 4.2.

$$V_{mid} = \frac{V_{peak} + V_{ped}}{2} \tag{4.2}$$

Variable	Description	Units
SN	Sample number	Samples (au)
V_{ped}	Signal pedestal	Volts (V)
V_{peak}	Signal Amplitude	Volts (V)
V_{mid}	50% of Signals Amplitude	Volts (V)
$V(SN-1)$	Size of sample number which occurs immediately before V_{mid} is reached	Volts (V)
$V(SN+1)$	Size of sample number which occurs immediately after V_{mid} is reached	Volts (V)
t_{mid}	Time when signal reached 50% of amplitude	Picoseconds (ps)
$t(SN-1)$	Time of sample number which occurs immediately before V_{mid} is reached	Picoseconds (ps)
$t(SN+1)$	Time of sample number which occurs immediately after V_{mid} is reached	Picoseconds (ps)
t_{fine}	High resolution time when signal reached 50% of amplitude	Samples (au)

Table 4.1: FADC250 FPGA Pulse time variables. These variables are used in the FADC250 calculation of pulse time objects determined by the FPGA.

In order to determine the time t_{mid} in which V_{mid} is reached by the pulse data, the method of linear interpolation is utilized by the FPGA which is briefly discussed below.

Once V_{mid} has been calculated the FPGA can then deduce numerically what sample numbers are, and their respective data, immediately adjacent to the point in which the pulse data has reached its half maximum. That is to say that V_{SN-1} & V_{SN+1} are known. Since these quantities are definitively known, a linear interpolation can be calculated. The two discrete points in the data that are of interest are (t_{SN-1}, V_{SN-1}) and (t_{SN+1}, V_{SN+1}) which are represented by red data points in Fig. 4.5. As previously mentioned V_{mid} has already been calculated. However, the quantity of interest is the time associated with the half maximum of the pulse data,

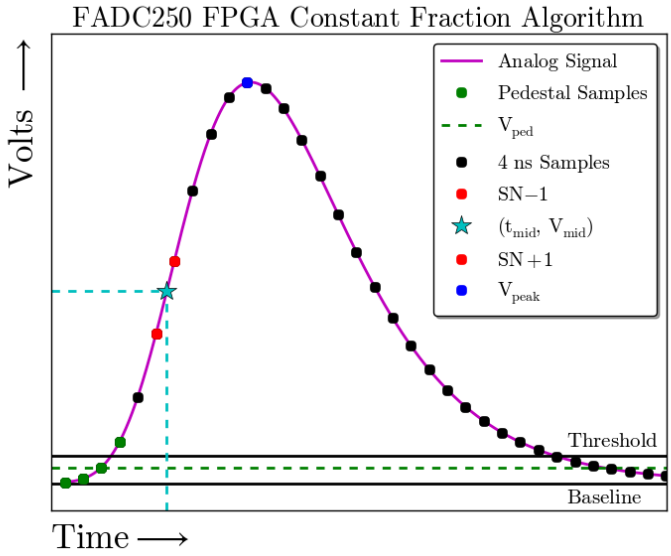

Figure 4.5: FADC250 FPGA Constant fraction algorithm. Graphical representation of the FADC250 FPGA constant fraction algorithm utilized to calculate the pulse time for pulse data. It should be noted that a signal can cross the threshold anywhere in time, albeit within the trigger window which is usually on the order of 400 ns or 100 samples.

t_{mid}. From linear interpolation we have the relationship given by Eq. 4.3.

$$\frac{V_{mid} - V(SN-1)}{t_{mid} - t(SN-1)} = \frac{V(SN+1) - V(SN-1)}{t(SN+1) - t(SN-1)} \tag{4.3}$$

Solving for the quantity $t_{mid} - t(SN-1)$ we obtain Eq. 4.4.

$$t_{mid} - t(SN-1) = t(SN+1) - t(SN-1) \cdot \frac{V_{mid} - V(SN-1)}{V(SN+1) - V(SN-1)} \tag{4.4}$$

When the FPGA is operating in high resolution timing modes there exists 64 sub-samples, each separated by 62.5 ps in time, associated with each 4 ns sample period. Therefore, it is clear that $t(SN+1) - t(SN-1) = 4$ ns $= 64$ *sub samples* and Eq. 4.4 reduces to Eq. 4.5 where we have defined $t_{fine} = t_{mid} - t(SN-1)$.

$$t_{fine} = 64 \cdot \frac{V_{mid} - V(SN-1)}{V(SN+1) - V(SN-1)} \tag{4.5}$$

When the FPGA is not running in high resolution timing modes, the time in which the first sample crosses threshold is reported. The situations in which the FPGA

fails to correctly calculate the pulse time, or any of its associated data, are discussed in further detail with reference [26]. In order to convert the high resolution pulse time (t_{fine}) to units of time a conversion factor α_i^{FADC} is required. One count corresponds to one period of the 250 MHz system clock divided by the number of sub samples for each period which is 64, *i.e.* 62.5 ps [27]. The final form of the pulse time is offset such that the spectrum is approximately centered about zero illustrated by Eq. 4.6.

$$t_i^{FADC} = \alpha_i^{FADC} \cdot T_{FADC} + O_i \tag{4.6}$$

When computing the high resolution pulse time, the sampling interval of the FADC250 causes the pulse time spectrum to be populated by a series of convoluted Gaussian distributions, with centroids separated 4 ns in time. This effect is clearly observable in Fig. 4.4. This is due to the fact that t_{fine} can technically occur at any

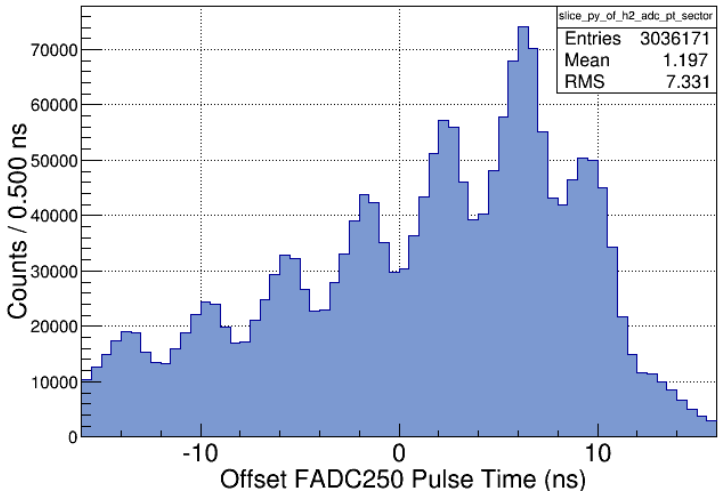

Figure 4.6: Start Counter FADC250 4 ns pulse time spectrum structure. Zoomed in look at a typical pulse time spectrum which has an applied offset to center the time around 0 ns. This spectrum is from sector 15, during the Spring 2015 run 2931.

time within the 4 ns sampling interval ($t(SN-1),\ t(SN+1)$) within the FADC250 readout window. Thus, each 4 ns time interval within the readout window will have

subsequent Gaussian distributions of t_{fine} quantities separated by 4 ns in time. This phenomenon is illustrated in Fig. 4.6.

The advantage of the FADC250's FPGA high resolution pulse time calculation is that the algorithm mimics that of a constant fraction discriminator (CFD) timing algorithm and effectively removes all time-walk effects [28] in the pulse time spectrum relative to signal amplitude. This effect is clearly illustrated in Fig. 4.7. Therefore, the high resolution pulse times returned by the FADC250 for hits in the

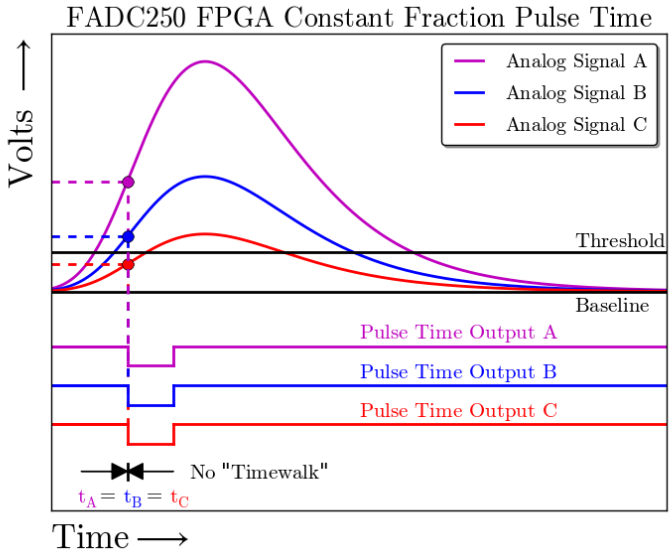

Figure 4.7: FADC250 FPGA Constant fraction pulse time. Simulation of three coincident signals of varying amplitude as read out by the FADC250s. The half-max of each signal is calculated as well as the corresponding pulse times.

ST can serve as a reference time when performing time-walk corrections. The time-walk effect, and lack thereof in the high resolution pulse time calculation, will be discussed in further detail in section 4.3.1.

4.2 GlueX Time to Digital Converters

The 30 ST analog signals dedicated for timing measurements have been amplified by a factor 5 relative to the ADC channels, are first fed into two 16 channel VME leading edge discriminator/scaler modules. The discriminator logic signals are output as differential ECL logic signals [29] and are fed into the front panel of Jefferson Lab's 32 channel high resolution, multi-hit, VME64x F1 time-to-digital converter (F1TDC) [30].

4.2.1 Start Counter F1TDC Configuration Parameters

The ST F1TDC channels are configured to run in the synchronous, high resolution mode. During the Spring 2015 run, the ST F1TDC's were configured to have individual channel resolutions (bin sizes) equal to 58.1 ps. This value can in fact be modified as needed by changing various F1TDC configuration parameters which are described in Table 4.2.

Variable	Definition	Value
`CLKPER`	F1TDC System clock period	32 ns (31.25 MHz)
`REFCNT`	Number of clock periods before value counter is reset	115
`REFCLKDIV`	Reference clock divider factor	128
`HSDIV`	High speed divider factor	232
`TFRAME`	Period of TDC Counter	3744 (ns)
`N`	Number of time bins	64466
τ	Channel resolution (bin size)	0.0581 (ns)

Table 4.2: F1TDC configuration variables. Variables used in the F1TDC resolution calculation during the Spring 2015 commissioning run.

In order to configure the F1TDC's to have a particular resolution one must first begin by defining certain configuration parameters to achieve the desired resolution. The clock period (`CLKPER`) is the clock period of the F1TDC, while the number of

clock periods before the value counter is reset is defined to be the reference counter (REFCNT). Therefore, Eq. 4.7 defines the period of the F1TDC counters, namely TFRAME.

$$\texttt{TFRAME = CLKPER } \times \texttt{ (REFCNT + 2)} = (32 \text{ ns}) \times (115 + 2) = 3744 \text{ ns} \tag{4.7}$$

To define the resolution of each F1TDC bin, one must then determine the number of time bins (N) which will populate the full period (TFRAME) of the F1TDC counters. Equation 4.8 describes the this very quantity.

$$\texttt{N=2}\times\texttt{(REFCNT+2)}\times\texttt{152}\times\frac{\texttt{HSDIV}}{\texttt{REFCLKDIV}} = 2 \times (115 + 2) \times 152 \times \frac{232}{128} = 64466 \tag{4.8}$$

The reference clock divider factor REFCLKDIV is always set to $2^7 = 128$ for the GlueX F1TDC systems. Therefore the two parameters dictating the number of time bins, and thus channel resolution, are the high speed divider factor (HSDIV) and the number of clock periods (REFCNT). It is useful to note that the factor 2 in Eq. 4.8 arises from the fact the ST F1TDC's are operating in high resolution mode and thus N must be doubled and τ halved. Moreover, the factor 152 in Eq. 4.8 is a constant within the F1TDC system [31]. Lastly, in order to determine the resolution of each F1TDC time bin, one needs only to calculate the quantity τ as shown in Eq. 4.9.

$$\tau = \frac{\texttt{TFRAME}}{\texttt{N}} = 0.0581 \text{ ns} \tag{4.9}$$

4.2.2 Start Counter F1TDC & Hit Times

As discussed previously in section 4.2.1 the ST F1TDC system clock has been configured to have a window (TFRAME) of 64466 channels (3.744 μs) during the Spring 2015 run. This means that the F1TDC counters will return integer values in the interval $[0, \text{N}]$ for every channel corresponding to an event trigger. These integer

values are easily converted to units of nanoseconds *via* the channel resolution parameter τ. Thus, the distribution of F1TDC times for each of the 30 ST channels will result in a spectrum uniform in time spanning the interval $[0, \texttt{TFRAME}]$ which is illustrated in Fig. 4.8.

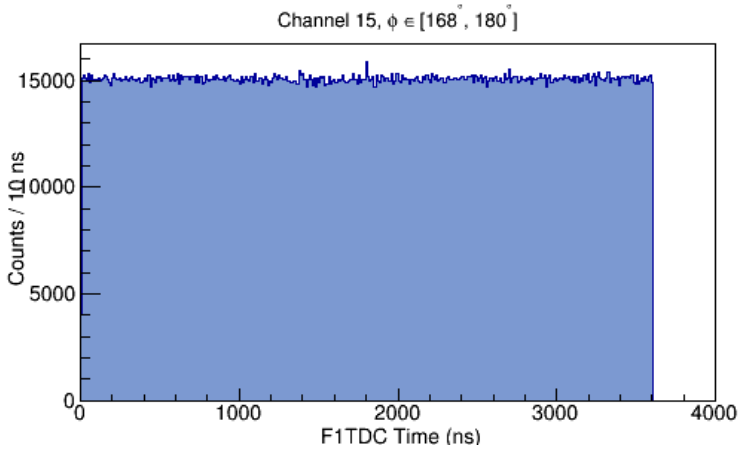

Figure 4.8: Typical F1TDC time spectrum. It is clearly visible that the distribution is uniform in time for the time interval $[0, \texttt{TFRAME}]$. This spectrum is from sector 15, during the Spring 2015 run 2931.

In order to extract a meaningful time relative to the event trigger time, it is imperative to define what exactly the trigger time is. There exists a global system clock, governed by a 250 MHz oscillator, which resides on the trigger supervisor (TS) board. Furthermore, there exists a register on the trigger interface (TI) board that counts the number of system clock cycles which have occurred since the beginning of the run [31] and is readily available in the data stream. Therefore, for each triggered event there exists a time (T_{trig}) that is equal to the period of the system clock times the number of system clock cycles (n_{TI}) that have elapsed since the beginning of the run (see Eq. 4.10)).

$$T_{trig} = (4 \text{ ns}) \cdot n_{TI} \tag{4.10}$$

In a similar fashion, the ST F1TDC channels report how many `TRFRAME` roll over periods have occurred since the beginning of the run (n_{RO}) as well as the high

resolution time since the most recent roll over (T_{window}). Since TFRAME is a fixed parameter, the F1TDC time for each ST channel corresponding to an event trigger (T_{tot}) is given by Eq. 4.11.

$$T_{tot} = N_{RO} \cdot \texttt{TFRAME} + T_{window} \tag{4.11}$$

In order to then know what the hit time in the ST F1TDC is relative to the time in which the trigger occurred for that particular event, one simply needs to calculate the difference shown in Eq. 4.12.

$$T_{TDC} = T_{trig} - T_{tot} \tag{4.12}$$

An example of a ST trigger corrected F1TDC time spectrum can be seen in Fig. 4.9 It is important to note that not all times recorded in Fig. 4.9 are useful or

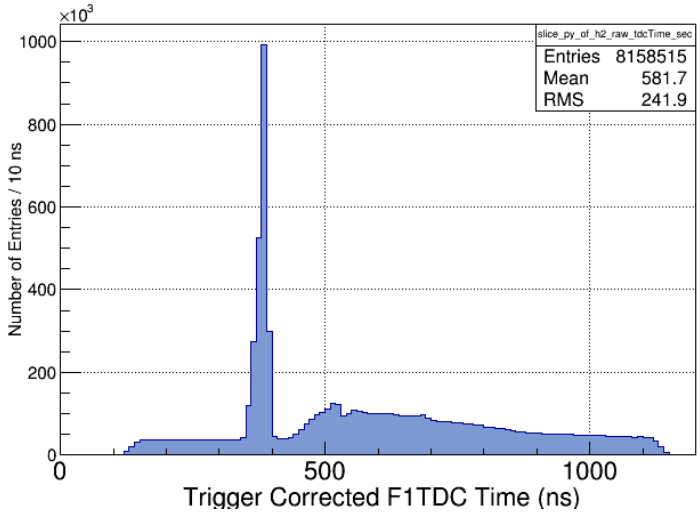

Figure 4.9: Typical Start Counter trigger corrected F1TDC time spectrum. There is indeed a preferred number of events that occur around 380 ns after the trigger arrived in the ST F1TDC crates. This spectrum is from sector 15, during the Spring 2015 run 2931.

even meaningful. There are a multitude of time differences that are completely out of time relative to the trigger time. Therefore, we define times of interest to only

be those that occur within ±60 ns of the main centroid located within the trigger corrected F1TDC time spectrum. In Fig. 4.9 the aforementioned times of interest are located at approximately 381 ± 60 ns. It is also useful to apply an arbitrary offset to the trigger corrected F1TDC time spectrum so that the centroid of useful times is located at zero. Thus, we are able to write the full expression for times reported by the ST F1TDC channels with 4.13 where O_i is an arbitrary offset that has been applied so that the centroid of the trigger corrected F1TDC time spectrum is centered around zero.

$$t_i^{TDC} = \tau \cdot T_{TDC} + O_i \tag{4.13}$$

The index $i \in [1, 30]$ indicates the particular ST channel of interest. Figure 4.10 illustrates a typical spectrum of useful offset trigger corrected F1TDC hit times for channel 15 in the ST (t_{15}^{TDC}).

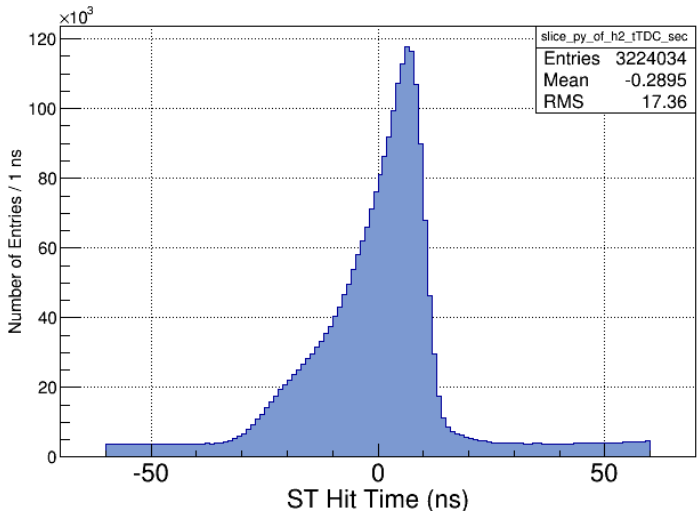

Figure 4.10: Typical Start Counter offset F1TDC hit time spectrum. This spectrum is merely a modification to the spectrum shown in Fig. 4.9. However, only times that occur within 0 ± 60 ns are considered as useful times. This spectrum is from sector 15, during the Spring 2015 run 2931.

4.3 Time-Walk Corrections

The time-walk effect is a well understood consequence of leading edge discriminators (LED). LEDs, as the name suggests, outputs a logic signal as soon as the leading edge of an incoming analog signal crosses a fixed threshold. Analog signals of varying amplitudes crossing a fixed threshold, as determined by the discriminator threshold setting, will do so at varying times.

4.3.1 Time-walk Effect

The time-walk effect is attributed to larger signals having faster rise times as compared to signals which have amplitudes close to the threshold setting, see Fig. 4.11. Due to the signal A having a larger amplitude as compared to signals B & C, it is

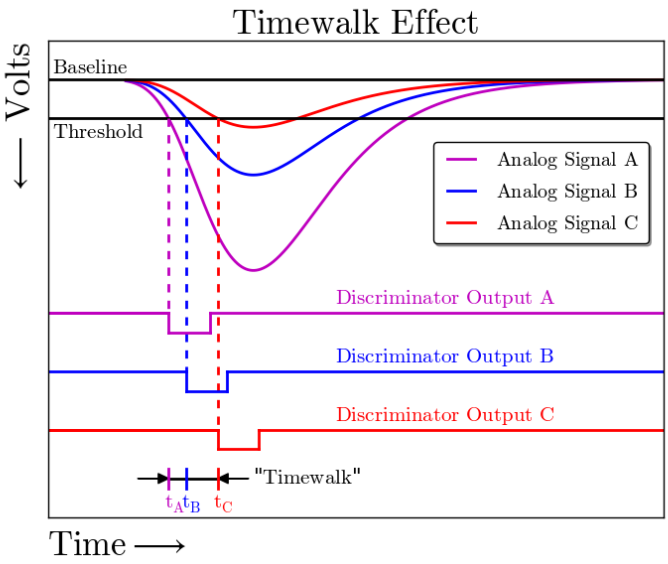

Figure 4.11: Example of the time-walk effect. Three coincident analog signals A, B, & C of varying amplitudes crossing a fixed threshold in a LED. The discriminator logic output signals vary in time relative to the amplitude of the incoming analog signal. The signals shown above are simulated analog signals being fed into the LED's thus, they have negative polarity.

clear that the logic signal output from the discriminator will "*walk about*" in time, resulting in the undesirable increase in time resolution of the systems TDC channels.

The time-walk effect can be corrected for in a number of ways. From a hardware standpoint, constant fraction discriminators (CFD) virtually eliminate all time-walk effects by generating the logic signal output when a particular fraction of the incoming signals amplitude is reached [28]. Unfortunately, this is a costly solution from a financial standpoint. However, software corrections for the time-walk effect are in fact achievable. The methods to perform time-walk corrections for the thirty Start Counter (ST) F1TDC channels are discussed below.

As mentioned in section 4.3.1 the TDC times reported by the LEDs are subject to the time-walk effect and must be corrected for *via* software so as to optimize the time resolution for each of the thirty Start Counter channels. In order to correct the TDC times (Eq. 4.13) returned by the F1TDC's one must first acquire a reference time for each hit in the ST, for each event.

4.3.2 F1TDC & FADC250 Time Difference

The TDC time, given by Eq. 4.13, alone will not suffice as the time spectrum to be time-walk corrected without a reference time since the trigger operates on a 250 MHz clock and causes an inherent 4 ns jitter associated with each event. However, this jitter is also present in the FADC250 pulse time, given by Eq. 4.6. Thus, a time difference between the TDC time and the ADC pulse time eliminates the 4 ns trigger jitter effect. Furthermore, as was illustrated in Fig. 4.7 in section 4.1.4 the FADC250 high resolution pulse time is not subject to time-walk effects thus making it a suitable time reference. Moreover, the FADC and TDC signals emanate from

the same location in the readout electronics and the cable lengths are identical. Thus, there are no cable propagation times to take into account.

A measure of this time difference distribution can be though of as a measurement of the "*self-timing*" resolution of each of the 30 ST sectors. It is useful to note that there exists another suitable time reference which could be used for these calibrations. That is the RF time provided by the accelerator. However, this time was not available at the time of these calibrations so the aforementioned time difference was implemented.

4.3.3 Time-walk Spectrum

Table 4.3 describes the necessary variables to describe the time-walk spectrum for the ST. The TDC/FADC time difference is given by Eq. 4.14.

Variable	**Definition**
a	Pulse peak (amplitude)
a_i^{thresh}	Discriminator threshold converted to ADC units
$c0_i, c1_i, c2_i$	Fit parameters
a_i^0	Most probable pulse peak
f_i^w	Functional form of time-walk fit
t_i^{TDC}	TDC time
T^w	Time walk corrected TDC time

Table 4.3: Time walk correction variables. Variables used in for the time walk corrections for the Start Counter.

$$\delta t_i = t_i^{TDC} - t_i^{FADC} \tag{4.14}$$

In Fig. 4.11 it was illustrated that the amplitude of each analog signal characterizes the time in which the leading edge crosses the threshold and thus, the time returned by the F1TDC. Figure 4.12 shows a typical time-walk spectrum for one sector of the ST. It is immediately obvious that there exists a correlation between the time and the

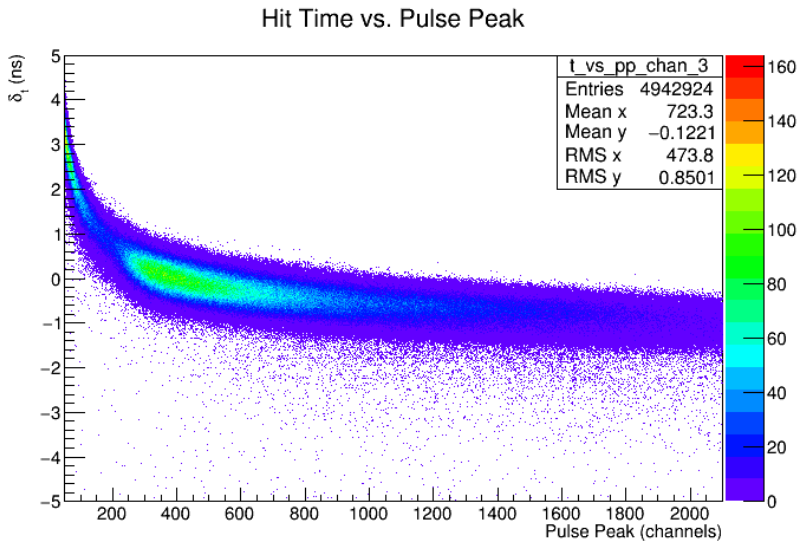

Figure 4.12: Typical Start Counter time-walk spectrum. Shown is the time-walk spectrum for sector 3 of the Start Counter during the Spring 2015 run 2931. On the y-axis is δt_3 and on the x-axis is the corresponding pedestal subtracted pulse peak spectrum. From this histogram it is clear that there is a correlation between the amplitude of the analog signal and the time in which the signal crosses the discriminator threshold.

pulse peak for hits in the ST. This correlation is nonlinear and requires a polynomial functional form to describe the correlation. Equation 4.15 from reference [27] was chosen to characterize the correlation between δt_i and the amplitude of the signal.

$$f_i^w(a/a_i^{thresh}) = c0_i + \frac{c1_i}{(a/a_i^{thresh})^{c2_i}} \tag{4.15}$$

The projection of the δt_3 (y-axis) is show in Fig. 4.13. The non time-walk corrected spectrum results in a poor time resolution due to the large time differences occurring among signals close to threshold and the more probable amplitudes being registered in the FADC. Figure 4.14 is the projection of the pedestal subtracted pulse peak (x-axis) of Fig. 4.12. It is required to subtract the pedestal from the pulse peak so that the absolute amplitude is being calculated.

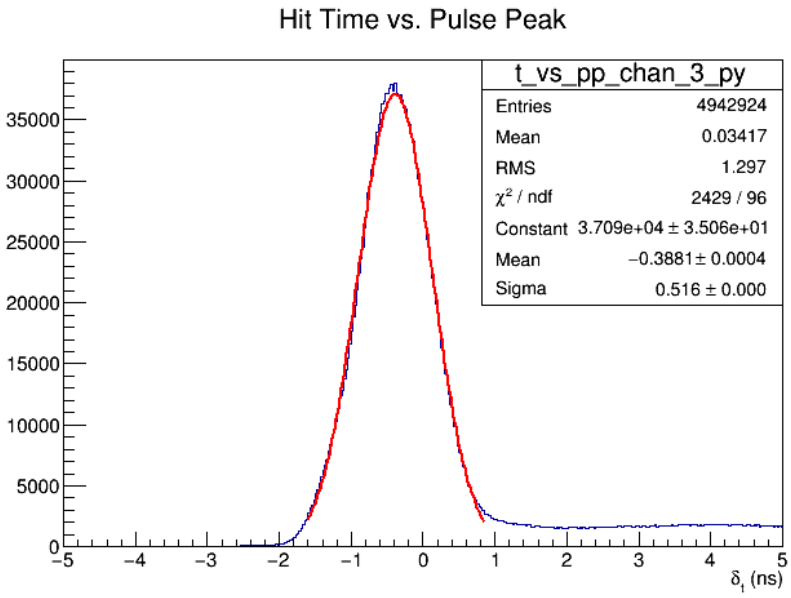

Figure 4.13: Typical Start Counter time difference spectrum. Shown is the time difference δt_3 spectrum for sector 3 of the Start Counter during the Spring 2015 run 2931. The uncorrected time-walk time spectrum has $\sigma_{\delta t_3} \approx 516ps$.

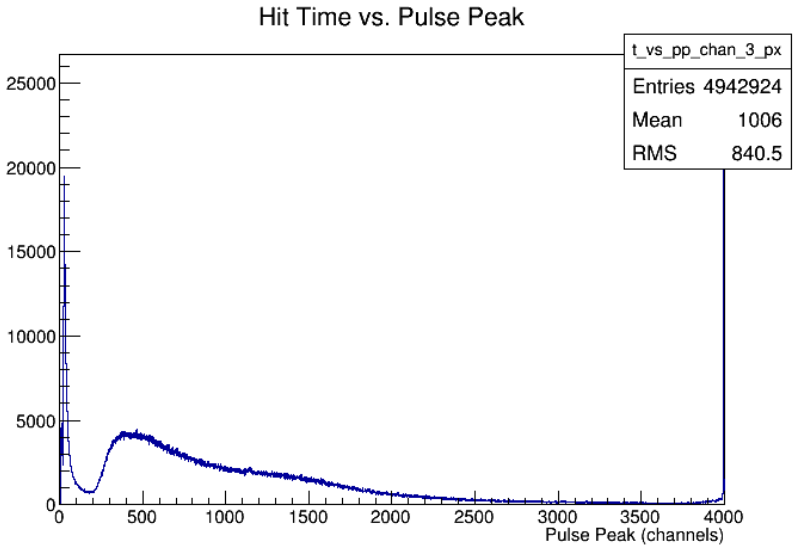

Figure 4.14: Typical Start Counter pedestal subtracted pulse peak spectrum. Shown is the pedestal subtracted pulse peak spectrum for sector 3 of the Start Counter during the Spring 2015 run 2931. It is important to note that the most probable value of the pulse peak spectrum is located somewhere within the minimum ionizing peak located around pulse peak value of 450.

4.3.4 Fitting the Time-walk Spectrum

In order to fit the nonlinear time-walk spectrum shown in Fig. 4.12 with the function given by Eq. 4.15 a custom fitting procedure was implemented instead of making use of ROOT's default fitter. The custom fitting procedure ultimately provides more control and a better understanding of how the correlation of the time difference and pulse peak behaves. For each individual pulse peak channel ranging from [50, 2100] the associated time difference for that channel was histogramed.

The time difference distributions contained within the individual pulse peak channels were first fit with a Gaussian function over the full 10 ns range of the histogram. The resulting fit parameters were then utilized to initialize, and subsequently perform, a second Gaussian fit which was fit over the range $[\mu - FWHM \cdot \sigma,\ \mu + FWHM \cdot \sigma]$ with the fir parameters μ and σ obtained from the previous fit, and FWHM being the full width half maximum (2.355) of a Gaussian distribution. This fit is illustrated in Fig. 4.15. This method provides the most accurate measure of the mean time corresponding to a particular pulse peak channel.

Pulse peak channels below 50 correspond to signals that are very close the threshold and are potentially polluted with noise. While channels greater than 2100 have very low statistics and fitting the time difference distributions for these channels produced unreliable fits. Thus, these channels were deemed to be unfit to characterize the time difference and pulse peak correlation and were omitted from the time walk spectrum fit.

With the time difference mean and associated errors obtained from the method outlined above, they were plotted against their respective pulse peak channels seen in Fig. 4.16. The most probable value (MPV) of the minimum ionizing peak was chosen to be the location in which the time-walk correction was zero. This location effectively serves as a reference point for the correction. Since the location of this

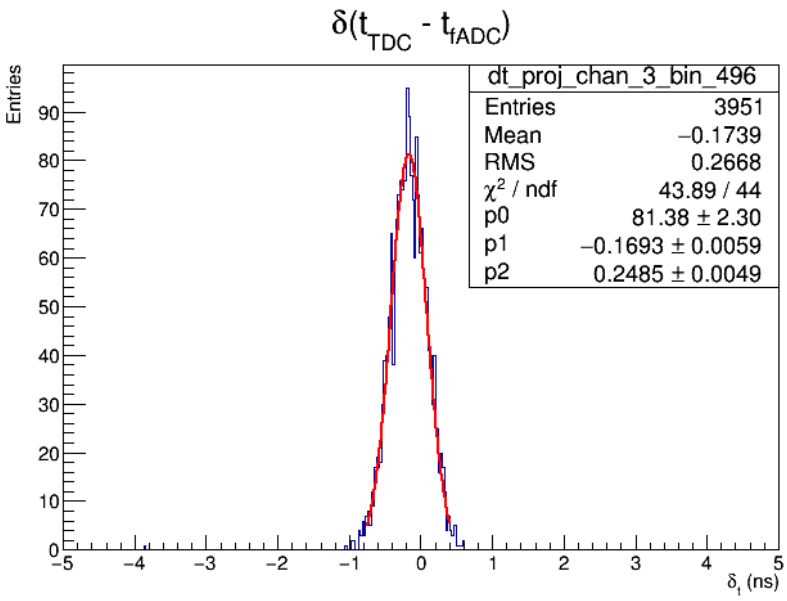

Figure 4.15: Typical Start Counter time difference/pulse peak channel spectrum. Shown is the pulse peak spectrum for channel 496 in sector 3 during the Spring 2015 run 2931.

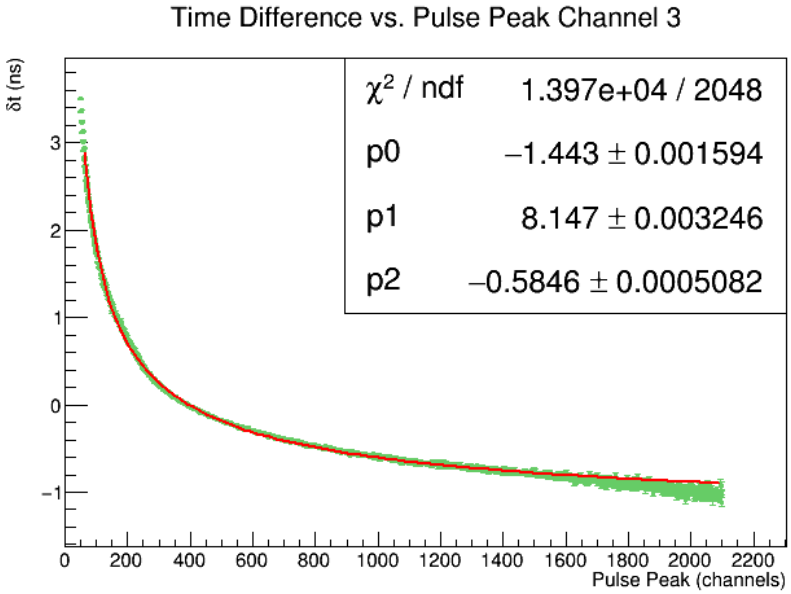

Figure 4.16: Typical Start Counter custom time-walk fit. Shown is the custom time-walk fit for sector 3 during the Spring 2015 run 2931. ROOT's fitting library Minuit was utilized to perform a χ^2 minimization to the data. It should be noted that in the plot above the parameters $p0,\ p1,\ p2$ are $c0_3,\ c1_3,\ c2_3$ respectively.

point is completely arbitrary no effort was put forth to properly determine the MPV by fitting the individual pulse peak spectrum with a Vavilov or convoluted Landau-Gaussian distribution. Instead, as seen in Fig. 4.17 a "pseudo" MPV was utilized. The "pseudo" MPV (a_i^0) was determined on a sector by sector basis by

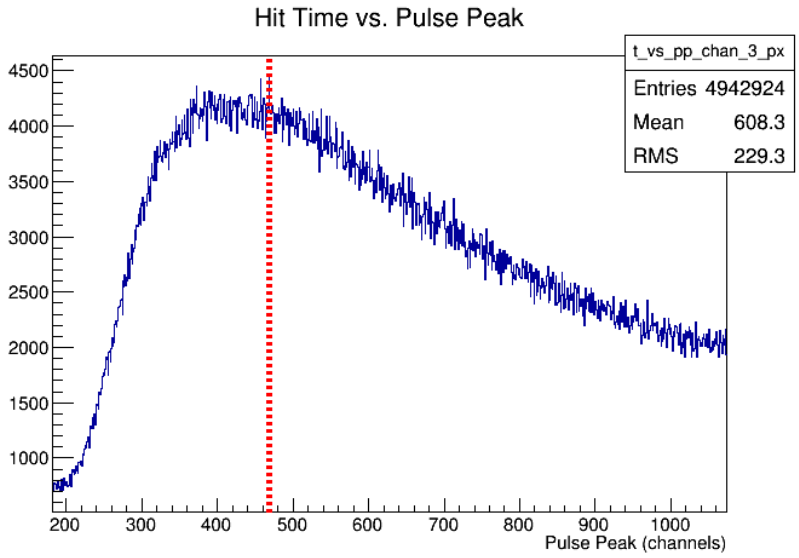

Figure 4.17: Typical Start Counter pulse peak minimum ionizing distribution. Shown is the pulse peak minimum ionizing distribution for sector 3 during the Spring 2015 run 2931. The red, verticle, dashed line in the histogram corresponds to the "pseudo" MPV (a_3^0) which was determined to be 469.

simply acquiring the pulse peak channel which had the most number of entries after the pulse peak channel 200. The large spike in the pulse peak spectrum at very low pulse peak values are most likely due to electromagnetic background in the event and do not correspond to a true minimum ionizing particle traversing the scintillator medium.

With all the necessary parameters, *i.e.* a_i^0, $c0_i$, $c1_i$, $c2_i$, determined the time-walk correction factor can be applied to the original TDC time. The functional form of the time-walk corrected time is given by Eq. 4.16.

$$T_i^w = t_i^{TDC} - f_i^w(a/a_i^{thresh}) + f_i^w(a_i^0/a_i^{thresh}) \tag{4.16}$$

4.3.5 Time-walk Correction Effects

Once the time walk corrections have been applied, the corrected timing distributions appear much more uniform in nature and exhibit a factor 1.75 improvement in resolution. Figure 4.18 illustrates the vast improvement in the time difference spectrum (δt_3) due to the applied time-walk corrections. Studies showed that not

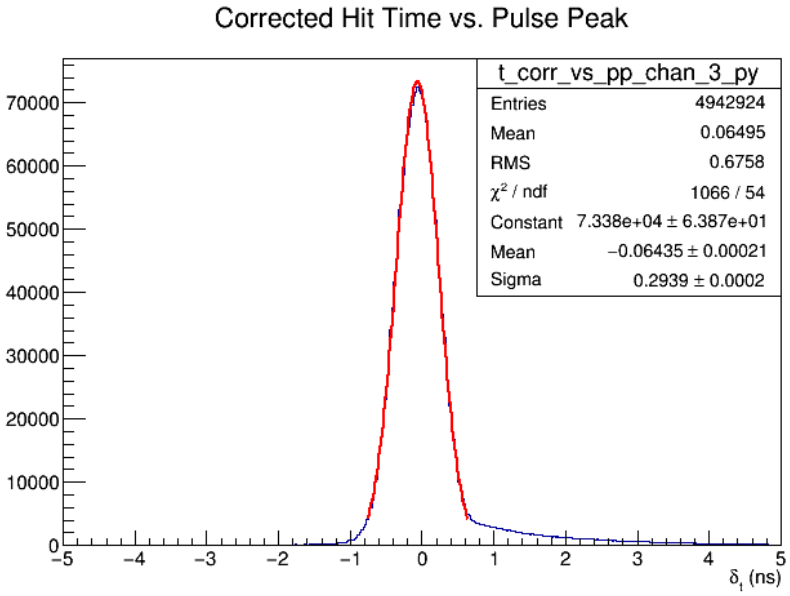

Figure 4.18: Time-walk Start Counter corrected time difference spectrum. Shown is the time-walk corrected time difference spectrum for sector 3 during the Spring 2015 run 2931. The time-walk corrected time difference spectrum has $\sigma_{\delta t_3} \approx 293ps$

only did the custom fitting procedures provide for a better, and more uniform, self timing resolution, the constants determined from the custom fitting procedure have much less variation than what was determined using the default ROOT fitter. The default ROOT fitter here is defined to be the utilization of ROOT's MINUIT χ^2 minimization fitting library to data which have been arbitrarily correlated. As can be seen in Fig. 4.19 the custom fitting procedures did no worse than the default ROOT fitter procedure. While the improvement of the custom fitting procedure is

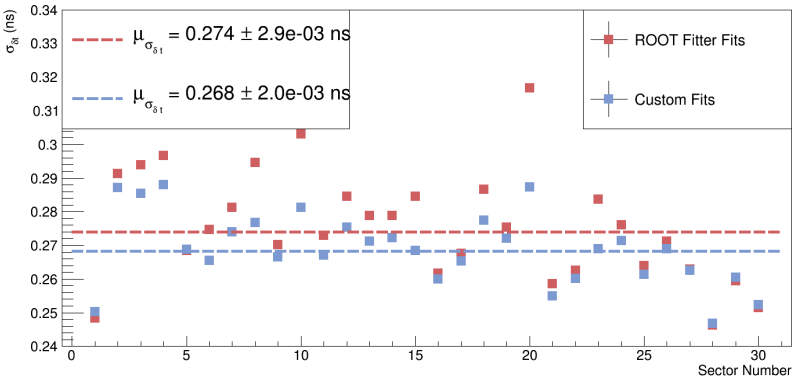

Figure 4.19: Start Counter self timing resolutions. Comparison of the self timing resolutions obtained after the time-walk corrections have been applied. The custom fitting procedures discussed above resulted in an average time resolution of $268 \pm 2ps$ among the 30 sectors of the ST.

not significantly better than the default ROOT fitter, it is more robust and well understood.

4.4 Attenuation Corrections

When photons traverse through a scintillator medium, or any medium containing matter, they can be lost through scattering, absorption, or escape at the boundaries. Attenuation corresponds to the reduction in observed light relative to the amount of initial scintillation light produced in the medium.

4.4.1 Attenuation of Photons in a Scintillator Medium

Photons produced in a scintillator medium, as a result of charged particles traversing through the material, are subject to the property of total internal reflection. The scintillator material for the ST paddles is EJ-200 with polyvinyltoluene acting as the polymer base [20]. If the resulting photons incident on the scintillator-air boundary have an angle of incidence which is smaller than the critical angle, then the photons

will leave the scintillator medium and be lost for detection and thus contribute to the overall attenuation. However, if the incident photon has an angle of incidence which is equal to or greater than the critical angle then those photons will totally internally reflect and may possibly be detected. It is useful to note that the EJ-200 scintillator material used in the Start Counter has an index of refraction of 1.58 [20] which results in the scintillator-air interface to have a critical angle of 39.3°. The photons that do in fact totally internally reflect however, are still subject to additional phenomena which contribute to the overall attenuation of photons in the scintillator medium.

With the above factors considered, one can define a parameter known as the "attenuation coefficient" which characterizes a particular materials ability to absorb photons. The attenuation coefficient is defined to be the length in the medium in which the initial number of primary photons are reduced by a factor of $1/e$ (36.8%). Since the loss of photons in scintillators equates to the loss of information relative to the event of interest, it is highly desirable to have a scintillator material with a long attenuation length. As a reference a flat $2 \times 20 \times 300$ cm^3 EJ-200 scintillator has a relatively long attenuation length on the order of 4 m.

4.4.2 Data Acquisition for Attenuation Corrections

In order to characterize the attenuation properties of the 30 ST scintillator paddles bench data obtained at FIU utilizing the custom test stand and ^{90}Sr source were analysed to provide an initial attenuation correction. Many efforts to utilize beam data acquired in the Spring 2015 commissioning run proved futile as there was a clear lack of statistics to perform such a calibration. Thus, the bench data was used since it at least provided a first order correction to account for attenuation in the ST scintillator paddles.

The custom test stand fabricated at FIU allows a ^{90}Sr beta source, which produces minimum ionizing electrons ranging in energy from 0.5 - 2.3 MeV electrons [32] [33], to be placed at twelve precise locations along the scintillator paddle. We define the variable z to be the distance along the scintillator path, which takes into account the paddle geometry, with the origin ($z = 0$ cm) being located at the beginning of the straight section and the end ($z \approx 59$ cm) being the tip of the nose.

The ^{90}Sr source is placed at four locations in the straight section, ≈ 8 cm apart starting at $z = 8.68$ cm. Additionally the source is placed at three locations in the bend section ≈ 1.3 cm apart, and five locations in the nose section ≈ 3 cm apart. Light produced in the scintillators by the ^{90}Sr beta spectrum are readout utilizing silicon photomultipliers (SiPM) detectors configured in the same manner as was used in the ST readout installed in HallD. An event trigger photomultiplier (PMT) was implemented so as to provide a reference (start) time. Both ADC and TDC data, corresponding to 10,000 event triggers, were collected for all 30 ST scintillator paddles at the exact same 12 discrete locations described above utilizing the same ^{90}Sr source.

For each of the twelve locations along the scintillator paddle ADC data was collected. A typical ADC spectrum at one location in the straight section is illustrated in Fig. 4.20. The peak corresponding to scintillation light being detected by the SIPM detector is clearly visible and located around ADC channel 225, while the pedestal governed by DC offset and electronic noise is centered around channel 50. In order to calculate the true ADC value of interest, it is required to completely isolate the peak and pedestal and fit the corresponding spectra with a Gaussian distribution so that the relative difference in their means, determined by the fit, may be calculated.

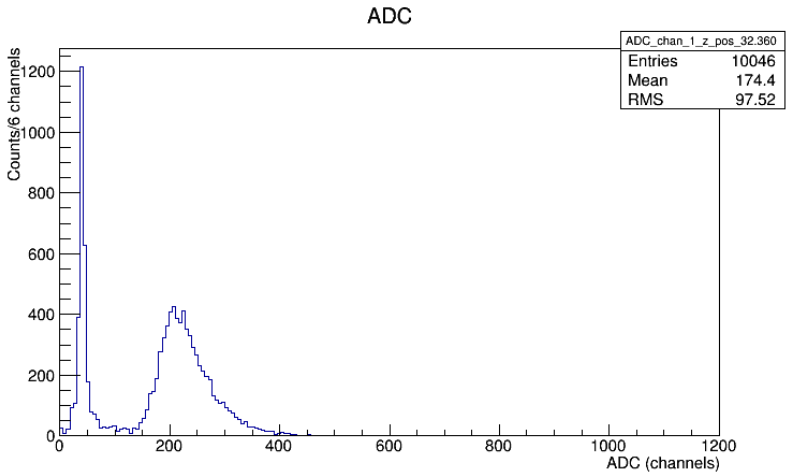

Figure 4.20: Typical Start Counter bench ADC spectrum. Shown is the ADC spectrum for sector 1 with the 90^{Sr} source located in the straight section at z = 32.36 cm. Both the pedestal (left) and peak (right) are clearly visible in this spectrum.

One way to do this is to make use of the TDC data that was taken simultaneously with the ADC data. The TDC data, which corresponds to the time difference between the trigger time and the hit time in the SiPM, was collected utilizing a CFD. Thus, no time-walk corrections to the data were necessary. A typical TDC time spectrum can be seen in Fig. 4.21. An initial fit to the entire dynamic range of the TDC data was performed so as to "hunt" for the Gaussian distribution. Utilizing the parameters determined from the initial fit, a second fit was performed so that the explicit fit range $\mu \pm 7\sigma$ could be determined. Once the fit range was defined any ADC event with a corresponding hit time that fell within the $\mu \pm 7\sigma$ TDC time window, was declared as a good peak signal. However, any ADC event not satisfying the aforementioned condition was declared as a pedestal signal. It is useful to note that the σ obtained from the second fit is a measure of the time resolution of a ST paddle at that particular location along the length of the scintillator.

Once the peak and pedestal histograms were isolated a similar fitting procedure to the data, outlined in detail in section 4.3.4, was implemented so as to extract

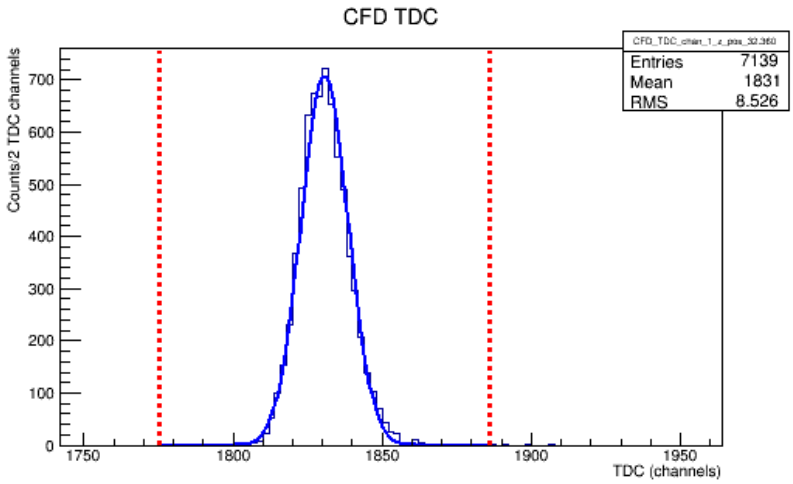

Figure 4.21: Typical Start Counter bench TDC spectrum. Shown is the TDC spectrum for sector 1 with the 90^{Sr} source located in the straight section at z = 32.36 cm. The blue line indicates a Gaussian fit to the data while the red vertical dashed red lines indicate the $\mu \pm 7\sigma$ range which defines the hit to be and out of time. At this location $\sigma \approx 390ps$.

their mean values so that the true ADC mean value could be obtained. Figure 4.22 shows the ADC pedestal corresponding to the aforementioned TDC cuts.

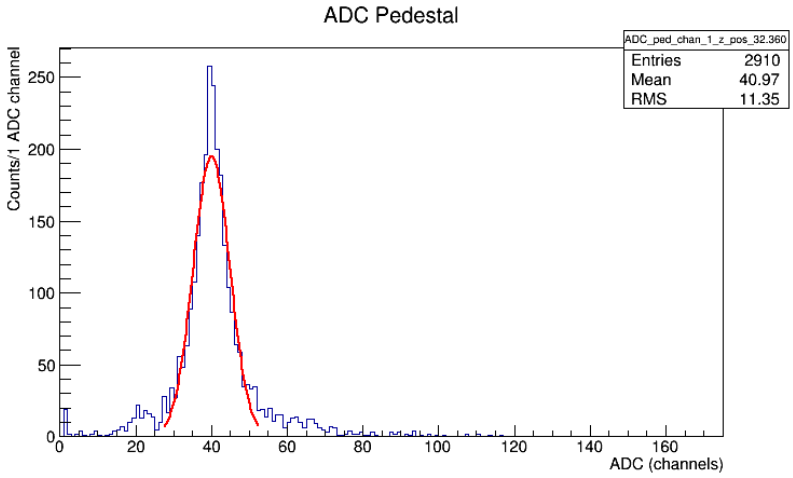

Figure 4.22: Typical Start Counter bench ADC pedestal spectrum. Shown is the ADC pedestal spectrum for sector 1 with the 90^{Sr} source located in the straight section at z = 32.36 cm. The hit time returned by the TDC was outside the $\mu \pm 7\sigma$ time window. A similar fit was applied to the ADC peak data.

Upon calculating the difference $\mu_{peak} - \mu_{ped}$ from the ADC spectra at each of the twelve locations along the length of the ST sector 1 one obtains Fig. 4.23 which is the pedestal corrected mean ADC values characterizing the attenuation properties of the unique ST scintillator geometry.

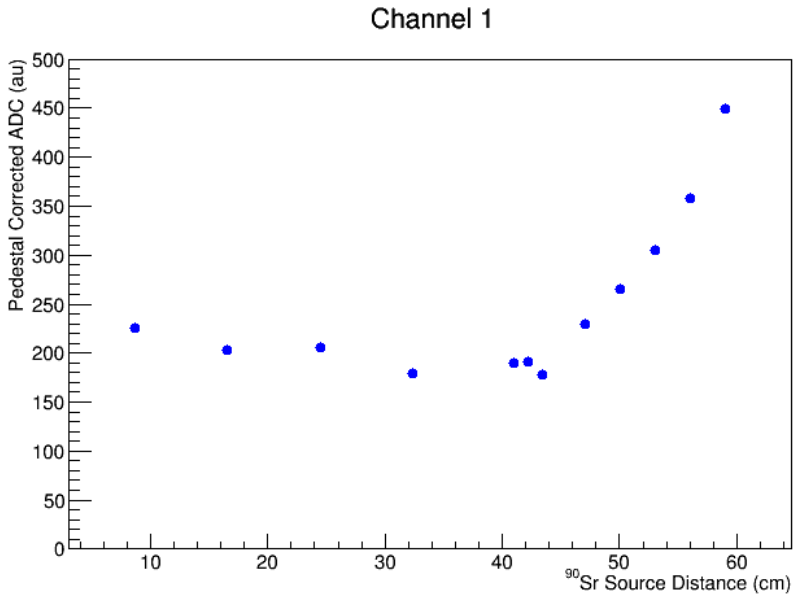

Figure 4.23: Typical Start Counter bench attenuation data. Shown is the attenuation data for sector 1. It is clear that there exists attenuation (light loss) in the straight section as the source moves further away from the SiPM. However, the interesting, and beneficial, phenomenon of light amplification as the source moves further away in the nose section is also noticeable.

Figure 4.24 illustrates the time resolution characteristics of a typical ST paddle at the twelve individual ^{90}Sr locations. The time resolution in the straight section at $z = 32.36$ cm was found to be ≈ 390 ps while the time resolution at the tip of nose was found to be ≈ 235 ps. This effect is due to the unique tapering trapezoidal geometry of the nose section. It is worth noting that the same increase in light output in the nose section was observed utilizing beam data and selecting fast pions ($p > 1.0$ GeV) matched to the ST so as to ensure the particles were minimum ionizing.

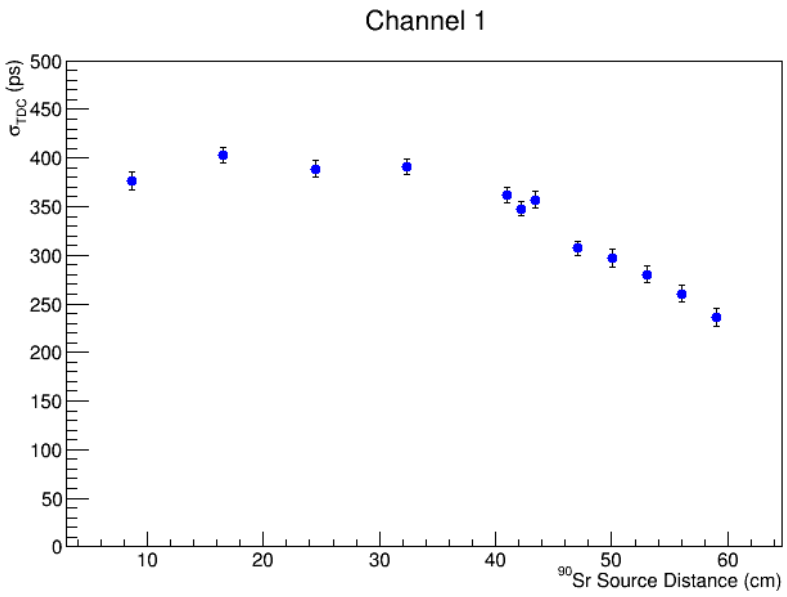

Figure 4.24: Typical Start Counter bench time resolution data. Shown is the time resolution data for sector 1. It is clear that there is a linear increase in time resolution in the straight section as the source moves further away from the SiPM. However, the interesting, and beneficial, phenomenon of time resolution improvement as the source moves further away in the nose section is also noticeable.

Upon comparing figures 4.23 and 4.24 it is adamantly clear that the geometry of the nose section gives rise to an increase in light collection at the upstream end of the straight section. This phenomenon is at first counterintuitive. However, the effective path length and number of reflections of photons traversing through this tapered section of the scintillator paddle is reduced relative to the non-tapering section present in the straight section. These figures also indicate that the while straight section is trapezoidal, it exhibits the behaviour of a typical rectangular scintillator bar which is to be expected.

4.4.3 Attenuation Corrections

As was discussed in section 4.4.2 the unique geometry of the ST causes for the the two distinct regions, *i.e* straight and bend/nose, to have differing properties in terms

of light output and thus, time resolution. Therefore, when performing attenuation corrections the two regions must be treated independently in order to properly characterize photon attenuation in their respective regions. At the transition region, where the end of the straight section meets the start of the bend/nose section, the difference in the two independent fit functions evaluated at $z = 40.0$ cm was found to be minimal. Thus, no effort was put forth to ensure that this transition region was continuous.

After many studies it was empirically determined that the ideal fit function for the straight section would follow Eq. 4.17.

$$f_S(z) = A_S e^{B_S \cdot z} \tag{4.17}$$

Similarly, the functional form of the bend/nose section follows Eq. 4.18.

$$f_{BN}(z) = A_{BN} e^{B_{BN} \cdot z} + C_{BN} \tag{4.18}$$

Exponential decay functions are typically used to describe the attenuations of photons in scintillator material. However, for the unique case of the bend/nose section, an exponential growth function was utilized. In order to investigate the possibility of utilizing a single functional form to describe the entire length of a scintillator paddle, a polynomial of $\mathcal{O}(5)$ was also studied.

Figure 4.25 illustrates the ADC mean vs. ^{90}Sr distance for sectors 5 and 23. In the bend/nose region it is clear that both the polynomial and exponential growth function fit the data well and are very similar in nature. For the straight section there is also good agreement between the exponential decay function and the polynomial for $z > 9$ cm. While Fig. 4.25 serves as two examples in which the polynomial could potentially describe the attenuation of photons for the region $z < 9$ cm, Fig. 4.26 illustrates that for sectors 15 & 13 the polynomial fit can severely under or over estimate the ADC mean values respectively.

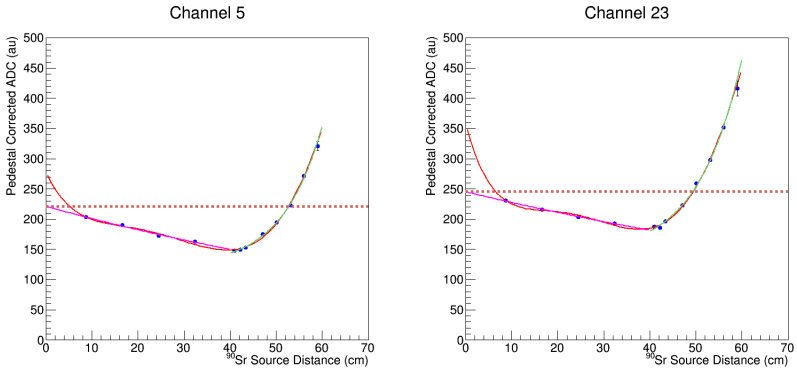

Figure 4.25: Attenuation corrections: Good ADC fits. Two particular cases in which the polynomial of $\mathcal{O}(5)$ fits the ADC mean data relatively well. The red line corresponds to the polynomial of $\mathcal{O}(5)$ fit. The magenta line is the exponential fit to straight section [0 cm, 40 cm] while the green line is the exponential fit to the bend/nose section [40 cm, 60 cm]. Sector 5 is on the left while sector 23 is on the right. The red horizontal dashed line corresponds to the value of the exponential fit in the straight section evaluated at z = 0 cm.

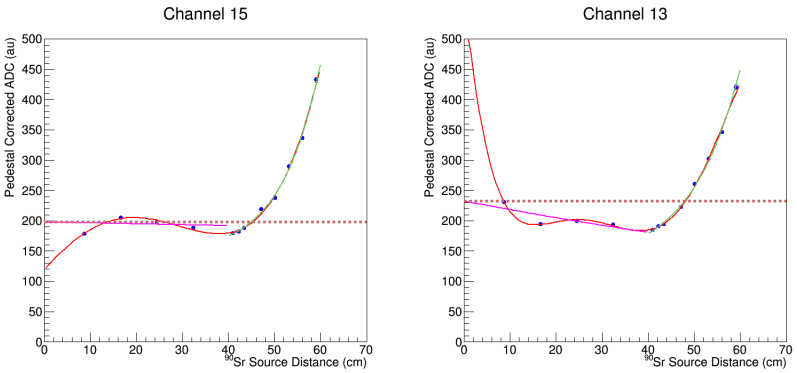

Figure 4.26: Attenuation corrections: Bad ADC fits. Two particular cases in which the polynomial of $\mathcal{O}(5)$ fails to fit the ADC mean data. The red line corresponds to the polynomial of $\mathcal{O}(5)$ fit. The magenta line is the exponential fit to straight section [0 cm, 40 cm] while the green line is the exponential fit to the bend/nose section [40 cm, 60 cm]. Sector 15 is on the left while sector 13 is on the right. The red horizontal dashed line corresponds to the value of the exponential fit in the straight section evaluated at z = 0 cm.

Because the region $z < 9$ cm has no data it is critical that the fit function in this region be well behaved and provide a reliable extrapolation as $z \to 0$. Polynomial fits "blowing up" in regions with a lack of data is a well known effect and since fits to many of the ADC bench data exhibited this feature, the method of utilizing two

individual piecewise exponential functions to fit the two distinct regions of the ST paddles were implemented.

The exponential fits seem to do a decent job of estimating the attenuation behaviour in situations where the data is somewhat unreliable.

The energy deposited (dE_{hit}) by a charged particle in a scintillator medium is proportional the number of photons created, which is in turn proportional to the pulse integral of the signal read out by the FADC250. However, since the photons created *via.* ionization are subject to attenuation as they traverse through the scintillator medium, the energy deposition measured by the SiPM does not correctly measure the energy deposited by the charged particle at the location of intersection with the scintillator. A plot of the uncorrected energy deposition per unit length versus momentum (dE_{hit}/dx *vs.* p) in the ST is shown in Fig. 4.27.

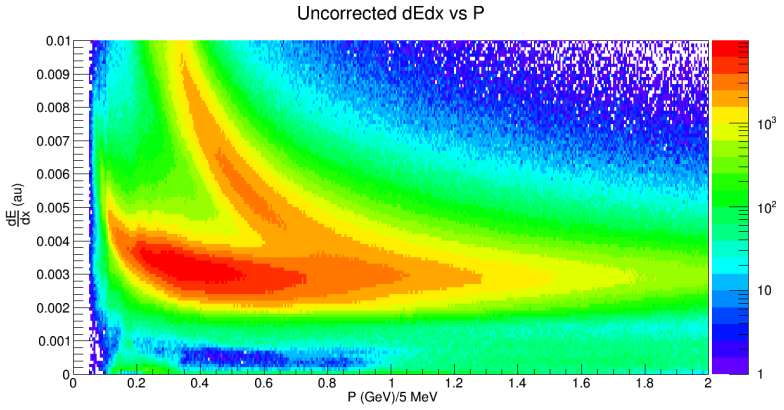

Figure 4.27: Typical uncorrected dE/dx *vs.* p distribution in the Start Counter. Shown is the uncorrected dE/dx *vs.* p distribution for tracks matched to the Start Counter in the Spring 2015 run 2931. The "banana band" corresponds to protons while the horizontal band corresponds to charged electrons, pions, and kaons. It is clear that pion/proton separation is quite difficult to achieve for tracks with $p > 0.6\ GeV/c$.

Evaluating the fit function in the straight section at $z = 0$ cm is representative of a minimum ionizing particle traversing through virtually no scintillator material,

and is thus subject to no effects of attenuation. Therefore, for all charged particles passing trough the ST scintillator paddles we apply an attenuation correction to the deposited energy measurement (dE_{hit}) to preserve the information regardless of where the track intersects the paddles. The corrected energy deposition (dE_{corr}) is given by Eq. 4.19 where the index i indicates which section the charged track intersected with.

$$dE_{corr} = dE_{hit} \cdot R_i \tag{4.19}$$

For the straight section we have Eq. 4.20.

$$R_S = \frac{f_S(0.0)}{f_S(z)} = e^{-B_S \cdot z} \tag{4.20}$$

For the bend/nose section we have Eq. 4.21.

$$R_{BN} = \frac{f_S(0.0)}{f_{BN}(z)} = \frac{A_S}{A_{BN} e^{B_{BN} \cdot z} + C_{BN}} \tag{4.21}$$

Thus, for every hit along the length of the ST paddles we find equations 4.22 & 4.23.

$$f_S(z) \cdot R_S = A_S \tag{4.22}$$

$$f_{BN}(z) \cdot R_{BN} = A_S \tag{4.23}$$

Once all energy deposition measurements have had the appropriate attenuation corrections applied as was discussed above, a plot of the energy deposition per unit length versus momentum ($dE_{corr}/dx \; vs. \; p$) in the ST is shown in Fig. 4.28.

Granted the Start Counter was not designed with particle identification (PID) in mind, it is pleasant to know that the ST can in fact be used, at some level, for PID studies.

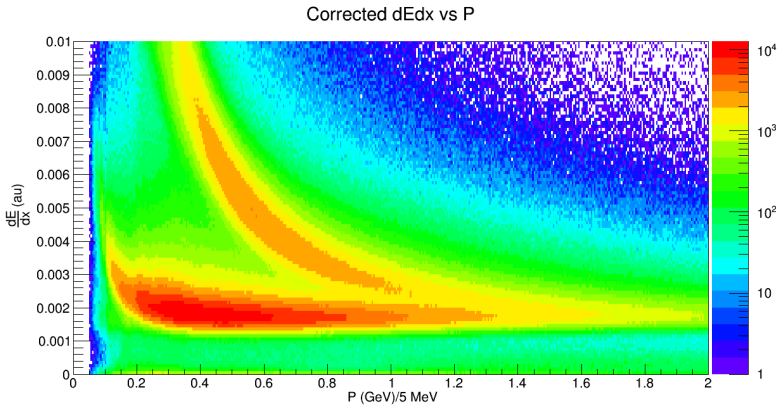

Figure 4.28: Typical corrected dE/dx *vs.* p distribution in the Start Counter. Shown is the corrected dE/dx *vs.* p distribution for tracks matched to the Start Counter in the Spring 2015 run 2931. The "banana band" corresponds to protons while the horizontal band corresponds to charged electrons, pions, and kaons. It is clear that pion/proton separation is achievable for tracks with $p > 1.1$ GeV/c.

4.5 Propagation Time Corrections

As a charged particle traverses through the Start Counter scintillator material the molecules become excited and a small fraction ($\approx 3\%$) [34] of the excitation energy is released in the form of "optical" photons. The photons produced will be emitted uniformly in all directions and some will escape the medium, some will be reflected back into the medium by virtue of the reflective AL foil wrapping, and some will be lost. However, the photons which are in fact not lost, will totally internally reflect until they reach the SiPM detector placed at the upstream end. The moment the photons are produced they will begin to propagate through the scintillator medium until they are eventually detected. The time from production to the time of detection in the ST scintillator paddles must be accounted for and is discussed below.

4.5.1 Light Propagation in Scintillators

The EJ-200 scintillator material has a refractive index equal to 1.58 [20] meaning that light in the medium will travel with a velocity $\approx 19\ cm/ns$. However, what is measured in the lab is known as the effective velocity which is slower due to the fact that the majority of photons are not travelling in straight lines parallel to the medium boundaries. Instead they are constantly reflecting off the boundaries meaning there is an increase in their respective path lengths which contributes to an observed reduction in velocity. This velocity is known as the effective velocity.

Both the CLAS Start Counter and the GlueX Start Counter were manufactured with the EJ-200 scintillator material and are comparable in thickness's and lengths. CLAS's Start Counter was 2.15 mm thick and 50.2 cm long [35]. While the GlueX Start Counter is 3 mm thick and 60.0 cm long. Therefore the effective velocities of photons should be quite similar. In fact, bench studies made at FIU, as well as beam studies with π^-'s, illustrated that the straight section had an effective velocity on the order of 14 cm/ns. It was found that photons propagating in the straight section ("leg") of the CLAS Start Counter, had an effective velocity of $13 \pm 1\ cm/ns$ [35].

Correcting for the time in which light spends traversing through the scintillator material is an important correction since the ST paddles are 60 cm in length. Thus, light produced in the tip of the nose will take on the order of 4 ns to reach the SiPM at the upstream end. Performing the propagation time corrections utilizing the common effective velocity method is not the most robust procedure for the case of the ST. Both bench and beam studies showed that the unique geometry in the bend and nose region cause the effective velocity of light in these two regions to be larger than that of the straight section. It was found that the light in the bend region had an effective velocity of $\approx 17\ cm/ns$ while the nose region had an effective

velocity of $\approx$ 20 cm/ns. These corrections proved to not be the most optimal correction so as to minimize the time resolution of the ST paddles.

4.5.2 Propagation Time Correction Event Selection

In order to conduct the propagation time corrections for the ST a distinct set of events needed to be selected so that a well understood reference time was being utilized. This reference time would then act as a measure of the event time for all other charged tracks intersecting the ST in the same event. For every charged track in a given event, three global tracking requirements were required. First, only charged tracks with a tracking confidence level, or tracking figure of merit (FOM), greater than 0.0027 were considered as can be seen in Fig. 4.29. Secondly all charged

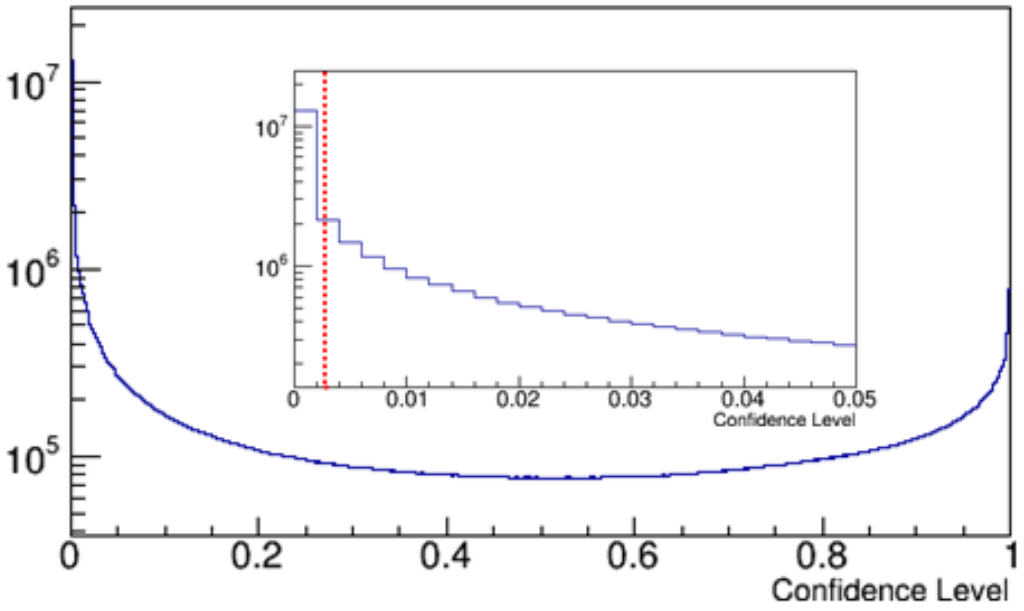

Figure 4.29: Spring 2015 run 2931 confidence level of charged tracks. Shown is the confidence level (FOM) for charged tracks in the Spring 2015 run 2931. The inset histogram illustrates the confidence level cut. All tracks with a confidence level $<$ 0.0027 were not considered. Note the log scale on the y-axis.

tracks were required to have the z coordinate of its vertex to be contained with in

the target geometry *i.e.* 50.0 cm $< z_{\text{vertex}} <$ 80.0 cm illustrated in Fig. 4.30 and the

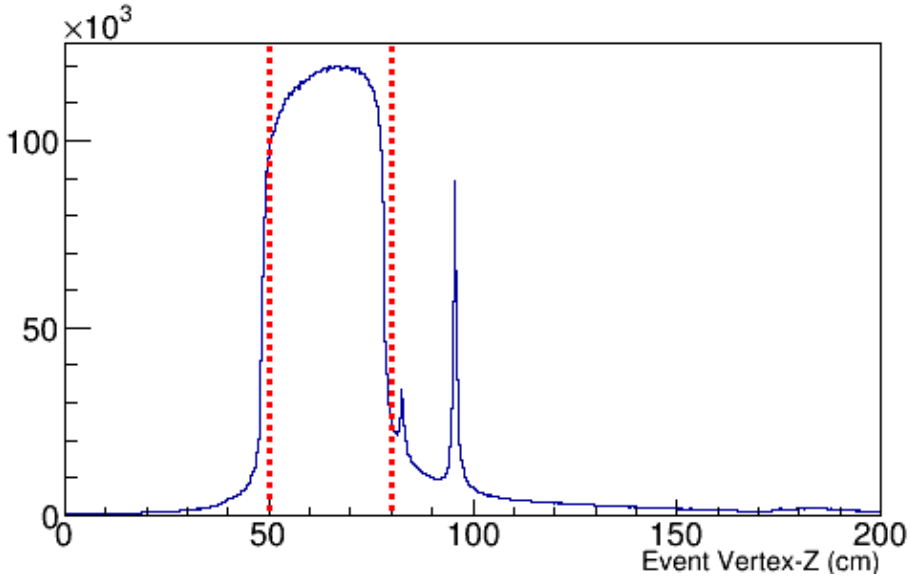

Figure 4.30: Spring 2015 run 2931 charged track z vertex distribution. Shown is the charged track z vertex distribution. Downstream of the target, from left to right, is the thin kapton exit window of the target and a thin plastic target placed at the end of the Start Counter. The area between the red dashed vertical lines indicate the range of z coordinates comprising the target length.

r coordinate of its vertex be contained with the geometry of the scattering chamber *i.e.* $r_{vertex} = \sqrt{x_{vertex}^2 + y_{vertex}^2} < 3.745$ cm illustrated in Fig. 4.5.2. It is useful to note that in an ideal situation only tracks with their respective r_{vertex} coordinate occurring within the beam diameter should be considered. However, the severe limit in statistics from the Spring 2015 commissioning run required this cut to be loose so that a first order calibration could be conducted.

For each event, if there existed a single π^- track with $p > 0.5$ GeV/c, while passing the aforementioned "global" tracking requirements, this track was considered to be a candidate to serve as the event time for that event. Figure 4.32 illustrates the π^- track candidates for this particular study. Fast π^-'s were chosen as a suitable

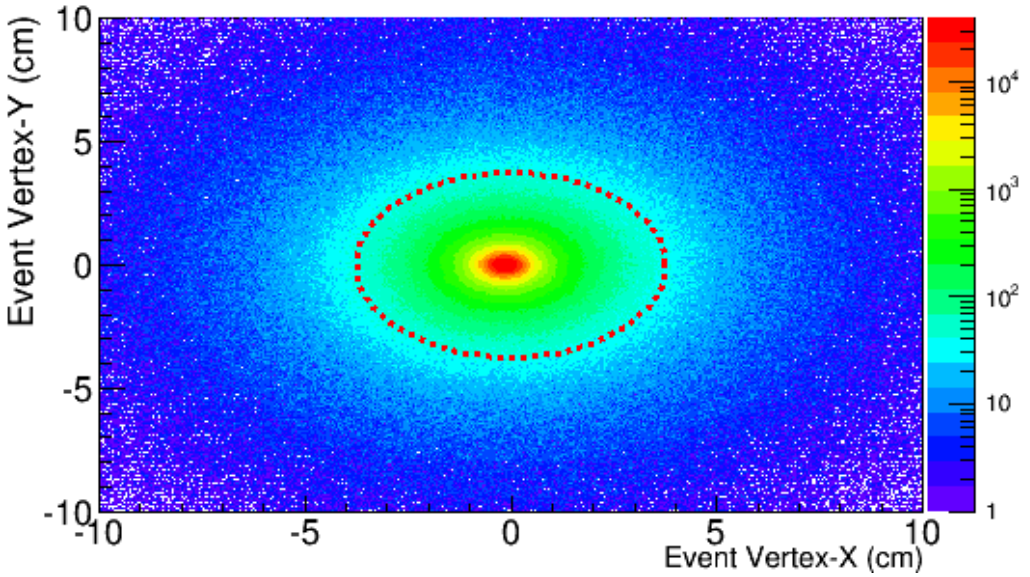

Figure 4.31: [
Spring 2015 run 2931 charged track r vertex distribution. Shown is the charged track r vertex distribution. The area inside the red dashed circle indicate the range of r coordinates comprising the scattering chamber.

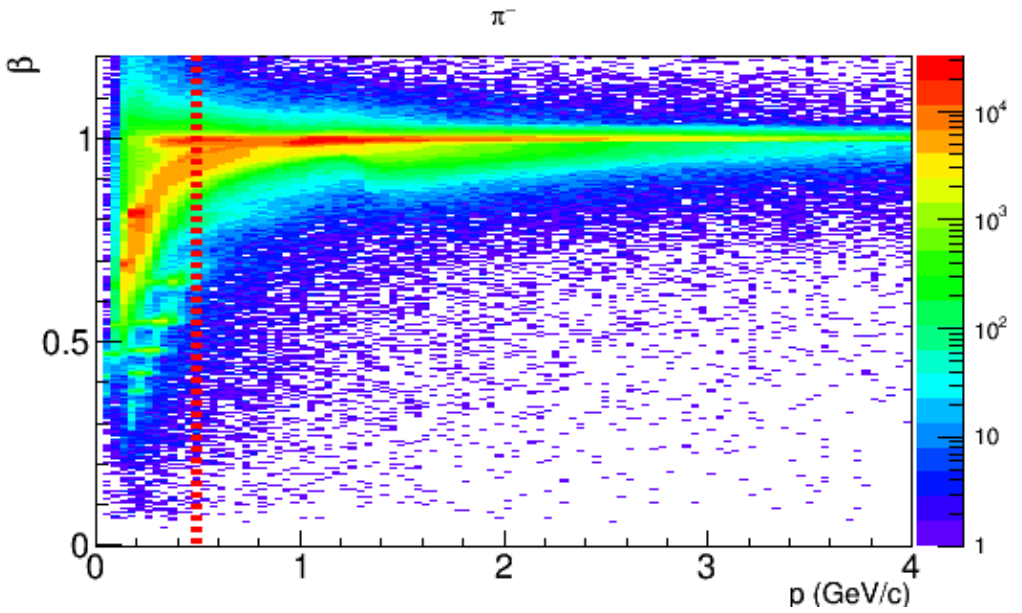

Figure 4.32: π^- β *vs.* p distribution. Shown is the π^- β *vs.* p distribution from the Spring 2015 run 2931. Only π^- tracks with $p > 0.5$ GeV/c were selected. This cut corresponds to all tracks to the right of the red dashed vertical line.

track to serve as the reference time since these tracks have the least amount of background associated with them.

Once a good π^- track was acquired it was then required to match to a hit in the TOF and not also match to a hit in the ST. This was done in order to avoid any potential bias in the calibration. The advantage of using the TOF time is that the time resolution of the TOF is the best of any detector in HallD ($\approx$ 96 ps) [36]. The calibrated (time-walk & propagation) hit time returned by the TOF (T^{TOF}_{hit}) was then corrected for the flight time from the π^- track vertex to the TOF (T^{TOF}_{flight}). Equation 4.24 is the TOF measure of the π^- track vertex time.

$$T^{TOF}_{vertex} = T^{TOF}_{hit} - T^{TOF}_{flight} \tag{4.24}$$

4.5.3 Obtaining the RF Reference Time

The RF signal that is readout in HallD is provided by the CEBAF accelerator at a rate of 499 MHz (2.004 ns) while the beam bunches in the Spring 2015 commissioning are produced at a rate of 249.5 MHz (4.008 ns). The RF signal from the accelerator is multiplexed into four detector system TDC's namely the TAGH, FDC, PSC, & TOF. However, the provided signal rate is too high to readout without causing overflow in the TDC buffers thus the RF signal is pre-scaled [37]. A typical pre-scale factor is 128 and consequently the RF signal is readout every 128×2.004 ns $= 256.512$ ns. Thus, the time associated with the beam bucket that produced the event of interest must be calculated since it is not provided directly.

For every event, the associated RF time provided by the CEBAF accelerator and by the HallD analysis library (DANA) is the pre-scaled time the RF signal arrived at the center of the target (T^{RF}_{center}). This time must be propagated out to the vertex location of the track since the photon responsible for the track spends a

finite amount of time traversing through the target before interacting with it. This propagation time (T^{RF}_{prop}) correction is given by Eq. 4.25

$$T^{RF}_{prop} = (z_{vertex} - z^{target}_{center}) \cdot \frac{1}{c} \tag{4.25}$$

Once the propagation time is summed with the centered RF time (T^{RF}_{center}) one obtains the measure of the RF time at the vertex of the π^- track and is given by Eq. 4.26.

$$T^{RF}_{vertex} = T^{RF}_{center} + T^{RF}_{prop} \tag{4.26}$$

Due to the inherent ambiguity associated with pre-scaling, T^{RF}_{vertex} is not the correct measurement of the time the beam bunch actually produced the π^- track. Therefore, one must "step" T^{RF}_{vertex} to the time the π^- track was produced as measured by T^{TOF}_{vertex}. To do this one must first calculate the time difference δT given by Eq. 4.27.

$$\delta T = T^{TOF}_{vertex} - T^{RF}_{vertex} \tag{4.27}$$

Next, one must calculate the number of beam buckets ($N^{buckets}_{step}$) that have elapsed during the δT time period and is given by Eq. 4.28, where ($N^{buckets}_{step}$) is rounded to the nearest integer.

$$N^{buckets}_{step} = \frac{\delta T}{T^{BB}_{period}} = \frac{\delta T}{4.008\ ns} \tag{4.28}$$

Lastly one can now calculate the time the beam bunch arrived at the vertex that produced the π^- track (T^{BB}_{vertex}) and is given by Eq. 4.29.

$$T^{BB}_{vertex} = T^{RF}_{vertex} + T^{BB}_{period} \cdot N^{buckets}_{step} \tag{4.29}$$

For every event, the first π^- track satisfying the aforementioned event selections outlined in section 4.5.2 will then have the associated T^{BB}_{vertex} time calculated which will serve as the reference time for all other tracks that have intersected the ST.

4.5.4 Start Counter Propagation Time Corrections

In order to properly calculate the propagation time (T^{ST}_{prop}) of photons produced by a charged track intersecting the ST, a few quantities must be known. Particularity the time-walk corrected hit time (T^{ST}_{hit}), the flight time from the track vertex to the ST intersection point (T^{ST}_{flight}), and a well defined reference time corresponding to the event (T^{BB}_{vertex}).

Once T^{BB}_{vertex} has been determined, all other charged tracks in the event were analyzed. These charged tracks were then subject to the same event selection procedure outlined in section 4.5.2 except that they must also have a matched hit in the ST.

It is required to note that for each charged track reported by DANA, there are multiple time-based tracks associated with it. For instance, if the track is negatively charged then there will exist three time-based tracks associated with it that contain different mass hypotheses *i.e.* e^-, π^-, K^-. For each time based track, and its associated mass hypothesis, there exists a tracking FOM which quantifies how "good" the track is based on it's respective mass hypothesis.

Since each charged track has multiple time based tracks associated with it, corresponding to various mass hypotheses, only the time based track with the highest tracking FOM was considered so as to avoid double counting. Each of those charged tracks were then required to match to a hit in the ST. Charged tracks satisfying these conditions then had their respective hit times and flight times recorded so that a relative time difference between the beam bunch time, which serves as the event reference time, could be calculated and is given by Eq. 4.30.

$$T^{ST}_{prop} = T^{ST}_{hit} - T^{ST}_{flight} - T^{BB}_{vertex} \tag{4.30}$$

This time difference is a direct measure of the amount of time the detected light produced by the intersecting charged track spent traversing the scintillator medium.

In order to perform the propagation time corrections the z-coordinate of the tracks intersection point with the ST (z_{hit}^{ST}) was also recorded for every charged track intersecting the ST. Once both T_{prop}^{ST} and z_{hit}^{ST} were calculated the propagation correction calculation could be performed. Figure 4.33 illustrates correlation between these two quantities.

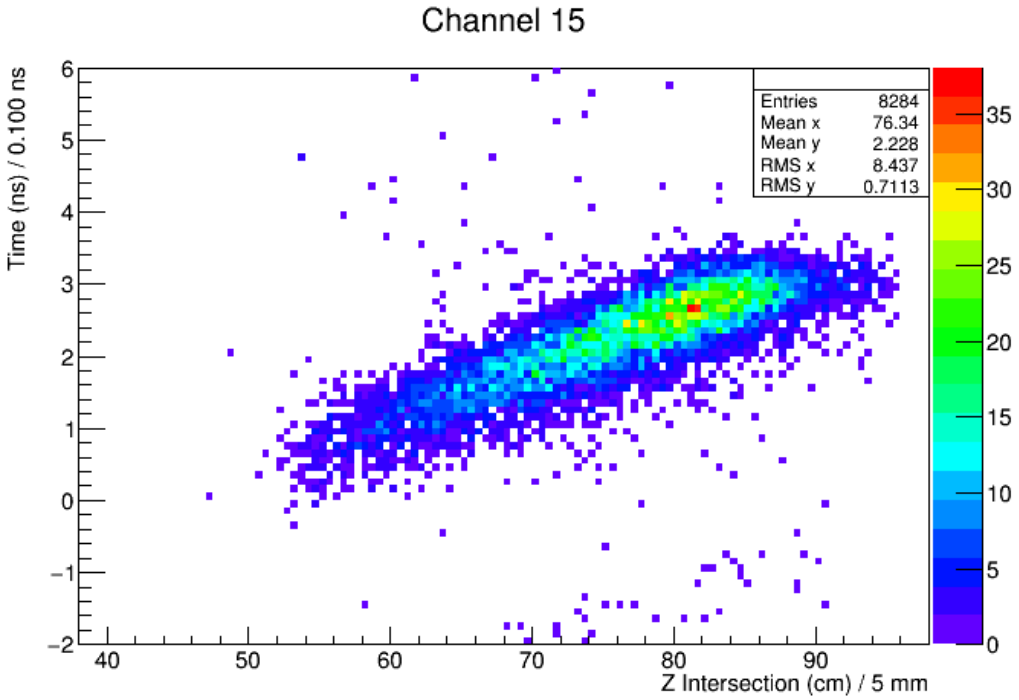

Figure 4.33: Typical Start Counter propagation time correlation. Shown is the ST propagation time correlation for sector 15 of the ST during the Spring 2015 run 2931. T_{prop}^{ST} is plotted on the y-axis and the z_{hit}^{ST} is plotted along the x-axis. There is a clear correlation between the time in which optical photons are detected by the SiPM and the location of the charged track intersection point with the ST. z is in hall coordinates.

For each 0.5 cm bin in z_{hit}^{ST} the corresponding propagation time distributions were fit utilizing the identical two-step fitting procedure discussed in section 4.3.4. It should be noted that only bins in z which had more than 65 entries were fit so that the means extracted were reliable. The lack of statistics from the Spring 2015 run is the direct cause for not having data for in the regions $z_{hit}^{ST} < 30.0$ cm and

$z_{hit}^{ST} > 50.0$ cm. The mean value of the propagation time, and it's associated error, were then plotted versus the center of each 0.5 cm bin in z_{hit}^{ST} as can be seen in Fig. 4.34. It is important to note that the data in Fig. 4.34 has been offset relative to Fig.

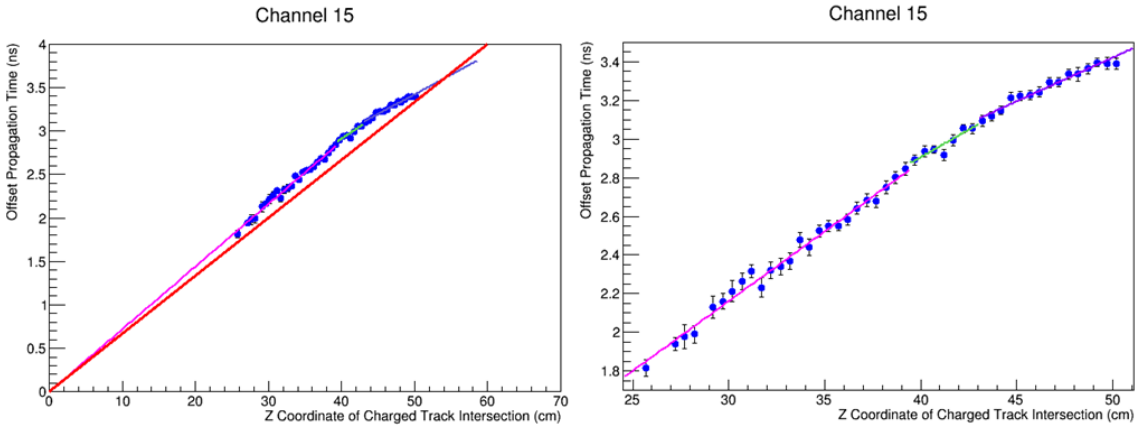

Figure 4.34: Typical Start Counter propagation time projection correlation. Left: Typical propagation time projection correlation for sector 15 of the ST during the Spring 2015 run 2931. The red line serves as a reference for the propagation time assuming it was a constant 15 cm/ns. The magenta line is the fit corresponding to the straight section. The green and dark blue solid lines correspond to the fits in the bend and nose section respectively. Right: zoomed in view of data points.

4.33 in both z and T_{prop}^{ST}. This was done so that when $z_{hit}^{ST} = 0.0$ cm, $T_{prop}^{ST} = 0.0$ ns.

The mean propagation times were then grouped into three distinct regions corresponding to the three unique geometrical sections of the ST namely the straight, bend, and nose regions. These three regions were then fit utilizing the χ^2 minimization technique with a linear function whose functional form is given by Eq. 4.31 where the index i indicates which region the fit is being performed.

$$f_i(z) = A_i + B_i \cdot z \tag{4.31}$$

With the fit parameters determined an explicit time difference correction for each of the 30 ST channels could then be applied to calculate the ST measure of the vertex time given by Eq. 4.32 which must be a function of where the charged

track intersects with the ST.

$$T^{ST}_{vertex}(z) = T^{ST}_{hit} - T^{ST}_{flight} - T^{ST}_{prop}(z) \tag{4.32}$$

4.6 Start Counter Time Resolution

Measuring the ST vertex time relative to the RF beam bunch vertex time is the most optimal way to determine the Start Counters ability to successfully identify the beam buckets associated with a particular event. The design resolution of the ST was to have all 30 sectors have a time resolution no larger than 350 ps so as to successfully identify the beam buckets to within a 99% accuracy.

4.6.1 Time Resolution Event Selection

The charged tracks used to perform the time resolution measurement are very similar to those which were used in section 4.5.2. Every charged track was required to have a tracking FOM > 0.0027 and only the time based track with the best FOM was utilized to avoid double counting. Each charged track was required to have z_{vertex} be contained within the target geometry while the r_{vertex} was required to be contained within the scattering chamber geometry. Lastly, each charged track was required to have a matched hit in the ST. All charged tracks satisfying the aforementioned conditions were used in the time resolution measurements discussed below.

4.6.2 Time Resolution Measurements

With both the time-walk corrections and the propagation time corrections complete it is relatively simple to calculate the time resolution of the ST relative to the RF (beam bunch) signal. All that is needed is to calculate the ST measure of the

vertex time for each charged track given by Eq. 4.32. Then in an identical manner outlined in section 4.5.3 T^{RF}_{vertex} must be "stepped" to the time the charged track vertex was produced so as to obtain a proper measure of the T^{BB}_{vertex}. The resulting distribution in the time difference of these two times provides a measure of the ST time resolution and is seen in Fig. 4.35. It is useful to note that while Fig. 4.35

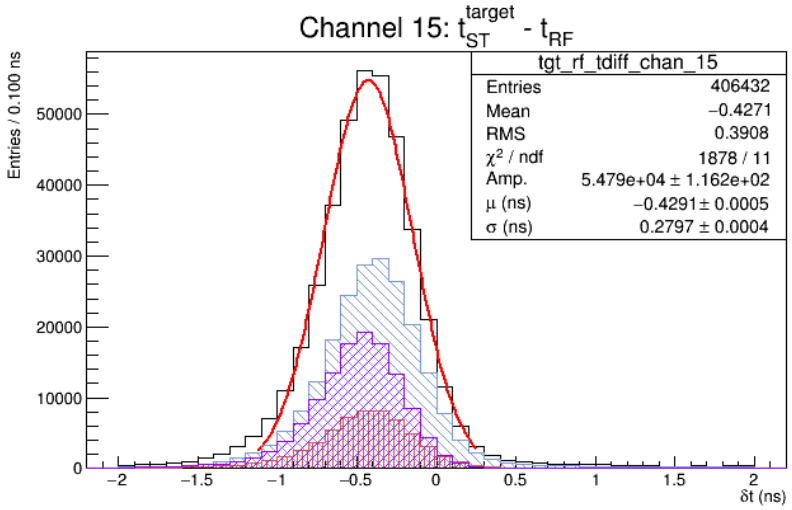

Figure 4.35: Typical Start Counter/RF time resolution distribution. Shown is the time resolution distribution for sector 15 during the Spring 2015 run 2931. The x-axis is the time difference between T^{ST}_{vertex} and T^{BB}_{vertex}. The blue histogram is the resolution in the straight section. The red and purple histograms correspond to the resolution in the bend and nose sections respectively. The black histogram is a sum of the three sections and corresponds to the resolution along the entire length of the paddle.

only shows a Gaussian fit to the entire length of sector 15, identical fits were made to fit the individual sections as well so as to compare with data taken on the bench at FIU and is discussed below.

The aforementioned fits were then carried out for each of the 30 ST sectors with σ, and its associated error being calculated. Then a weighted average of the 30 σ's were calculated so that the ST could have its time resolution characterized in its entirety. The same procedure was also conducted for the three individual sections.

Figure 4.36 illustrates the uniformity in time resolution among all 30 sectors of the ST. Figure 4.36 indicates that the average time resolution of 300 ps is well below the

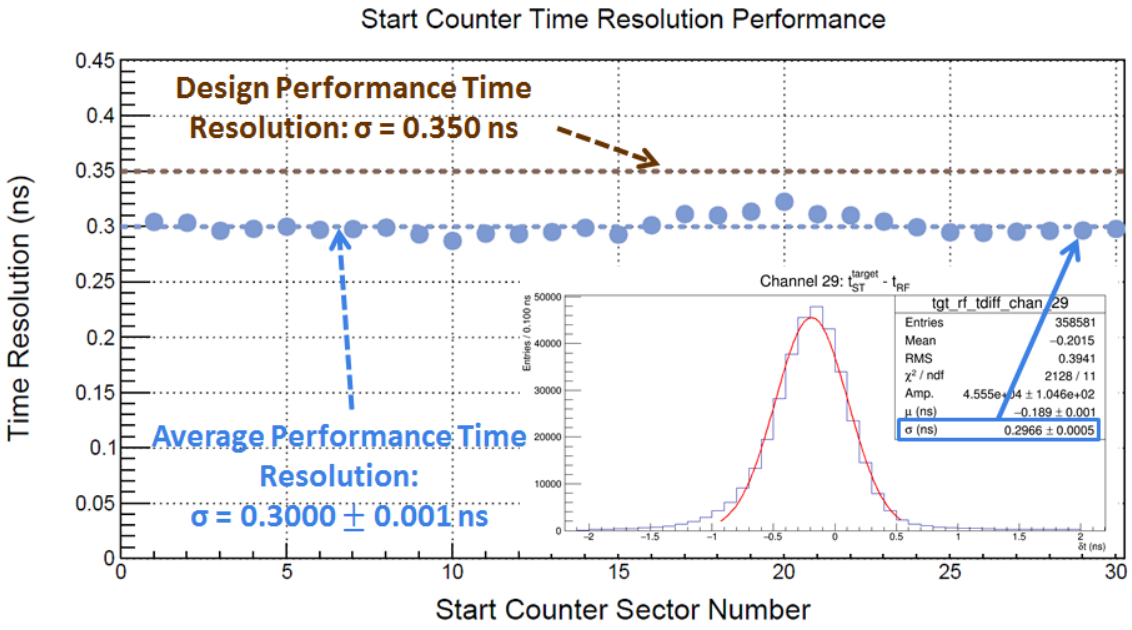

Figure 4.36: Start Counter time resolutions. Shown is the time resolution for all 30 sectors of the ST. The inset histogram illustrates the mean value of the Gaussian fit which characterizes the time resolution measurement for each of the 30 ST sectors.

design resolution of 350 ps. Table 4.4 details the weighted average time resolution of all 30 ST sectors in the different geometrical regions. It is clear from Table

ST Section	$\sigma_{\mathbf{all}}$	$\sigma_{\mathbf{straight}}$	$\sigma_{\mathbf{bend}}$	$\sigma_{\mathbf{nose}}$
$\sigma_{\mathbf{avg}}$	290 ps	299 ps	292 ps	264 ps

Table 4.4: Average time resolutions by section. Shown is the average of all 30 ST sectors by independent geometrical regions.

4.4 that the average time resolution measured with beam data is identical to the average of the data measured on the bench at FIU which was shown in Fig. 4.24. In addition what is observed is that measurements made with beam data exhibit the same phenomenon of substantial improvement in light collection, and thus time resolution, as light is produced further downstream in the nose region.

When these measurements were first conducted approximately 16 months had elapsed since polishing studies were being conducted at FIU on scintillators with severe surface damage. The 30 ST sectors are comprised of 30 of those very scintillators which were at one point unusable. Prior experience with degrading scintillators indicates that degradation in time resolution will be visible in a matter of weeks. However, after 16 months no degradation has been observed and the ST is performing well below design resolution.

CHAPTER 5

Beam Asymmetry Σ in Single π^0 Photoproduction

5.1 Measurement of the Beam Asymmetry Σ in Single π^0 Photoproduction

An initial measurement of the beam asymmetry Σ in the exclusive reaction $\vec{\gamma}p \to \pi^0 p$, where $\pi^0 \to \gamma\gamma$, has been carried out utilizing linearly polarized photons produced *via* the coherent Bremsstrahlung process, incident on a LH_2 target in Hall D. The tagged photon energies ranged from $2.5 \leq E_\gamma \leq 3.0$ GeV in the coherent peak. The resulting photoproduced π^0 meson, and its subsequent decay constituents ($\pi^0 \to \gamma\gamma$), as well as the recoiling proton were reconstructed with the GlueX spectrometer. The details of the GlueX spectrometer was outlined in section .

5.1.1 Event Selection

In order to isolate the $\vec{\gamma}p \to \pi^0 p$ reaction the linearly polarized photon data from runs 3185 and 3186, ≈ 33 M events, were analyzed. The particle combinations were required to contain 2 neutral particles, and one positive particle with the aim of properly selecting the corresponding 2 $\gamma's$ and the recoil proton respectively. The run conditions are given in Table 5.1. Furthermore, for these two runs the beam

Run Number	**Events**	**Beam Energy (GeV)**	**Beam Current (μA)**	**Solenoid Current (A)**
3185	19,866,480	5.5	11.8	1300
3186	13,117,090	5.5	17.6	1300

Table 5.1: Spring 2015 polarized photon beam run conditions. These runs consist of $\approx$ 2 hours of production data.

was collimated with a 5 mm diameter active collimator. The radiator used was the

J1A50, a 50 μm thick diamond from Hall B. The trigger was an energy sum between the FCAL and BCAL with the conditions that the shower energy in the calorimeters satisfied the relation ship: $E_{FCAL} + 4 \cdot E_{BCAL} > 0.5$ GeV.

For each event the beam photon and the reconstructed particles were required to originate in the same beam bunch while all other beam photons were rejected. Furthermore, the minimum shower energy in both the BCAL and FCAL was required to be larger than 0.1 GeV on an individual basis. Furthermore, each track in the event was required to have a tracking confidence level greater than 5.73×10^{-7}.

For proton candidates the TOF, BCAL, and FCAL detector systems can measure the track vertex time by correcting for the tracks flight time from its vertex to each respective detector. The difference (Δt) of the vertex time relative to the RF beam bunch time provides a robust way to ensure the proper particle identification (PID) has been made for that particular candidate. A similar calculation can be done for photon candidates in the calorimeters, namely the FCAL and BCAL. Figure 5.1 illustrates two examples of PID timing cuts made in the BCAL for both proton and photon candidates. Table 5.2 summarizes the various PID Δt cuts made for the

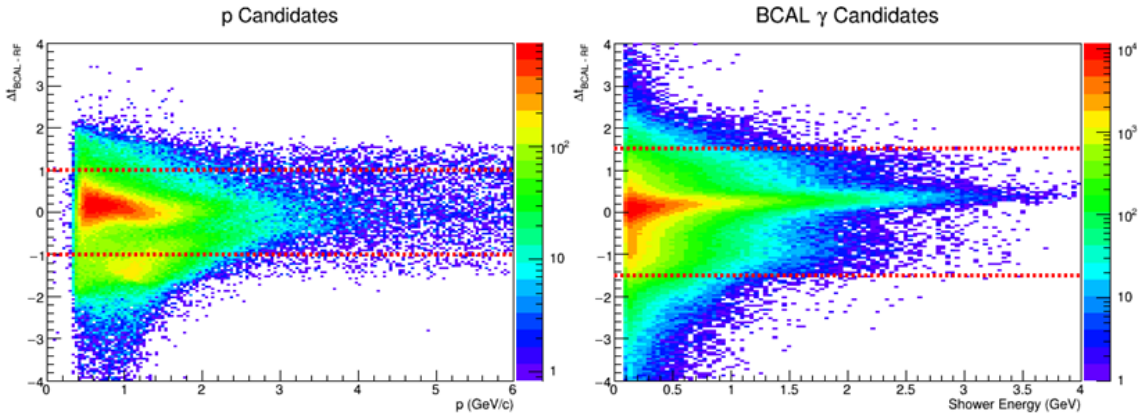

Figure 5.1: PID Δt cuts. Left: PID $\Delta t = \pm 1$ ns cut made for proton candidates in the BCAL. Right: PID $\Delta t = \pm 1.5$ ns cut made for photon candidates in the BCAL. The horizontal dashed red lines indicate the cut region.

proton and photon candidates.

Candidate	Detector System	Δt cut (ns)
Proton	TOF	±1.0
Proton	BCAL	±1.0
Proton	FCAL	±2.0
Photon	BCAL	±1.5
Photon	FCAL	±2.0

Table 5.2: Summary of PID Δt cuts.

To better isolate the proton candidates from other positively charged particles, the CDC was utilized in measuring the tracks energy deposition per unit length (dE/dx) in correlation with the tracks momentum (p). The dE/dx *vs.* p distribution for proton candidates as measured by the CDC is shown in Fig. 5.2. According to

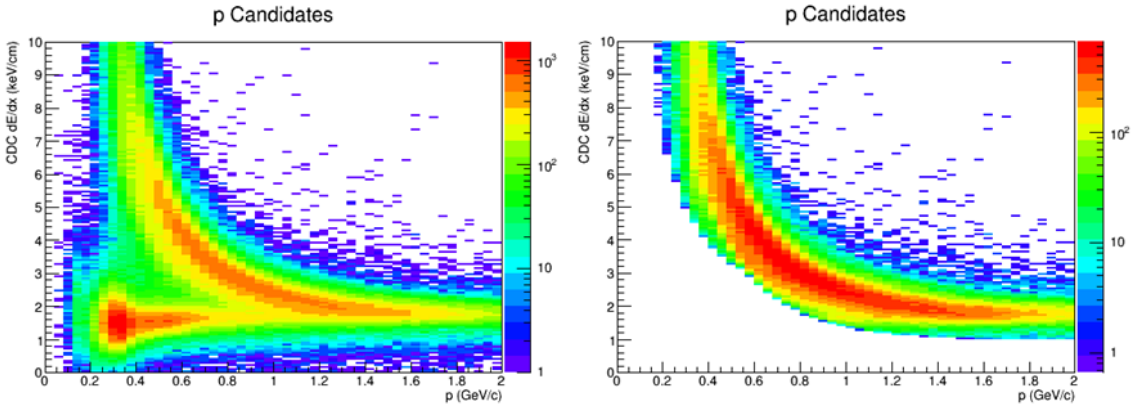

Figure 5.2: dE/dx *vs.* p in the CDC. Left: dE/dx *vs.* p in the CDC before applying exponential cut. Right: dE/dx *vs.* p in the CDC after applying exponential cut. There is clear proton/hadron separation for tracks with $p < 1.0$ *GeV*

the Bethe-Bloch equation, $dE/dx \propto M/\beta^2$ [34] implying then that protons with slower momenta will deposit more energy per unit length than lighter particles with same momentum. As seen in Fig. 5.2 the "banana band" corresponds to protons while the horizontal band $\approx$ 1.5 GeV corresponds to other positively charged particles which have been misidentified as protons. Therefore, in order to reduce the number of misidentified proton candidates an exponential cut, whose parameters

were determined empirically, was applied to the $dE/dx vs. p$ data. The functional form is given by Eq. 5.1.

$$\frac{dE}{dx} = 1.0 + e^{3.93p+3.0} \tag{5.1}$$

The effects of applying the exponential cut are illustrated in Fig. 5.2 and there is a clear reduction in contamination for proton candidates with low momentum. The advantage to utilizing an exponential cut is that it is better at maximizing the number of "good" proton candidates as opposed to imposing a horizontal dE/dx cut.

With the fiducial PID cuts having been implemented to the data, kinematic constraints were then applied to the data. In order to more easily discuss the kinematic variables associated with the topology $\vec{\gamma}p \to \pi^0 p$, four momentum vectors are labelled as $P_{\mu,X}$ where X is the particle label. Moreover, the label $\mathbf{P_X^T}$ will refer to the transverse momentum ($\mathbf{P_X^T} = (P_{x,X}, P_{y,X})$) of particle $\mathbf{X}$.

The proton initial four vector is assumed to be at rest and $P_{\mu,p} = (m_p, 0, 0, 0)$. The incident polarized photon is assumed to have momentum only in the z direction $P_{\mu,\gamma} = (E_\gamma, 0, 0, P_{z,\gamma})$. If we define the initial transverse momentum vector as $\mathbf{P_i^T} = \mathbf{P_\gamma^T} + \mathbf{P_p^T}$ it follows that the composite initial system will have zero transverse momentum.

Conservation of momentum gives $\mathbf{P_i^T} = \mathbf{P_f^T}$ where $\mathbf{P_f^T} = \mathbf{P_{\pi^0}^T} + \mathbf{P_{p'}^T}$ and p' is the recoil proton. Since the initial state four vector has zero transverse momentum it must be that $\mathbf{P_{\pi^0}^T} = -\mathbf{P_p^T}$ and therefore the $\pi^0 p$ system will be coplanar, *eg.* $\delta\phi(\pi^0 p) = 180^\circ$, in the lab frame where ϕ is the azimuthal angle between the π^0 and the recoil proton. Figure 5.3 illustrates the coplanar nature of the $\pi^0 p$ system. Only events which have passed the aforementioned PID cuts and have $\delta\phi(\pi^0 p) = 180^\circ \pm 5^\circ$ were considered for further analysis.

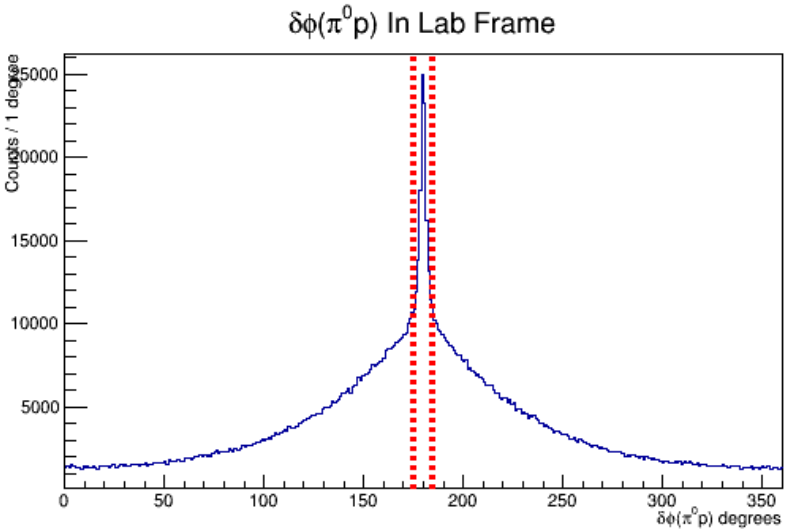

Figure 5.3: $\pi^0 p$ coplanarity cut. There is a clear coplanar preference of the $\pi^0 p$ system. The vertical red dashed lines indicate the coplanarity cut.

To further improve the $\vec{\gamma}p \to \pi^0 p$ event selection we required that the vertex of the recoil proton be located within the target geometry. In Fig. 5.4 the z coordinate of the recoil proton track vertex is required to occur within the 30 cm target, located at *eg.* 50 cm $< z_{vertex} <$ 80 cm. Furthermore, the track vertex is constrained to

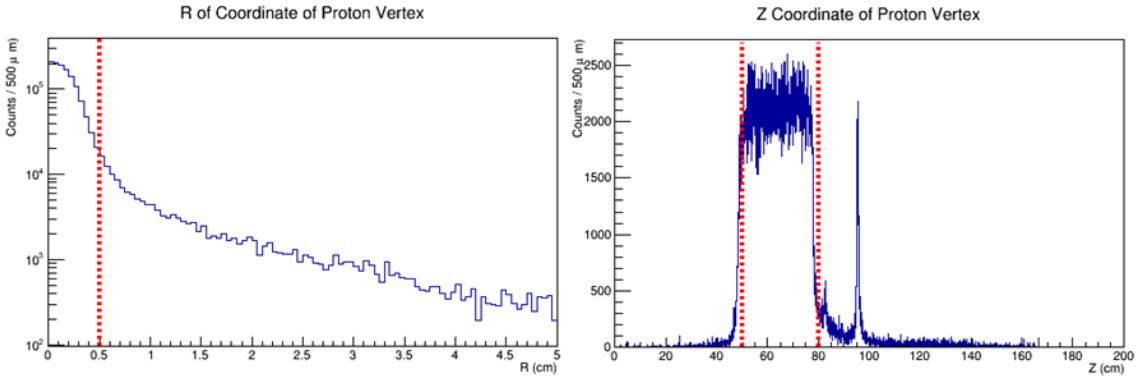

Figure 5.4: Recoil proton vertex cuts. Left: r coordinate of recoil proton vertex. Right: z coordinate of recoil proton vertex. The peak immediately downstream of the z = 80 cm cut is the vacuum chamber exit window, and the more prominent peak is a thin plastic target placed at the end of the ST. The vertical dashed red lines indicate the cuts.

have its position of closest approach to the beam line within the diameter of the collimated beam, *i.e.* $r_{vertex} < 5$ mm.

Let us define a "missing" four momentum vector given by Eq. 5.2.

$$P_{\mu,miss} = P_{\mu,i} - P_{\mu,f} = (P_{\mu,\gamma} + P_{\mu,p}) - (P_{\mu,\pi^0} + P_{\mu,p'}) \tag{5.2}$$

Conservation of energy and momentum require $P_{\mu,miss} = (0,0,0,0)$. However, this is not the case for every event due to the uncertainty of determining the particles four vectors. Therefore it is required to ensure that the missing mass and energy of the events are close to zero. The missing mass squared can be calculated for each event.

$$M^2_{miss} = P_{\mu,miss} \cdot P^{\mu,miss} = (E_\gamma + m_p - E_{\pi^0} - E_{p'})^2 - |\vec{p}_\gamma - \vec{p}_{\pi^0} - \vec{p}_{p'}|^2 \tag{5.3}$$

Moreover, the energy component of the missing four momentum vector, given by Eq. 5.2, should also be equal to zero. Figure 5.5 illustrates both the missing mass squared ($|M^2_{miss}| \leq 0.020$ GeV) and missing energy cuts ($|E_{miss}| \leq 0.200$ GeV) that were applied to the data. It is useful to note that in Fig. 5.5 the missing mass

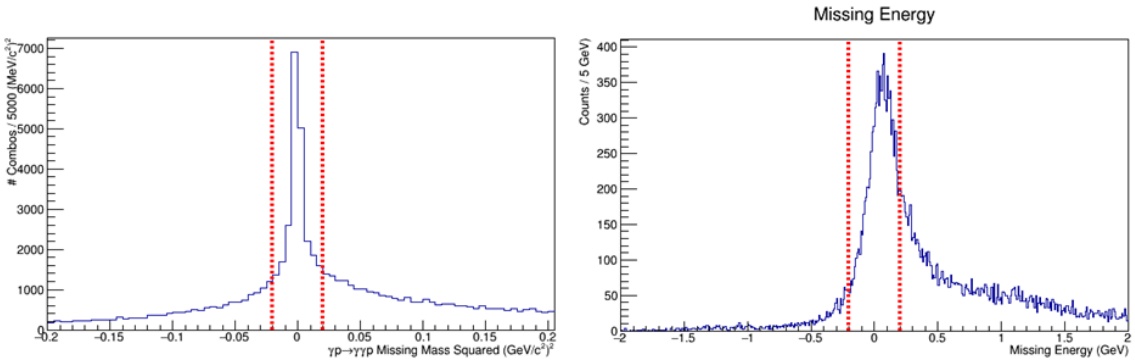

Figure 5.5: Missing mass squared & missing energy cuts. Left: Missing mass squared cut. Right: missing energy cut. The vertical dashed red lines indicate the cuts.

squared cut was applied prior to the missing energy cut.

One of the most crucial kinematic constraints that was applied to the data to cleanly select the $\vec{\gamma}p \to \pi^0 p$ topology was the cut applied to the $\gamma\gamma$ invariant mass

spectrum. Figure 5.6 illustrates the effects of the PID Δt, CDC dE/dx *vs.* p cut, and the $\pi^0 p$ coplanarity cut in the $\gamma\gamma$ invariant mass spectrum. Figure 5.7 shows

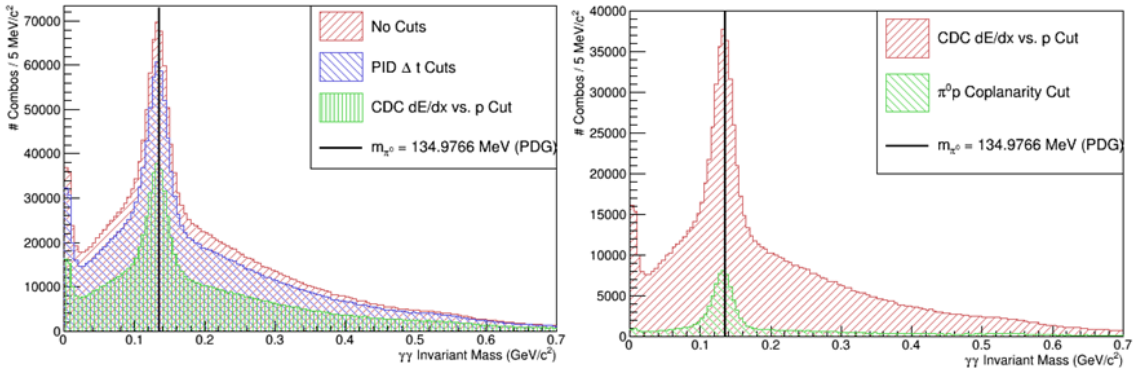

Figure 5.6: Effects of cuts on the $\gamma\gamma$ invariant mass spectrum. Left: PID Δt, and CDC dE/dx vs. p cuts on the raw $\gamma\gamma$ invariant mass spectrum. Right: $\pi^0 p$ coplanarity cut on the CDC dE/dx vs. p cut data.

the effects of the recoil proton vertex cut, the missing mass squared cut, the missing energy cut, and lastly the $|m_{\pi^0}| \leq 0.035$ GeV cut. It is clear from figures 5.6 and 5.7

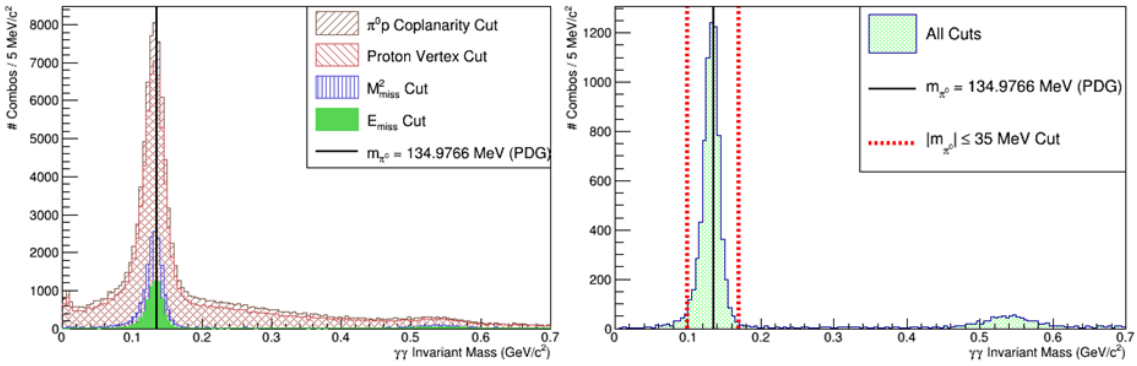

Figure 5.7: Final $\gamma\gamma$ invariant mass spectrum. Left: recoil proton vertex, missing mass squared, and missing energy cuts on the $\pi^0 p$ coplanarity cut data. Right: $\gamma\gamma$ invariant mass cut. It is useful to note that the η mass peak is seen at approximately 0.550 GeV.

that the most significant cuts came from the $\pi^0 p$ coplanarity cut and the missing mass squared cut.

In order to extract the beam asymmetry Σ for the reaction $\vec{\gamma}p \rightarrow \pi^0 p$ only events occurring in the coherent peak were analyzed. Therefore, a cut on the tagged

photon energy was applied to the data with the aforementioned event selection criteria. The tagged photon energy spectrum is shown in Fig. 5.8 with the coherent peak cut ($2.5 \leq E_\gamma \leq 3.0$ GeV) shown. It is required to note that the number of

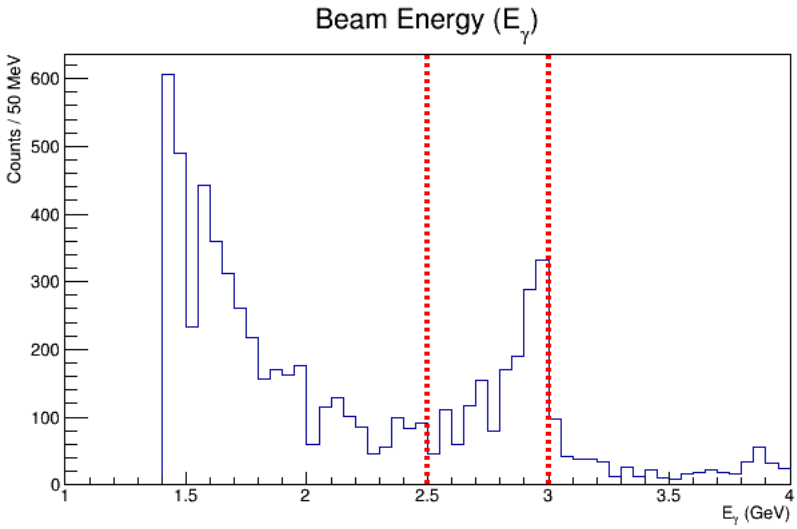

Figure 5.8: Coherent peak cut. For $E_\gamma < 2.5\ GeV$ the low energy Bremsstrahlung spectrum is clearly visible. Furthermore for photon energies $2.5 \leq E_\gamma \leq 3.0\ GeV$ the sharp coherent peak is also visible.

π^0 candidates shown in Fig. 5.7 was reduced by a factor of 6 upon selecting tagged photons in the coherent peak.

All of the events passing the aforementioned cuts were classified as events corresponding to the $\vec{\gamma}p \to \pi^0 p$ topology and were used to extract the associated beam asymmetry Σ.

5.1.2 Measuring the beam asymmetry Σ

In order to calculate the degree of polarization of the photon beam in the coherent peak a fit to the enhancement spectrum was performed [38]. The enhancement spectrum is calculated by dividing the tagged polarized photon energy spectrum by the unpolarized Bremsstrahlung photon energy spectrum produced with an amorphous

radiator. The enhancement spectrum is then fit to obtain the average and peak degree of polarization for the linearly polarized photon beam and is illustrated in Fig. 5.9. The fit to the enhancement spectrum yields a peak polarization of $\sim 65\%$ [38]

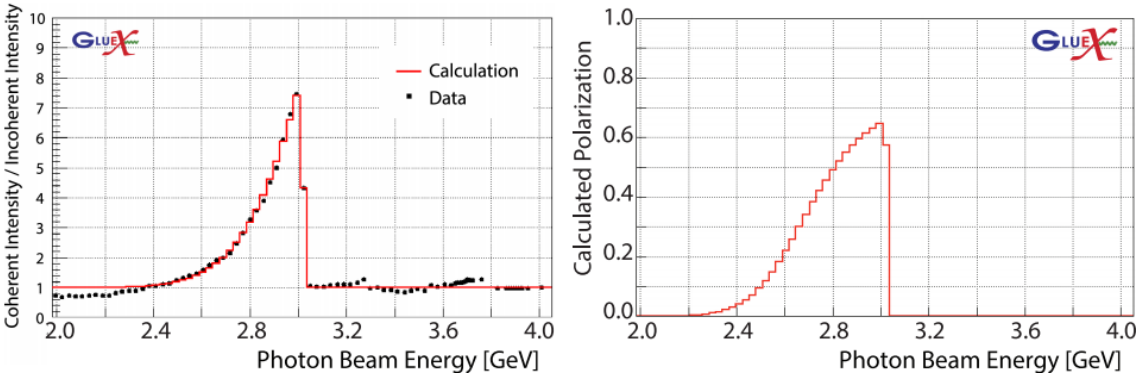

Figure 5.9: Beam polarization in run 3185. Left: fit to the enhancement spectrum where only the coherent peak is visible. Right: calculated polarization resulting from the fit to the enhancement spectrum [3].

and an average polarization $P_{||} \approx 47\%$ [39].

The polarized photon beam during runs 3185 and 3186 in the Spring 2015 commissioning run had its electric vector oriented parallel to the floor whose degree of polarization is denoted as $P_{||}$. The differential cross section for the incident photon beam polarization is given by Eq. 5.4 where σ_a is the unpolarized cross section, and Σ is the associated beam asymmetry [40] [41].

$$\frac{d\sigma_{||}}{d\Omega} = \frac{d\sigma_a}{d\Omega}(1 - P_{||}\Sigma cos(2\phi)) \tag{5.4}$$

Moreover, the variable ϕ is the azimuthal angle of the π^0 in the lab frame. The ϕ dependence of Σ arises from the partial wave expansion of the helicity amplitude elements [42]. Therefore, the ϕ distribution of the photoproduced π^0 meson can be fit with the functional form $A(1+Bcos(2\phi))$ where $B = P_{||}\Sigma$. Figure 5.10 shows the modulation of ϕ for the π^0 for runs taken with an amorphous radiator and oriented diamond. There is a clear modulation in ϕ due to the polarization transfer from

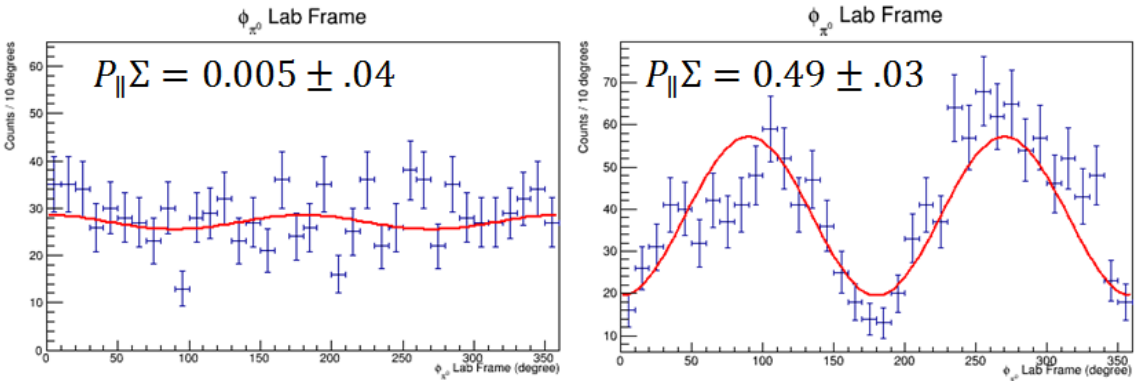

Figure 5.10: ϕ distribution of the photoproduced π^0 meson. Left: ϕ distribution of the photoproduced π^0 meson utilizing a unpolarized photon beam produced with an amorphous radiator. Right: ϕ distribution of the photoproduced π^0 meson utilizing a polarized photon beam produced with an oriented diamond. There is a clear modulation in ϕ due to the polarization transfer from the beam to the π^0

the beam to the π^0 as opposed to the non existent modulation for the amorphous radiator runs.

The world data for measuring the beam asymmetry Σ of the photoproduced π^0 meson with linearly polarized photons in the $2.5 \leq E_\gamma \leq 3.0$ GeV is quite sparse. One experiment was carried out 46 six years prior at the Massachusetts Institute of Technology (MIT) utilizing the Cambridge electron accelerator (CAE) in which linearly polarized photons in the energy range $2.7 \leq E_\gamma \leq 3.3$ GeV were incident on a LH_2 target [43]. Figure 5.11 illustrates the definition of the kinematic variables for the $\vec{\gamma}p \rightarrow \pi^0 p$ topology. The Mandelstam variable t for the reaction of interest

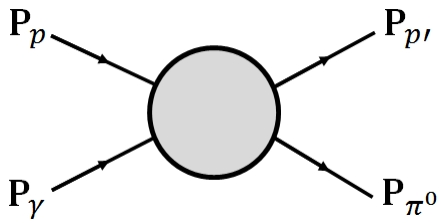

Figure 5.11: Two body reaction schematic.

is given by Eq. 5.5.

$$t = (\mathbf{P_p} - \mathbf{P_{p'}})^2 = m_p^2 - 2E_pE_{p'} + 2\mathbf{P_p}\mathbf{P_{p'}} + m_{p'}^2 \tag{5.5}$$

Therefore, t is a measure of the squared four momentum transfer of the photon to the target proton. The experiment at CEA measured Σ for $0.1 \leq t \leq 1.2$ GeV^2.

Utilizing the Spring 2015 polarized photon data, the modulation in ϕ of the photoproduced π^0 meson was measured in three ranges of Mandelstam t namely, $0.0 \leq t \leq 0.5$ GeV^2, $0.5 < t \leq 1.0$ GeV^2, and $1.0 < t \leq 1.5$ GeV^2. Due to the severe lack of statistics produced in only two hours of physics production, the binning had to be quite coarse. Figure 5.12 shows fits to the data to extract $P_{||}\Sigma$ the three bins in Mandelstam t. Assuming the average beam polarization to be $P_{||} = 47\%$ [39] the beam asymmetry Σ was measured from the relationship $\Sigma = B/P_{||}$ for each of the three bins in Mandelstam t and is shown in Fig. 5.13 relative to the Σ determined at CEA [43]. Figure 5.13 shows that with only the 2 hours of physics data, the GlueX beam asymmetry measurements agree well with MIT data within error.

A similar beam asymmetry measurement was attempted in the $\vec{\gamma}p \rightarrow \pi^+(n)$ topology where the neutron was missing. A nearly identical event selection as was carried out for the π^+ as was discussed previously. However, upon investigating the missing mass spectrum, shown in Fig. 5.14, no clear neutron candidates were observed after implementing various fiducial cuts and cutting on tagged photons in the coherent peak. Due to the large background observed in this particular topology, the beam asymmetry could not be extracted. It is important to realize that the trigger type used in these runs was an energy sum between the FCAL and BCAL with the conditions that the shower energy in the calorimeters satisfied the relation ship: $E_{FCAL} + 4 \cdot E_{BCAL} > 0.5$ GeV. Furthermore, the minimum ionizing

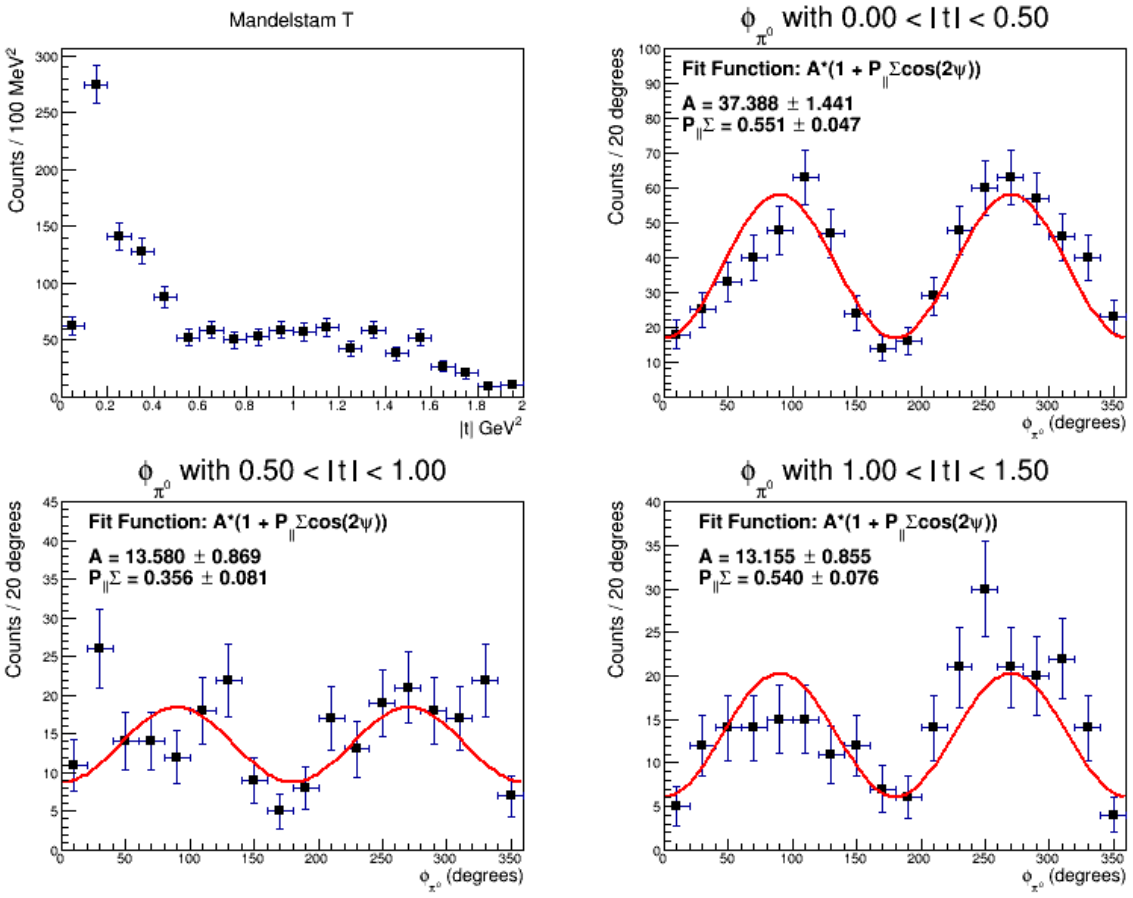

Figure 5.12: ϕ modulation fits in different bins of Mandelstam t. There is clear lack of statistics for $|t| > 0.5\ GeV^2$.

energy in the FCAL for pions is ≈ 0.4 GeV and therefore suppresses the detection of a single π^+.

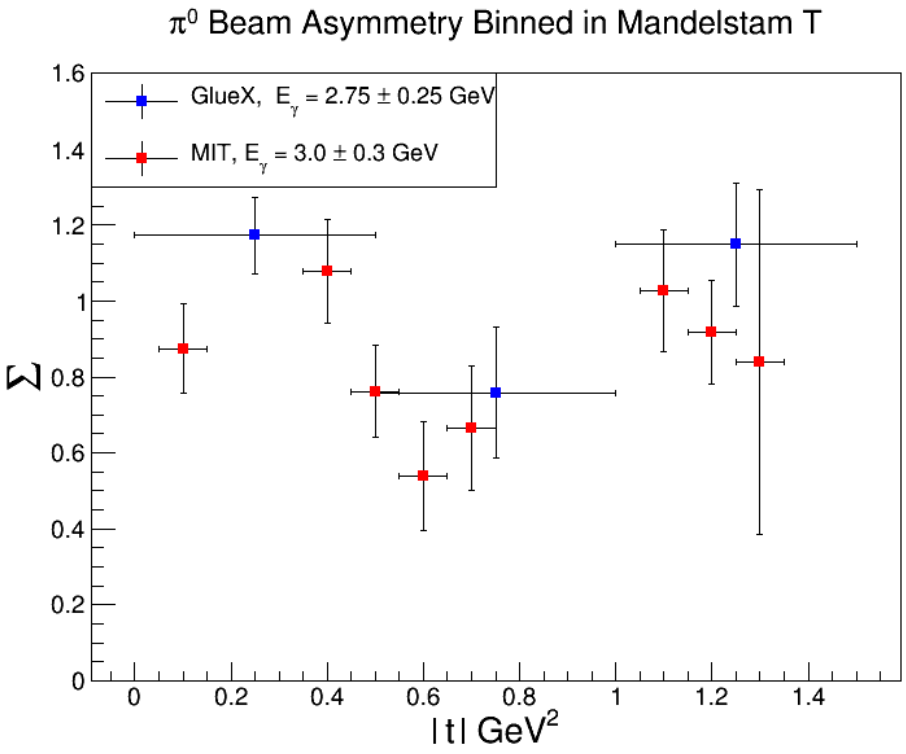

Figure 5.13: Beam asymmetery measurements at both GlueX and MIT. The horizontal error bars correspond to the bin width of Mandelstam t.

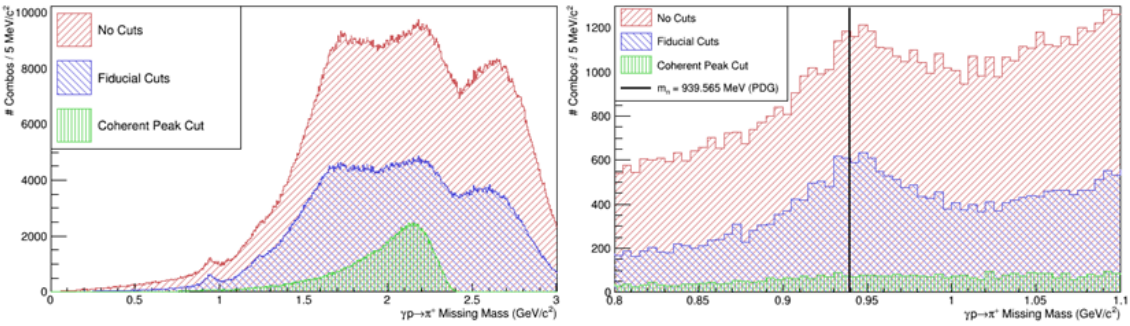

Figure 5.14: $\vec{\gamma}p \to \pi^+(n)$ missing mass spectrum. Left: broad missing mass spectrum. Right: zoomed in missing mass spectrum centered around the neutron mass.

BIBLIOGRAPHY

[1] Curtis Meyer et al. The gluex experiment in hall-d. A proposal to the 36th Jefferson Lab Program Advisory Committee, GlueX-doc 1545-v7, 2010.

[2] Lawrence Cardman and et al. The science driving the 12 gev upgrade of cebaf. Available at, 2001.

[3] Justin Stevens. Gluex progress and plans. Talk given at the Science and Technology Review, 2015.

[4] Volker Crede et al. An initial study of mesons and baryons containing strange quarks with gluex. A proposal to the 40th Jefferson Lab Program Advisory Committee, GlueX-doc 2198-v10, 2013.

[5] Jozef J. Dudek et al. Toward the excited isoscalar meson spectrum from lattice qcd. *Phys. Rev. D*, 88, 2013.

[6] Simon Taylor. A first look at reconstructed data from the gluex detector. Talk given at the 2015 DNP meeting, 2015.

[7] Liping Gan. Symmetry tests of rare eta decays to all-neutral final states: The jlab eta factory (jef) experiment. Eta Rare Decay Proposal for PAC40, 2014.

[8] GlueX Collaboration. *Hall D GlueX Technical Construction Report*, May 2015. Technical note GlueX-doc-2511-v4 available at `http://argus.phys.uregina.ca/gluex/DocDB/0025/002511/004/tcr.pdf`.

[9] Curtis Meyer. Performance of the gluex detector systems. Technical note GlueX-doc-2775-v10, 2015.

[10] Alexander Somov et al. Pair spectrometer hodoscope for hall d at jefferson lab. *Nuclear Instruments and Methods in Physics Research Section A*, 795:376–380, 2015.

[11] Brianna Thorpe. A triplet polarimeter for use in the jefferson lab gluex experiment. Poster for APS 2015 meeting, 2015.

[12] Kei Moriya. Polarimeter update. Talk given at the Fall 2015 GlueX collaboration meeting, 2015.

[13] Beni Zihlmann. *TOF detector description for CDR*, March 2008. Technical note available at http://argus.phys.uregina.ca/gluex/DocDB/0009/000994/004/TOF_cdr.pdf.

[14] Daniel S Carman. *Forward Drift Chamber Technical Design Report*, June 2008. Technical note available at http://argus.phys.uregina.ca/gluex/DocDB/0007/000754/010/fdc_design.pdf.

[15] Justin Stevens. *GlueX FDIRC Technical Design Report*, September 2015. Technical note available at http://argus.phys.uregina.ca/gluex/DocDB/0028/002809/003/dirc_tdr.pdf.

[16] http://www.plastic-craft.com/.

[17] http://www.mcnealplasticmachining.com/.

[18] E.H. Bellamy et al. Absolute calibration and monitoring of a spectrometric channel using a photomultiplier. *Nuclear Instruments and Methods in Physics Research Section A*, 339:468–476, 1994.

[19] https://geant4.web.cern.ch/geant4/.

[20] *EJ-200 Plastic Scintillator.* Technical note available at http://www.eljentechnology.com/images/stories/Data_Sheets/Plastic_Scintillators/EJ200%20data%20sheet.pdf.

[21] Kenneth S. Krane. *Introductory Nuclear Physics*, chapter Detecting Nuclear Radiations, pages 201–202. John Wiley & Sons, 1988.

[22] Puneet Khetarpal. *Start Counter Geant4 Simulations.* Start Counter Geant4 Simulations Wiki available at https://halldweb.jlab.org/wiki/index.php/Start_Counter_Simulations.

[23] Christopher M. Poole. A cad interface for geant4. Paper submitted to Cornell Archive (arXiv) May 5, 2011, 2011.

[24] A. Levin & C. Moison. A more physical approach to model the surface treatment of scintillation counters and its implementation into detect. Paper presented at IEEE, Nuclear Science Symposium; Anaheim, November 2-4 available at http://geant4.slac.stanford.edu/UsersWorkshop/PDF/Peter/moisan.pdf, 1996.

[25] Puneet Khetarpal. Start counter: Optics simulations. Talk Given at the February 16, 2012 GlueX Collaboration meeting, 2012.

[26] E. Jastrzembski & H. Dong. *Summary of FADC250 Operating Modes*, February 2014. Technical note available at `https://userweb.jlab.org/~brads/Manuals/Hardware/JLab/FADC/timing_extraction/FADC250%20modes%202-1.pdf`.

[27] E.S. Smith. *Low-level calibration constants for BCAL*, December 2014. Technical note GlueX-doc-2618-v10, available at `http://argus.phys.uregina.ca/gluex/DocDB/0026/002618/010/bcal_constants.pdf`.

[28] William R. Leo. *Techniques for Nuclear and Particle Physics Experiments: A How-to Approach*, chapter Timing Methods and Systems, pages 325–326. Springer-Verlag, 1994.

[29] J. Proffitt. *16-Channel Discriminator/Scaler VME Module Manual*, April 2003. Technical note GlueX-doc-530-v1 available at `http://argus.phys.uregina.ca/gluex/DocDB/0005/000530/001/discr_scaler_manual.pdf`.

[30] Fernando Barbosa et al. *F1TDC User's Manual V1.1*, April 2004. Technical note GlueX-doc-1021-v1 available at `http://argus.phys.uregina.ca/gluex/DocDB/0010/001021/001/F1TDC%20-%20User%20Manual%20V1.1.pdf`.

[31] Kei Moriya & Mark Ito. *Synchronization of GlueX Timing Systems*, July 2015. Technical note GlueX-doc-2686-v5 available at `http://argus.phys.uregina.ca/gluex/DocDB/0026/002686/005/tdc_writeup.pdf`.

[32] ^{90}Sr *Decay Radiation Data*. National Nuclear Data Center, Nuclear Structure and Decay Database (NuDat) available at `http://www.nndc.bnl.gov/nudat2/decaysearchdirect.jsp?nuc=90SR&unc=nds`.

[33] ^{90}Y *Decay Radiation Data*. National Nuclear Data Center, Nuclear Structure and Decay Database (NuDat) available at `http://www.nndc.bnl.gov/nudat2/decaysearchdirect.jsp?nuc=90Y&unc=nds`.

[34] J. Beringer et al. (Particle Data Group). Review of particle physics. *Phys. Rev. D*, 86(010001):342–343, 2012.

[35] Y.G. Sharabian et al. A new highly segmented start counter for the clas detector. *Nuclear Instruments and Methods in Physics Research Section A*, 556:246–258, 2006.

[36] Benedikt Zihlmann. *GlueX Time Of Flight Calibration*, July 2015. Technical note GlueX-doc-2767-v4 available at `http://argus.phys.uregina.ca/gluex/DocDB/0027/002767/004/tofcalib.pdf`.

[37] Paul Mattione. *RF Calibration*. RF Calibration Wiki available at `https://halldweb.jlab.org/wiki/index.php/RF_Calibration`.

[38] Ken Livingston. Coherent bremsstrahlung. Talk given at the Spring 2015 GlueX collaboration meeting, 2015.

[39] Justin Stevens. Physics update from fall and spring commissioning. Talk given at the Spring 2015 GlueX collaboration meeting, 2015.

[40] M. Dugger and et al. Beam asymmetry Σ for π^+ and π^0 photoproduction on the proton for photon energies from 1.102 to 1.862 gev. *Phys. Rev. C*, 88:065203, Dec 2013.

[41] N. Sparks and et al. Measurement of the beam asymmetry σ in the forward direction for $\vec{\gamma}p \to \pi^0 p$. *Phys. Rev. C*, 81:065210, Jun 2010.

[42] Patrick Collins. Beam asymmetry in eta(547) and eta(958) meson pohotoproduction. A Dissertation Presented in Partial Fulfilment of the Requirements for the Degree Doctor of Philosophy, 2009.

[43] D. Bellenger and et al. Photoproduction of π^0 with plane polarized 3-gev photons. *Phys. Rev. Lett.*, 23:540–542, Sep 1969.

VITA

ERIC POOSER

1985	Born, Atlanta, Georgia
2009	B.S., Physics & Mathematics University of North Georgia Dahlonega, Georgia
2016	Ph.D., Physics Florida International University Miami, Florida

PUBLICATIONS AND PRESENTATIONS

Pooser, E., (2012). *The GlueX Start Counter & S11 (1535) Electroproduction at Large* Q^2. Hampton University Graduate Studies Program. Newport News, Virginia.

Pooser, E., (2013). *The GlueX Start Counter*. Annual Meeting of the APS Southeastern Section. Bowling Green, Kentucky.

Pooser, E., (2013). *The GlueX Start Counter*. Fall Meeting of the APS Division of Nuclear Physics. Newport News, Virginia.

Pooser, E., (2015). *Hall D Update*. Invited talk given at the Joint Hall A/C Summer Collaboration Meeting. Newport News, Virginia.

Pooser, E., (2015). *The GlueX Start Counter & Beam Asymmetry* Σ *in Single* π^0 *Photoproduction*. Invited talk given at the Jefferson Lab Physics Seminar. Newport News, Virginia.

Pooser, E., (In progress). *Start Counter Research, Developments, Construction, & Calibration*. GlueX internal document.

Pooser, E., (In progress). *The GlueX Start Counter*. NIM A Article.